VOL. XI - Nº 3 1989
ISSN 0100-7386

REVISTA BRASILEIRA DE CIÊNCIAS MECÂNICAS

JOURNAL OF THE BRAZILIAN SOCIETY OF MECHANICAL SCIENCES

PUBLICAÇÃO DA ABCM
ASSOCIAÇÃO BRASILEIRA DE CIÊNCIAS MECÂNICAS

REVISTA BRASILEIRA DE CIÊNCIAS MECÂNICAS
JOURNAL OF THE BRAZILIAN SOCIETY OF MECHANICAL SCIENCES

EDITOR: **Hans Ingo Weber**

Deptº Projeto Mecânico, FEC, UNICAMP, Caixa Postal 6131, 13081 Campinas/SP, Brasil,
Tel. (0192) 39-7284, Telex (019) 1981, Telefax (0192) 39-4717

EDITORES ASSOCIADOS

Álvaro Toubes Prata
Deptº Engenharia Mecânica, UFSC, Caixa Postal 476, 88049 Florianópolis/SC, Brasil,
Tel. (0482) 34-5166, Telex (482) 240 UFSC

Augusto César Noronha R. Galeão
LNCC, Rua Lauro Müller 455, 22290 Rio de Janeiro/RJ, Brasil, Tel. (021) 541-2132 r. 170, Telex 22563 CBPQ

Carlos Alberto de Almeida
Deptº Eng. Mecânica, PUC/RJ, Rua Marquês de São Vicente, 255, 22453 Rio de Janeiro/RJ, Brasil,
Tel. (021) 529-9323, Telex (021) 131048

Hazim Ali Al-Qureshi
ITA/CTA, Caixa Postal 6001, 12225 São José dos Campos/SP, Tel. (0123) 41-2211

CORPO EDITORIAL

Abimael Fernando D. Loula (LNCC)
Arno Blass (UFSC)
Carlos Alberto de Campos Selke (UFSC)
Carlos Alberto Schneider (UFSC)
Clovis Raimundo Maliska (UFSC)
Fathi Darwich (PUC/RJ)
Henner Alberto Gomide (UFU)
Jaime Tupiassú de Castro (PUC/RJ)
João Lirani (EESC)
José Luiz de França Freire (PUC/RJ)
Leonardo Goldstein Jr. (UNICAMP)
Luiz Carlos Martins (COPPE/UFRJ)
Luiz Carlos Wrobel (COPPE/UFRJ)
Moysés Zindeluk (COPPE/UFRJ)
Nelson Back (UFSC)
Nestor Alberto Zouain Pereira (COPPE/UFRJ)
Nivaldo Lemos Cupini (UNICAMP)
Paulo Rizzi (ITA)
Paulo Roberto de Souza Mendes (PUC/RJ)
Raul Feijóo (LNCC)
Renato M. Cotta (COPPE/UFRJ)
Samir N.Y. Gerges (UFSC)
Valder Steffen Jr. (UFU)

Publicado pela / Published by

ASSOCIAÇÃO BRASILEIRA DE CIÊNCIAS MECÂNICAS, ABCM /
BRAZILIAN SOCIETY OF MECHANICAL SCIENCES

Secretária da ABCM: Sra. Simone Maria Frade
Av. Rio Branco, 124 - 18º Andar - Rio de Janeiro - Brasil
Tel. (021) 221-6177 R. 278, Telex (21) 37973 CGEN-BR

Presidente: Sidney Stuckenbruck
Secret. Geral: José Luiz de França Freire
Diretor de Patrimônio: José Augusto Ramos do Amaral
Vice-Presidente: Luiz Bevilacqua
Secretário: Tito Luiz da Silveira

PROGRAMA DE APOIO À PUBLICAÇÕES CIENTÍFICAS

MCT

CNPq

finep

RBCM - J. of the Braz.Soc.Mech.Sc.
Vol. XI - nº 3 - pp. 183-196 - 1989

ISSN 0100-7386
Impresso no Brasil

THERMAL SIMULATION OF MINE TUNNELS

SIMULAÇÃO TÉRMICA DE TÚNEIS DE MINAS

José Maria Saiz Jabardo - Membro da ABCM
EPUSP - Departamento de Engenharia Mecânica
Av. Prof. Mello de Moraes, 2231
São Paulo, SP - Brasil - CEP 05.508

Celso Luís Mesquita Ribeiro
EPUSP - Departamento de Engenharia de Minas e
Instituto de Pesquisas Tecnológicas - IPT/SP
São Paulo, SP - Brasil - CEP 05.508

ABSTRACT

A mathematical model has been developed for the determination of thermal conditions in mine entries in a general effort to simulate operating conditions in mining networks. The time dependence of the rate of heat transferred from the rock has been handled through a numerically obtained Time Factor. It has been shown that the Time Factor deviates from the previously accepted characteristics. A Wetness Factor, as introduced by Amano, has been included in the model to handle partially wet rock surface problems. Preliminary analysis of the obtained results underlines the adequacy of the proposed model.

Keywords: Mines ▪ Tunnels ▪ Thermal Simulation ▪ Ventilation

RESUMO

Um modelo matemático para a determinação das condições ambientais em túneis de minas foi desenvolvido no âmbito de um esforço mais geral de simulação das condições operacionais de redes de túneis em minas. A variação temporal da taxa de transferência de calor da rocha foi possível graças à introdução de um Fator Tempo, o qual mostrou características diferentes daquelas que anteriormente se admitiam como válidas. O problema da superfície da rocha parcialmente molhada foi incluído no modelo pela introdução do Fator de Umidade, anteriormente sugerido por Amano. Análises preliminares dos resultados apontam para uma adequação do modelo proposto.

Palavras-chave: Minas ▪ Túneis ▪ Simulação Térmica ▪ Ventilação

---

Submetido em Outubro/88 **Aceito em Julho/89**

INTRODUCTION

Thermal conditions in mining networks have been investigated for quite a long time, specially in applications where significant heat generation may occur. Severe thermal conditions in working areas affect productivity and the health of people exposed to such an environment for a long period of time. Thus, it is important to predict conditions which may occur during mining operations in order to provide means of reducing temperature and humidity to adequate levels. In those cases where there is intense heat and humidity generation such prediction is not easy due to the complexity of mine operation. Several simulation programs have appeared in the last thirty years, all of them based upon models of the mine network [1], [2], [3]. One of them, developed by AMANO and co-workers, [3], has been successfully applied to the predictión of thermal conditions in mine networks. The main contribution of the procedure developed by AMANO et al is related to the heat and mass transfer mechanism from the rock to the air in underground mines. Even though different sources of heat and humidity may be present, the one originated from the rock may be important and difficult to evaluate. The present work is based upon a mine network simulation program developed at the Escola Politécnica of the University of São Paulo, Brazil. The aspects of that program referred to in this paper are related with thermal simulation of an underground mine. The basis for that simulation is the above mentioned work by AMANO et al [3]. However, a different approach was adopted, since the heat transfer from the rock was obtained from a numerical procedure, from which qualitatively different results were obtained when compared to those by AMANO et al [3].

THE MODEL

General Considerations. As it has been mentioned in the Introduction, the mechanism of heat and mass transfer to the air in a bore of a mine is a very complex one. In order to make it amenable to a feasible analysis, some simplifying assumptions have to be made. In this work most of the assumptions previously made by AMANO et al [3] have been adopted.

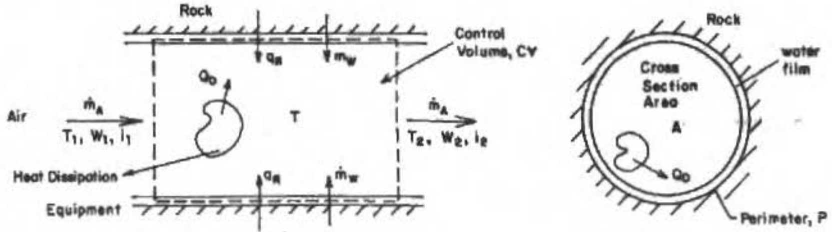

Figure 1. Geometry associated to the model of a mine entry

The associated geometry of the problem is shown in Figure 1, where the most significant parameters of the heat and mass transfer mechanisms are included. The main assumptions made in the development of the model are the following:

1) The entry presents a constant cross section, and its length is divided in equal volume regions of length L. One of those regions is displayed in Figure 1. The length L will be discussed later on in the paper.
2) Transport properties of the rock and the air are considered to be constant.
3) The wall of the entry is assumed to be covered with a thin layer of water. This assumption will be discussed later.
4) The air in the mine network is assumed to present no thermal inertia effects. This does not imply that the system operates under steady state conditions.

If heat and mass balances for the control volume (CV) of Figure 1 are performed, the following equations may be obtained:

$$q_R(PL) + Q_D = \dot{m}_A(i_2 - i_1) - \dot{m}_W i_W \tag{1}$$

$$\dot{m}_W = \dot{m}_A(\omega_2 - \omega_1) \tag{2}$$

where q_R, in W/m^2, is the heat flux from the rock, i refers to the enthalpy, and ω to the humidity ratio of the air. $\dot{m}$ refers to the mass flow rate, whereas Q_D includes the heat dissipated by machines, lights, etc. Subscripts 1 and 2 designate the entrance and exit of the CV respectively, and subscripts A and W designate air and water respectively. The above equations should be complemented by rate equations, such as:

$$q_R = \frac{h_c}{c_{p_u}} (i_I - i) \tag{3}$$

$$i = (i_1 + i_2)/2 \tag{4}$$

$$\dot{m}_W = h_{cm} (\omega_I - \omega) (PL) \tag{5}$$

$$\omega \approx (\omega_1 + \omega_2)/2 \tag{6}$$

where h_c and h_{cm} stand for the heat and mass transfer coefficients, c_{pu} is the humid air constant pressure specific heat, and the subscript I designates conditions in the air at the water-air interface. In the development of Eq. (3) it has been assumed that the Lewis

Relation for air-steam mixtures is very close to one [4], [5]. Under this assumption the convective mass transfer can be determined from the following relation:

$$h_{cm} = \frac{h_c}{c_{p_u}} \tag{7}$$

The solution of the set of Equations (1) to (7) will lead to the exit and air-water interface conditions of the CV of Figure 1. However, the value of the rate of heat dissipated by equipment in the CV must be estimated, as well as the enthalpies of the air and the heat flux from the rock, q_R. Q_D can be evaluated from information about the equipment operating in the area, and the effect of auto-compression*, related to gravity. The term q_R will be discussed in the next section. With respect to the enthalpies, the following psychrometric relation can be used to relate the humid air entalph to the temperature and humidity ratio:

$$i = c_{PA}\,T + (a + c_{PV}\,T)\,\omega \tag{8}$$

Where the subscripts A and V of the specific heat designate air and steam, and a is a numerical constant.

Heat Transfer from the Rock. The heat transferred to the air is dependent on the temperature gradient in the rock at the surface. The law which governs the conduction heat transfer in the rock is the so-called Poisson Law. If heat conduction effects in the entry direction are neglected, that law can be written as:

$$\frac{\partial T}{\partial t} = \alpha\left(\frac{\partial^2 T}{\partial r^2} + \frac{1}{r}\,\frac{\partial T}{\partial r}\right) \tag{9}$$

where α is the thermal diffusivity of the rock. Figure 2 can be used as reference for the heat conduction problem. Equation (9) involves time variation effects, and to solve it, initial and boundary conditions must be provided. Those conditions will be established here, through the following arguments:

1) The rock is assumed to be at a uniform temperature, T_0, at the beginning of the mine operation.

2) The surface is assumed to be dry for the moment.

---

*Auto-compression is the term used in mining engineering to designate the rising in the temperature of the air when it flows from the mine entrance (at a high level) to the tunnel under consideration (at a lower level).

3) The air in the entry is assumed to be blown constantly at a temperature T_A. Thus, the entry operates as a heat sink for the rock, progressively cooling it. As a result the temperature in the rock will diminish with the time.

4) The rock is assumed to be of infinite thickness, so that the temperature at the furthermost regions will remain unchanged, and equal to T_0.

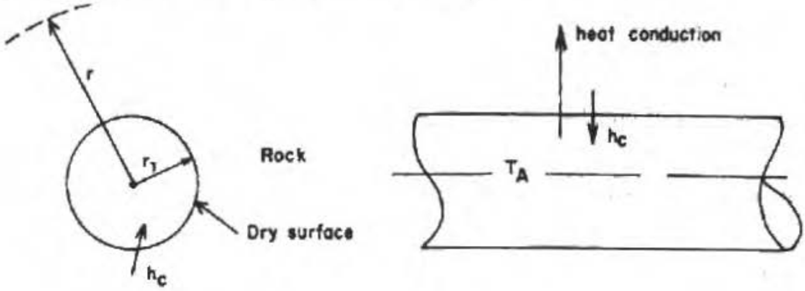

Figure 2. Geometry of the heat conduction problem

Given the aforementioned arguments, the boundary and initial conditions associated to Eq. (9) can be written as:

$$t = 0 \qquad T = T_0$$

$$t > 0 \qquad r = r_1 \qquad k\,\frac{\partial T}{\partial r} = h_c\,(T_{r=r_1} - T_A) = q_R \tag{10}^*$$

$$r \to \infty \qquad T = T_0$$

where k stands for the thermal conductivity of the rock.

In order to simplify the procedure for the evaluation of the heat flux at the surface, the procedure suggested by AMANO [3] has been adopted in this work, according to which a TIME FACTOR, f_t, is defined such that:

$$f_t = \frac{r_1\left(\frac{\partial T}{\partial r}\right)_{r=r_1}}{T_0 - T_s} \tag{11}$$

Under those circumstances, the heat flux at the rock surface can be determined from the following equation:

*For the sake of simplicity, $T_{r=r_1}$ will be substituted for T_S, designating the temperature at the surface of the rock.

$$q_R = kf_t(T_0 - T_S)/r_1 \tag{12}$$

The Time Factor is dependent upon the rock Biot number, $h_c r_1/k$, and time. It must be noticed that in Eq. (12), T_S is also time dependent. T_S will be obtained from the solution of the system in section 2, whereas the Time Factor can be determined beforehand. The procedure for that will be developed in the next section.

The question that remains to be answered is the one related to the procedure when the wall is completely wet, as it has been assumed in the previous section. In that case, under the assumption of negligibly small thermal resistance of the water film, the boundary conditions associated to Eq. (9) could be written as*:

$$r = r_1 \qquad q_R = k\left(\frac{\partial T}{\partial r}\right) = \frac{h_c}{c_{p_u}}(i_I - i) \tag{13}$$

$$r \to \infty \qquad T = T_0$$

Under the form that it is presented, Eq. (13) is cumbersome to deal with, since the surface temperature does not appear explicitly. Thus, a combined heat and mass transfer coefficient could be defined, h_f, in such a way that:

$$h_f = \frac{h_c}{c_{p_u}}\frac{(i_I - i)}{(T_S - T_A)} \tag{14}$$

and

$$q_R = h_f(T_S - T_A) \tag{15}$$

Thus, instead of working with Eq. (13), one may use Eq. (15), and the problem becomes formally alike to the dry wall one. The only difference is related to the heat transfer coefficient, which in this case is h_f, and in the former is h_c. One may argue that h_f may vary with time, since it is dependent upon the mass transfer rate. Table 1 was included to display the h_f variation for different conditions at the water film. The air temperature was assumed to be equal to 20°C and its enthalph 40 kJ/kg. The other assumed parameters were: the entry radius, r_1, and thermal conductivity of the rock, k, which were assumed equal to 1.5 m and 2.5 W/m^0K, respectively.

It can be noticed that the maximum h_f variation is 27.9%, for both h_c's adopted. That figure is acceptable if one considers that the film temperature for which h_f presented the highest deviation is very close to the air temperature. In cases where the air and film temperatures were very close, the variation of h_f would be even smaller than in the case above.

---

*The initial condition remains unchanged.

Partially wet walls have also been considered by introducing a Wetness Factor, Ψ, as in AMANO et al [3]. The Wetness Factor is defined as the ratio between the rates of evaporation of water in a partially wet wall and in a wet wall. Since those rates are given by the following equations:

· Wet Wall: $(\dot{m}w)_W = h_c \frac{2\pi L}{c_{p_u}} r_1(\omega_I - \omega)$

· Partially Wet Wall: $(\dot{m}w)_{PW} = \dot{m}_A(\omega_2 - \omega_1)_{Real}$

Table 1. h_f values for different water film temperatures

$T_S\ (^oC)$			$h_f (W/m^2\,^oC)$	
			$h_c = 6.2\ W/m^2\,^oC$	$h_c = 29\ W/m^2\,^oC$
40	166.6	1.054	37.24	177.2
35	129.4	1.045	35.37	168.3
30	100.0	1.041	35.72	170.0
25	76.5	1.034	45.24	215.2

the wetness Factor can be written as:

$$\Psi = \frac{\dot{m}_A\, c_{p_u}(\omega_2 - \omega_1)_{Real}}{2\pi\, L r_1\, h_c\,(\omega_I - \omega)} \tag{16}$$

The definition for Ψ adopted by AMANO et al is not apparent. However, it is interesting from the practical point view, since $(\omega_2 - \omega_1)_{Real}$ may by measured, whereas $(\omega_I - \omega)$, for a wet wall, can be theoretically determined. Thus, Ψ can be experimentally evaluated. As it has been shown in [3], the above defined Wetness Factor can be used to determine the average wall temperature of a partially wet wall. Thus,

$$(T_S)_{PW} = (1 - \Psi)\,(T_S)_D + \Psi(T_S)_W \tag{17}$$

Where the subscripts D,W and PW stand for dry, wet and partially wet walls respectively. Since both, $(T_S)_D$ and $(T_S)_W$ can be determined through the proposed model for given entrance characteristics of the air, for a partially wet wall the average wall temperature can be evaluated by Eq. (17).

To conclude this section it must be noted that the heat transfer from the rock is evaluated by a previous determination of the Time Factor, which depends upon a non-dimensional time parameter, the Fourier Number, and the aforementioned Biot number. It must be stressed that the air temperature is assumed to be constant throughout the transient process in the rock. Thus, when the system of Equations (1) to (7) is solved along with either, Eq. (10) or Eq. (15), the heat transfer from the rock is evaluated as if the obtained air temperature, T_A, were constant throughout the life of the mine. The real process does not happen that way, since the air temperature varies gradually with the time.

NUMERICAL EVALUATION OF THE TIME FACTOR

The Time Factor, f_t , was introduced in the last section without mentioning the procedure to obtain it. Speaking in general terms, f_t may be evaluated by solving Eq. (9), and then introducing the adequate parameters into the definition equation, Eq. (11). AMANO et al [3] sought an analytical solution of Eq. (9). That solution was given in terms of Fourier series of Bessel Functions, as it should be expected for a cylindrical geometry like the one under consideration. In this work, the authors adopted a numerical solution for the problem. Several algorithms have been considered either for Eq. (9) discretization or the evaluation of the temperature gradient at the rock surface. The most adequate procedure in terms of mesh size and processing time has been found to be the Finite Volumes one [5]. According to that procedure the domain is devided in finite volume cylindrical cells, as it is shown in Figure 3. A heat balance for each cell leads to the following set of non-dimensional equations:

. Cell 1, $i = 1$

$$\Theta'_1 = \frac{\Delta\tau}{(\Delta x)}\left(\frac{2}{\Delta x} + 1\right)\Theta_2 + \left\{1 - \frac{\Delta\tau}{\Delta x}\left(2Bi + \frac{2}{\Delta x} + 1\right)\right\}\Theta_1 + 2\,\frac{Bi\,\Delta\tau}{\Delta x} \tag{18}$$

. Internal Cells, $i > 1$

$$\Theta'_i = \frac{\Delta\tau}{(\Delta x)^2}\left(1 + \frac{\Delta x}{2x_i}\right)\Theta_{i+1} + \left(1 - \frac{\Delta x}{2x_i}\right)\Theta_{i-1} + \left(1 - \frac{2\Delta\tau}{(\Delta x)^2}\right)\Theta_i \tag{19}$$

Where

Δr = radial dimension of the cells = $(r_{lim} - r_1)/N$, N is the number of cells

$\Delta x = \Delta r / r_1$

$\tau = \alpha t / r_1^2$ = Fourier Number, α is the thermal diffusivity of the rock

$\Delta\tau$ = non-dimensional time discretization

$$\Theta_i = \frac{T_i - T_0}{T_A - T_0} \qquad \Theta'_i = \Theta_i\,(t + \Delta t)$$

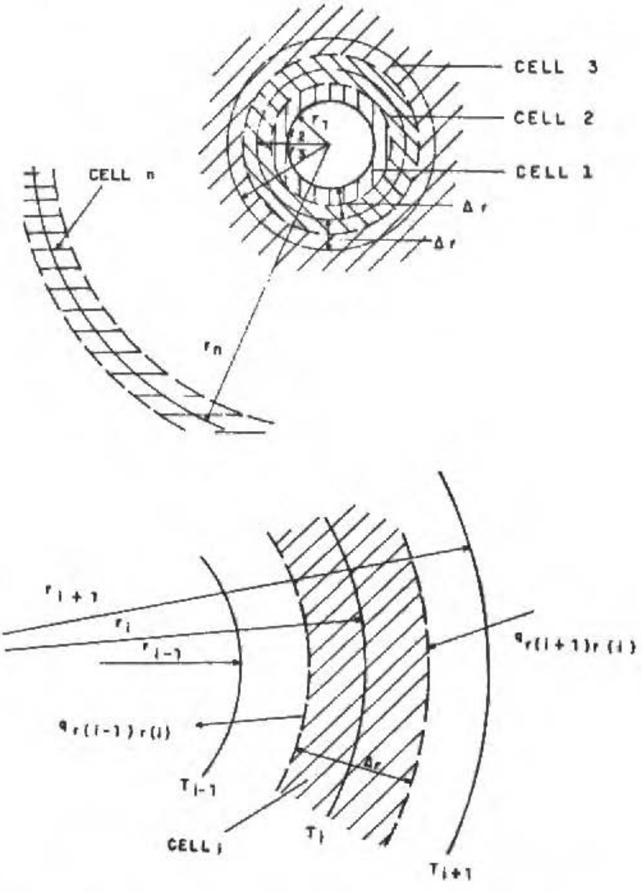

Figure 3. Finite volume cells for the numerical procedure

At this point, it should be noted that the numerical procedure requires a finite region, whereas the model assumes an infinite region. The procedure adopted in this work was to assign the boundary condition at infinity to a region sufficiently apart from the surface, such that its temperature will remain unchanged. Tests were conducted to determine such a region, and it has been found that a total of 80 cells is adequate for a non-dimensional mesh size, Δx, of 0.25.

Equations (18), (19) are typical of an explicit numerical procedure, according to which the temperature ahead of time can be determined completely from previous temperatures. Explicit algorithms are very simple, but they require the introduction of a stability criterion, such as the one due to Lax-Ritchmyer, according to which the necessary condition for stability is that.

$$a_{\Theta_i} \geq 0 \tag{20}$$

Where a_{Θ_i} is the coefficient of the temperature of the cell at a previous time, that is, the coefficient of Θ_i in Eqs. (18), (19). That criterion was adopted in this work to determine the required maximum of the time increment for stability.

The numerical evaluation of the Time Factor was performed through an equation which was obtained from its definition equation, Eq. (11), as follows:

$$f_t = \frac{r_1\left(\frac{\partial T}{\partial r}\right)_{r=r_1}}{T_0 - T_s} = \frac{h_c r_1}{k}\,\frac{T_S - T_A}{T_0 - T_S} \tag{21}$$

Adequate manipulation of Eq. (21), and the introduction of the non-dimensional temperature at the first cell, Θ_1, leads to the following equation:

$$f_t = Bi\cdot(1/\Theta_1 - 1) \tag{22}$$

That simple equation reduces the determination of the Time Factor to the evaluation of the temperature of the first cell, at the surface of the rock. The results are shown in Figure 4, where curves of the Time Factor are plotted as a function of the intervening parameters: Fourier and Biot numbers. It has been found that the curves presented in Figure 4 are similar to those by AMANO et al [3], but they present a trend for the Biot number effect which is the opposite of that suggested in [3]. Exaustive tests were conducted in the numerical procedure to cross-check the obtained results. Those tests confirmed the results displayed in Figure 4 [6].

The analytical solution obtained by AMANO et al [3] involves an infinite series of orthogonal Bessel Functions, and it was presented in graphical form. In the process of evaluating numerically those series, significant errors may be introduced ignoring some small value terms of the series. On the other hand computationally speaking, the numerical procedure is simpler, and it can be easily handled by a personal computer. It must be noted that the graphical presentation of the time factor is not fitted for using in the simulation procedure. Instead, an equation in terms of the Biot and Fourier numbers must be developed for it. That equation was obtained in this work by correlating the numerical results in terms of exponential equations, which were associated to elevated correlation coefficients (close to 1). Finally, it must be observed that the above mentioned discrepancies in trends must not be caused by the numerical procedure, since reduced mesh sizes and different boundary conditions treatment have shown the very same trend. It must be recognized, at this point, that the analytical solution must be worked out to definitely confirm the obtained results. This will be the subject of a future paper.

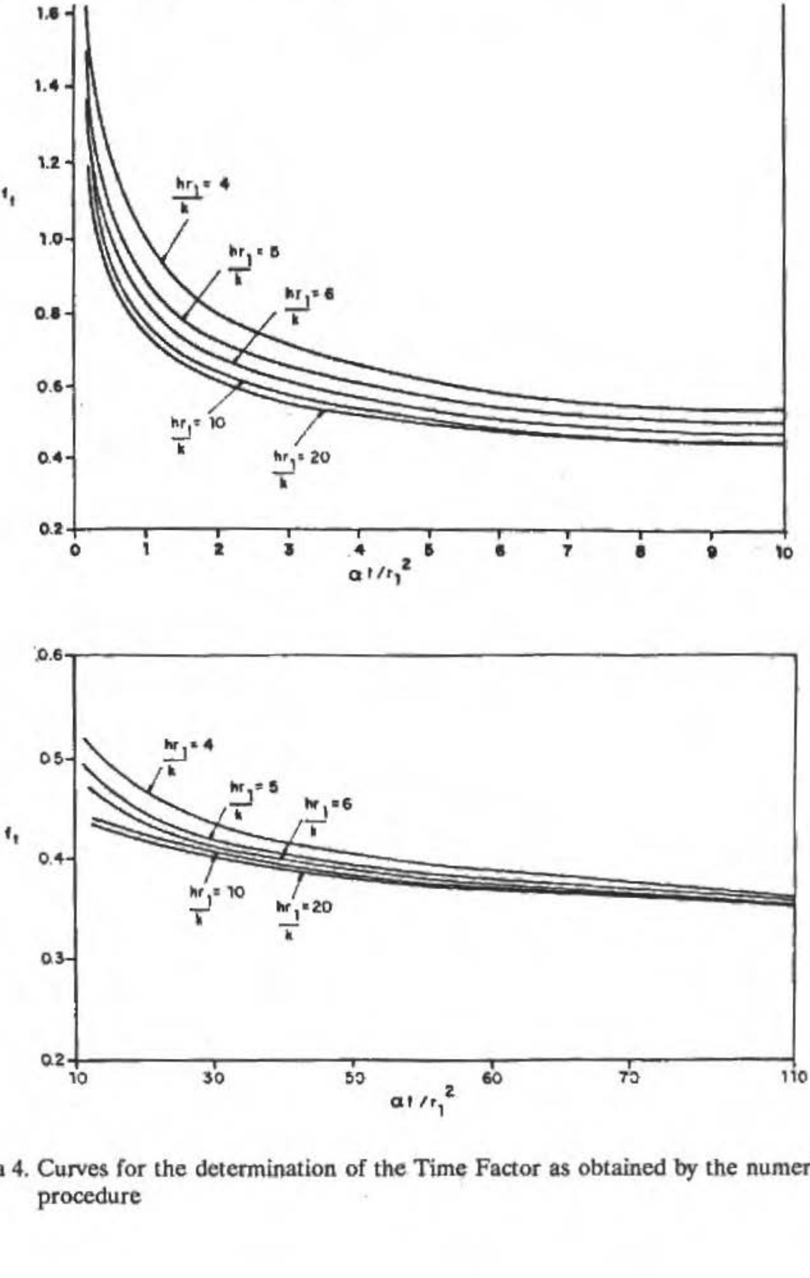

Figura 4. Curves for the determination of the Time Factor as obtained by the numerical procedure

THERMAL SIMULATION OF A SINGLE TUNNEL

The proposed model has been applied to the thermal simulation of a coal mine in operation in the south of Brazil.

A detailed description of the simulation program can be obtained in Reference [6]. In this work only the thermal simulation of a single tunnel will be considered. The first step in the tunnel simulation was to establish the optimum cell length, L (see Figure 1). That lenght was obtained by observing the effect of the cell length over the exit conditions of the air. That analysis allowed us to stablish that the maximum length which produced no significant effect over exit conditions was of the order of 50 m. Cell length above that figure would affect significantly exit conditions of the air. On the other hand, lower values of that length would increase computation time with no tangible improvement of the results. Tables 2 and 3 illustrate the obtained results for a tunnel under partially wet $(\Psi = 0.6)$ and wet wall conditions. The tunnel was assumed to be of 1000 m length with the following characteristics:

- Rock initial uniform temperature: 50^oC
- Entry radius: 1.1 m
- Air mass flow rate: 16.3 kg/s
- Inlet air temperature: 20^oC
- Inlet air humidity ratio: 6.43×10^{-3}
- Barometric pressure: 101.6 kPa
- Thermal conductivity of the rock: 3.6 W/moC
- Thermal diffusivity of the rock: $2.5 \times 10^{-6} m^2/s$
- Operation time of the tunnel: 720 h

Results shown in the above tables can be summarized as follows:

1) The rock surface is cooled in a relatively short period of time (1 month).
2) As the wetness of the rock increases, the wall temperature is reduced, due to mass transfer effects. Those effects are apparent at the tunnel entrance, where the wall temperature is lower than that of the air.
3) As the humidity of the air increases along the tunnel, mass transfer effects are reduced. That trend can clearly be observed from the variation of the Relative Humidity.
4) As the wetness of the wall increases, the outlet air temperature is reduced, whereas its humidity is increased.

The qualitative trends above were not compared to experimental results, since they were not available. However, mine network simulation compared fairly well with measurements obtained in the aforementioned mine [6], indicating that the proposed model is adequate.

Table 2. Wall temperature and humidity and temperature of the air along a 1000 m of tunnel. $L = 50\ m; \Psi = 0{,}6$ (partially wet wall)

Distance (m)	Wall Temperature (^oC)	Air Temperature (^oC)	Relative Humidity (%)	Humidity. Ratio (Kg/Kg)
100	18.7223	19.35359	56.4111	7.85241E-03
200	19.17284	19.23165	65.35897	9.046181E-03
300	19.73907	19.43938	71.79689	1.008367E-03
400	20.36707	19.84922	76.34665	1.101461E-02
500	21.02244	20.37797	79.52936	1.187207E-02
600	21.68354	20.97175	81.77988	1.267802E-02
700	22.33708	21.59596	83.38055	1.344702E-02
800	22.97514	22.22868	84.54854	1.418873E-02
900	23.5933	22.85632	85.42363	1.490955E-02
1000	24.18938	23.47067	86.11313	1.561371E-02

Table 3. Wall temperature and humidity and temperature of the air along a 1000 m tunnel. $L = 50\ m; \Psi = 1$ (wet wall)

Distance (m)	Wall Temperatura (^oC)	Air Temperature (^oC)	Relative Humidity (%)	Humidity Ratio (Kg/Kg)
100	15.62092	17.88512	67.35446	8.561815E-03
200	16.65716	17.2677	81.96003	1.004483E-02
300	17.62002	17.4016	90.31484	1.118242E-02
400	18.52041	17.90174	94.82011	1.213466E-02
500	19.36632	18.56933	97.17038	1.298582E-02
600	20.16388	19.30247	98.37832	1.378007E-02
700	20.91802	20.04955	98.98596	1.454052E-02
800	21.63283	20.7852	99.28391	1.527926E-02
900	22.31175	21.49764	99.42914	1.600259E-02
1000	22.95781	22.18202	99.48343	1.671379E-02

CONCLUSIONS

A mine tunnel has been thermally simulated in an effort to develop a simulation program for mine networks. A simple yet accurate model has been proposed, based upon a model previously proposed by AMANO et al [3]. Heat transfer from the rock has been numerically determined. Exaustive numerical tests have shown that trends for the Time Factor obained in this work are opposite to those suggested by AMANO et al. Thermal simulation of a tunnel has shown that the results are qualitativelly sound. However, given that experimental data were not available, it was not possible to cross-check simulation results. The tunnel model has been applied to the simulation of an operating mine for which experimental measurements have been raised. The results indicate the adequacy of the proposed model.

REFERENCES

[1] AMANO, K.; MIZUTA, Y; HIRAMATSY, Y. - An improved method of predicting underground climate, Int.J. Rock Mech.Sci., 19:31-37, 1982.

[2] STARFIELD, A.M. & DICKSON, A.J. - A study of heat transfer and moisture pickup in mine airways, J.S.Afr.Inst.Min.Metal., Norshalltown, 68(5): 211-234, Dec., 1967.

[3] AMANO, K. & HIRAMATSU, Y. - Calculation of the rate of flow, temperature and humidity of air currents in a mine, Int.J. Rock Mech.Min.Sci., 9:713-727, 1972.

[4] STOECKER, W.F. & JONES, J.W. - Refrigeração e ar condicionado, São Paulo, MacGraw-Hill, 481 p.il., 1985.

[5] THRELKELD, J.L. - Thermal environmental engineering, Prentice-Hall, Englewood Clifs, N.Y., 1970.

[6] RIBEIRO, C.L.M. - Sistema computacional para previsão das condições ambientais em minas subterrâneas, M.Sc. Thesis, Escola Politécnica da Universidade de São Paulo, Set., 1988.

RBCM - J. of the Braz.Soc.Mech.Sc.
Vol. XI - nº 3 - pp. 197-209 - 1989

ISSN 0100-7386
Impresso no Brasil

GRAVITY-DRIVEN MOTION OF A FLUID LAYER AROUND A CYLINDER

MOVIMENTO DE UMA CAMADA DE LÍQUIDO EM TORNO DE UM CILINDRO HORIZONTAL DEVIDO À AÇÃO DA GRAVIDADE

Paulo Roberto de Souza Mendes - Membro da ABCM
PUC/RJ - Departamento de Engenharia Mecânica
Rua Marquês de São Vicente, 225 - Gávea
Rio de Janeiro, RJ - Brasil - CEP 22.453

ABSTRACT

A theoretical investigation of the motion of a layer of a viscous fluid around a horizontal cylinder is reported in this paper. The layer has initially a uniform thickness, and, at some instant of time, it starts to flow due to the presence of a gravity field. The result sought is the film thickness as a function of time and angular position. The mass- and momentum-conservation principles are employed in conjunction with the integral method, and a system of two non-linear hyperbolic equations is shown to govern the problem. The results show that the flow tends to an equilibrium configuration where the fluid weight is balanced by the surface tension effects. For low viscosity fluids, an oscillatory motion is observed, which remains until all the kinetic energy is dissipated by the viscous effect.

Keywords: Wire Coating ▪ Integral Methods ▪ Surface tension

RESUMO

Um estudo teórico do movimento de uma camada de um fluido viscoso em torno de um cilindro horizontal é relatado neste artigo. A camada tem inicialmente uma espessura uniforme, e, em um dado instante, começa a escoar por ação de um campo gravitacional. O resultado almejado é a espessura do filme como função do tempo e da posição angular. Os princípios de conservação de massa e de momentum são utilizados em conjunto com um método integral, e mostra-se que um sistema de duas equações diferenciais hiperbólicas não-lineares governa o problema. Os resultados mostram que o escoamento tende a uma configuração de equilíbrio onde o peso do fluido é contrabalançado pelos efeitos de tensão superficial. Para fluidos de baixa viscosidade, um movimento oscilatório é observado, o qual permanece até que toda a energia cinética seja dissipada pelo efeito viscoso.

Palavras-chave: Esmaltamento de Fios ▪ Métodos Integrais ▪ Tensão Superficial

---

Submetido em Novembro/88 Aceito em Junho/89

INTRODUCTION

An effective simulation of coating processes of electrical wires is still an unresolved question. The processes employed do not perform satisfactorily, and therefore need improvement. However, the physical mechanisms involved are very complex, and a model that is both realistic and amenable to mathematical solution is yet to be developed.

Specifically, for horizontal wire coating, the gravity effect causes the liquid coating material previously deposited to flow down around the wire before solidification. This causes eccentric layers of deposited material, which is highly undesirable.

Therefore, prediction of the fluid motion arround the wire is necessary to control the eccentricity of the deposited layer of electrical insulation.

Coating processes have deserved some attention in the fluid mechanics literature. TAYLOR [1] proposed the so-called paint brush model to simulate the deposition of a fluid on a plane surface. SAVAGE [2] employed the lubrication theory to study the flow of a newtonian fluid in the narrow gap between a pair of rollers of different radii and at different peripheral speeds. His predictions for the film thickness were found to compare well with experiments.

KISTLER and SCRIVEN [3] described a number of valuable computational strategies to tackle coating flows. Predictions based on two different theories, one based on asymptotic expansions and the other on the full solution of the Navier-Stokes equations, are compared with the predictions of the lubrication theory for flows in forward-roll coating [4], and it was concluded that the latter theory is realistic only for high capillary numbers.

The coating process of a cylindrical wire moving in its axial direction, however, has not been addressed to date. The present research is focused on the issue of controlling the eccentricity of the deposited layer. The physical model is depicted in Figure 1. At time $t^* = 0$, a fluid layer of uniform thickness δ_0^* is deposited around a horizontal cylinder (or wire), and a gravity field $\vec{g}$ directed downward is switched on (Figure 1a). At some later time t^*, the

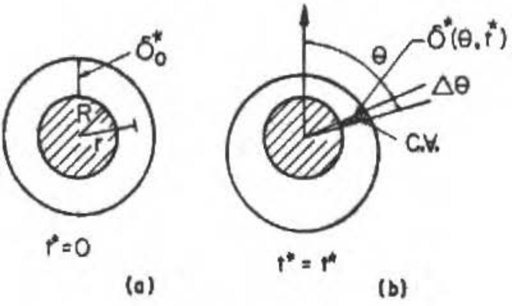

Figure 1. The physical model

flow has moved downward due to gravity (Figure 1b), and surface tension effects together with viscous forces tend to decelerate the motion. For the sought-for application, the film thickness is typically very small, generally of the order of 1 or 2% of the wire radius.

THE ANALYSIS

The principles of mass and θ-momentum conservation are evoked, and applied to the deformable control volume shown at some instant t^* in Figure 2.

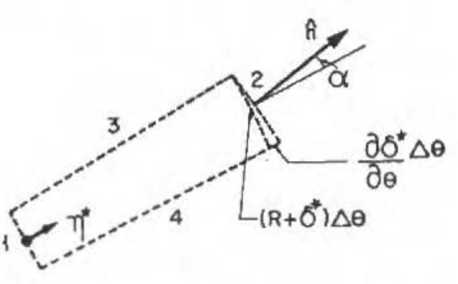

Figure 2. Magnification of the deformable control volume

In this two-dimensional analysis, the fluid density ρ is assumed to be invariant. The velocity field is given by $\vec{u} = u^* \hat{e}_r + v^* \hat{e}_\theta$. V^* stands for the velocity component v^* evaluated at the interface, i.e.,

$$V^*(\theta, t^*) \equiv v^*(R + \delta^*, \theta, t^*) \tag{1}$$

where $\delta^*(\theta, t^*)$ is the film thickness, measured in the radial direction, at some instant of time and θ location.

There exists a pressure difference Δp^* across the interface, due to the surface tension. Since the present study is focused on very thin films $(\delta^* << R)$, the curvature radius of the interface is nearly constant and close to $R + \delta_0^*$, where δ_0^* is the initial (and uniform along θ) film thickness. Therefore, if σ is the surface tension,

$$\Delta p^* = \frac{\sigma}{R + \delta_0^*} \tag{2}$$

Mass Conservation. The continuity equation for the control volume shown in Figure 2 is ($\vec{n}$ is the unitary vector normal to the control surface):

$$0 = \int_{CS} \vec{u} \cdot \hat{n}\, dA = \int_{1} \vec{u} \cdot \hat{n}\, dA + \int_{2} \vec{u} \cdot \hat{n}\, dA + \int_{3} \vec{u} \cdot \hat{n}\, dA + \int_{4} \vec{u} \cdot \hat{n}\, dA \tag{3}$$

At surface 1, $\vec{u} = 0$, and hence $\int_{1} \vec{u} \cdot \hat{n}\, dA = 0$. At surface 2,

$$\vec{u} = \frac{d\delta^*}{dt^*}\, \hat{e}_r + V^* \hat{e}_\theta \quad \text{and} \quad \hat{n} = \cos\alpha\, \hat{e}_r - \sin\alpha\, \hat{e}_\theta\,. \tag{4}$$

Then, at surface 2,

$$\vec{u} \cdot \hat{n} = \left(\frac{d\delta^*}{dt^*} - V^* \tan\alpha\right) \cos\alpha\ . \tag{5}$$

Now it is observed that

$$\tan\alpha = \frac{1}{R + \delta^*}\, \frac{\partial\delta^*}{\partial\theta} \quad \text{and} \quad \frac{d\delta^*}{dt^*} = \frac{\partial\delta^*}{\partial t^*} + \frac{V^*}{R + \delta^*}\, \frac{\partial\delta^*}{\partial\theta} \tag{6}$$

Substituting the above equations into Eq. (5), the dot product $\vec{u} \cdot \hat{n}$ becomes simply equal to $\frac{\partial\delta^*}{\partial t^*} \cos\alpha$, and

$$\int_{2} \vec{u} \cdot \hat{n}\, dA = \frac{\partial\delta^*}{\partial t^*}\, (R + \delta^*)\, \Delta\theta\,, \tag{7}$$

where, assuming a unitary length along the third direction, dA was substituted for by $(R + \delta^*)\, d\theta/\cos\alpha$.

It is not difficult to see that

$$\int_{3} \vec{u} \cdot \hat{n}\, dA + \int_{4} \vec{u} \cdot \hat{n}\, dA = \frac{\partial}{\partial\theta} \left[\int_{0}^{\delta^*} v^*\, d\eta^*\right] \Delta\theta \tag{8}$$

where $\eta^* \equiv r - R$.

Now, Eqs. (7) and (8) are plugged into the continuity equation (Eq. (3)), yielding

$$0 = \left(1 + \frac{\delta^*}{R}\right) \frac{\partial \delta^*}{\partial t^*} + \frac{1}{R} \frac{\partial}{\partial \theta} \left[\delta^* V^* \int_0^1 v \, d\eta\right] \tag{9}$$

where $\eta \equiv \eta^*/\delta^*$ roman and $v \equiv v^*/V^*$.

The above equation is then made dimensionless, yielding

$$0 = (1 + \delta) \frac{\partial \delta}{\partial t} + \frac{\partial}{\partial \theta} \left[V \delta \int_0^1 v \, d\eta\right] \tag{10}$$

where

$$\delta \equiv \frac{\delta^*}{R}, \quad t \equiv t^* \sqrt{\frac{g}{R}}, \quad \text{and} \quad V \equiv \frac{V^*}{\sqrt{gR}}, \tag{11}$$

g being the acceleration due to gravity.

Momentum Conservation. In the θ-direction, the principle of conservation of momentum gives, when applied to the control volume shown in Figure 2,

$$F_c + F_e = \int_{CV} \frac{\partial(\rho v^*)}{\partial t^*} \, d\mathcal{V} + \int_{CS} v^* \rho \vec{u} \cdot \hat{n} \, dA \, . \tag{12}$$

The contact forces F_c are due to the shear stress at surface 1 and to the pressure acting on surfaces 3 and 4. Then,

$$F_c = -\tau_\omega R \Delta\theta - \Delta p^* \, \frac{\partial \delta^*}{\partial \theta} \, \Delta\theta \, , \tag{13}$$

where Δp^* is given by Eq. (2). It is observed from Eq. (13) that the surface tension effect depends directly on the thickness gradient along θ, the derivative $\partial\delta^*/\partial\theta$. The shear stress at the wall τ_ω is obtained by

$$\tau_\omega(\theta, t^*) = \mu \left.\frac{\partial v^*}{\partial r}\right]_{r=R} = \frac{\mu V^*}{\delta^*} \left.\frac{\partial v}{\partial \eta}\right]_{\eta=0} \tag{14}$$

The external forces F_e are due to gravity, and hence given by

$$F_e = \int_0^{\delta^*} \rho g \sin\theta\,(R+\eta^*)\,d\theta\,d\eta^* = \rho g \sin\theta\left(R\delta^* + \frac{\delta^{*2}}{2}\right)\Delta\theta\,. \tag{15}$$

The first term on the right-hand side of Eq. (12) may be written as

$$\int_{CV} \frac{\partial(\rho v^*)}{\partial t^*}\,dV = \rho\Delta\theta \int_0^{\delta^*} \frac{\partial v^*}{\partial t^*}\,(R+\eta^*)\,d\eta^* =$$

$$= \rho g\,R^2\,\delta\Delta\theta \int_0^1 \frac{\partial(vV)}{\partial t}\,(1+\delta\eta)\,d\eta \tag{16}$$

If the same reasoning employed to obtain the mass conservation equation (Eq. (10)) is followed while working on the right-most term of Eq. (12), the expression below is obtained with no particular difficulty:

$$\int_{CS} v^*\,\rho\vec{u}\cdot\hat{n}\,dA = \rho V^*\,\frac{\partial\delta^*}{\partial t^*}\,R(1+\delta)\Delta\theta + \frac{\partial}{\partial\theta}\left[\delta^* V^{*2}\int_0^1 v^2\,d\eta\right]\rho\Delta\theta \tag{17}$$

Now Eqs. (2), (9), (12), (13), (14), (15), (16) and (17) are combined, yielding, after some algebra, the following dimensionless equation:

$$-\frac{V}{Re}\,\frac{\partial v}{\partial\eta}\Big]_{\eta=0} - \left(\frac{1}{S(1+\delta_0)}\right)\delta\,\frac{\partial\delta}{\partial\theta} + \sin\theta\left(1+\frac{\delta}{2}\right)\delta^2 =$$

$$= \delta^2\int_0^1 \frac{\partial(vV)}{\partial t}\,(1+\delta\eta)\,d\eta + \delta\,\frac{\partial}{\partial\theta}\left[\delta V^2\int_0^1 v^2\,d\eta\right] - \delta V\frac{\partial}{\partial\theta}\left[\delta V\int_0^1 v\,d\eta\right] \tag{18}$$

where

$$Re \equiv R\,\sqrt{gR}/\nu \qquad \text{and} \qquad S \equiv \rho g R^2/\sigma \tag{19}$$

Eqs. (10) and (18) are subjected to the following initial conditions:

$$V(\theta,0) = 0\,; \qquad \text{and} \qquad \delta(\theta,0) = \delta_0 \tag{20}$$

The boundary conditions are:

$$V(0,t) = V(\pi,t) = 0\,; \qquad \text{and} \qquad \frac{\partial\delta}{\partial\theta}(0,t) = \frac{\partial\delta}{\partial\theta}(\pi,t) = 0 \tag{21}$$

Evaluation of the Integral Terms. Further inspection upon Eqs. (10) and (18) reveals that there are four terms where the tangential component $v \equiv v^*/V^*$ of the velocity appears, three of them involving integrals, and the fourth involving a derivative evaluated at the wall. It is clear that the evaluation of these terms require the knowledge of the function $v^*(\eta,\theta,t)$.

In the present work, a linear profile of the form $v = a\eta + b$ was adopted. It is worth noting that this assumption is quite reasonable when $\delta << 1$, since any continuous function can be approximated by a straight line in such a small interval.

Using the facts that, at $\eta = 0$, $v = 0$, and at $\eta = 1$, $v = 1$, it is straightforward to obtain $v = \eta$. This profile is used in the four terms mentioned above, and the following results are obtained:

$$\int_0^1 v\,d\eta = \frac{1}{2}\,; \qquad \int_0^1 v^2\,d\eta = \frac{1}{3}\,; \qquad \left.\frac{\partial v}{\partial\eta}\right]_{\eta=0} = 1\,; \qquad \text{and}$$

$$\int_0^1 \frac{\partial(vV)}{\partial t}(1 + \delta\eta)\,d\eta = \left(\frac{\partial V}{\partial t} - \frac{V}{\partial}\,\frac{\partial\delta}{\partial t}\right)\left(\frac{1}{2} + \frac{\delta}{3}\right) \tag{22}$$

With the above results, the final form of the governing equations can be obtained:

$$(1 + \delta)\,\frac{\partial\delta}{\partial t} + \frac{1}{2}\,\frac{\partial(V\delta)}{\partial\theta} = 0 \tag{23}$$

and

$$V\left(\frac{1}{2} + \frac{\delta}{3}\right)\delta\,\frac{\partial\delta}{\partial t} - \left\{\left(\frac{1}{S(1 + \delta_0)}\right) - \frac{V^2}{6}\right\}\delta\,\frac{\partial\delta}{\partial\theta} -$$

$$- \delta^2\left(\frac{1}{2} + \frac{\delta}{3}\right)\frac{\partial V}{\partial t} - \frac{V\delta_2}{6}\,\frac{\partial V}{\partial\theta} = \frac{V}{\mathrm{Re}} - \sin\theta\left(1 + \frac{\delta}{2}\right)\delta^2 \tag{24}$$

The problem under study is governed by the above partial differential equations for δ and V, together with the initial and boundary conditions given in Eqs. (20) and (21).

It can be seen that the parameters that influence this physical situation are S, Re and the dimensionless initial film thickness δ_0. S is the ratio between gravity forces and forces due to surface tension, whereas the modified Reynolds number Re compares gravity forces with viscous forces.

METHOD OF SOLUTION

It can be observed that Eqs. (23) and (24) form a non-linear system of hyperbolic partial differential equations. Since no discontinuities are expected in the sought-for solution, a finite-difference scheme is, in principle, appropriate for the integration of the governing equations. In the present work, the Crank-Nicolson implicit scheme was employed to generate the albebraic discretization equations, which were solved with the aid of the Thomas algorithm together with an iterative scheme.

This iterative scheme consisted basically of, for a given instant of time, (i) assuming initial guesses for δ and V; (ii) solving the set of algebraic equations generated from Eq. (23) using the Thomas algorithm and the initial guesses for δ; (iii) solving the set of algebraic equations generated from Eq. (24) using the Thomas algorithm and the present values of V; (iv) going back to step (ii), but now using the present values of δ; (v) proceeding in this manner until convergence is achieved. The initial guesses mentioned above were just the values at the previous time step. Convergence was typically achieved in three or four iterations.

Due to symmetry, the solution domain in θ is from 0 to π. The grid employed was uniform, with 33 nodal points in θ and time steps varying from case to case in the range 0.001-10, depending upon the Reynolds number Re.

RESULTS AND DISCUSSION

Attention will now be focused on the results obtained with the just described model. Figure 3 shows the variation of the film thickness δ with the angular position θ, for the case $\delta_0 = 0.02, S = 0.2$ and $Re = 5.0$. From this figure it is seen that, at instant $t = 0$, the film thickness is uniform and equal to its initial value δ_0. As time ellapses, the fluid falls around the cylinder due to gravity, and therefore the film thickness at the upper region diminishes, whereas at the lower region the thickness increases.

However, once a thickness gradient in the θ direction is established, a force due to surface tension appears, and acts to balance the gravity effect. Furthermore, the viscous force also acts against the movement, and the overall effect is that the fluid tends asymptotically to an equilibrium configuration, where the surface tension effects exactly balance the fluid weight. This equilibrium configuration satisfies

$$\left(\frac{1}{S(1+\delta_0)}\right)\frac{d\delta}{d\theta} - \sin\theta\left(1+\frac{\delta}{2}\right)\delta = 0\ , \tag{25}$$

which expresses the equilibrium between gravity and surface-tension forces. The solution of Eq. (25) is

$$\delta(\theta,\infty) = \frac{2\delta(0,\infty)}{2+\delta(0,\infty)}\,\frac{\exp\left\{S(1+\delta_0)(1-\cos\theta)\right\}}{1-\dfrac{\delta(0,\infty)}{2+\delta(0,\infty)}\exp\left\{S(1+\delta_0)(1-\cos\theta)\right\}} \tag{26}$$

The value of $\delta(0,\infty)$ is obtained by assuring overall mass conservation i.e.,

$$2\int_0^{\pi}\delta(\theta,\infty)\left(1+\frac{\delta(\theta,\infty)}{2}\right)d\theta = \pi\left\{(1+\delta_0)^2-1\right\} \tag{27}$$

The curve in Figure 3 indicated by $t = \infty$, which was obtained via numerical integration of Eqs. (10) and (18) for large times, satisfies the analytical relation given in Eq. (26) within less than one percent. This fact strongly suggests that the numerical scheme employed performed satisfactorily. Another interesting fact that is indicated in Figure 3 is that the film thickness at an angular position of ≈ 100° is nearly independent of time, and equal to the initial thickness δ_0.

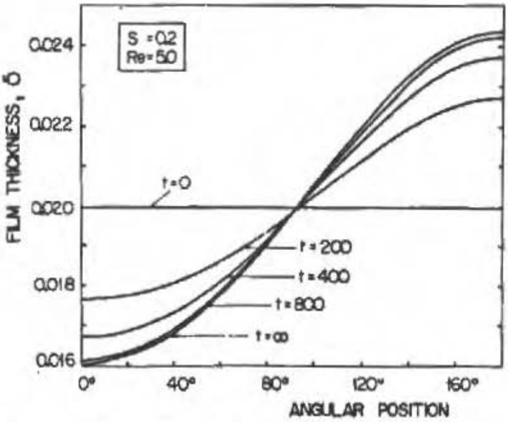

Figure 3. Film thickness versus angle for various times

The behavior of the tangential velocity at the interface is illustrated in Figure 4 for the same case shown in Figure 3. It can be seen that the fluid accelerates very fast at the onset of the motion, when the only force acting on it is gravity. Soon the surface tension and viscosity effects become important, and the velocity distribution $V(\theta, t)$ reaches maximum values at some early instant of time and then starts decreasing to zero until the equilibrium configuration is reached. It can also be seen that the location of maximum velocity happens in the range $80^{o} < \theta < 100^{o}$, depending upon the time instant.

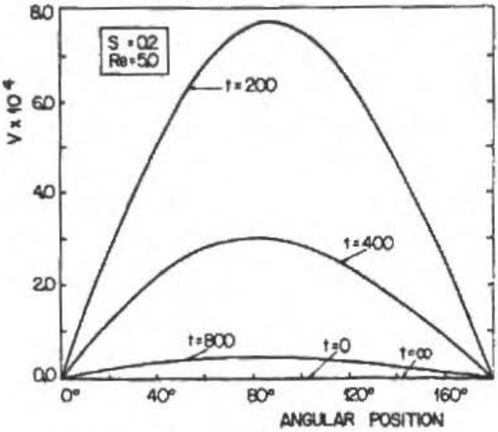

Figure 4. Tangential velocity versus angle for various times

The effect of the fluid viscosity is now addressed. Figures 5 and 6 show the variation of the film thickness at $\theta = 0^{o}$ with time, for different values of the modified Reynolds number Re. From its definition, it can be seen that low values of Re indicate high fluid viscosity, and vice-versa, for a given cylinder radius and gravity field. Figure 5 shows the cases of high fluid viscosities, whereas in Figure 6 the cases of low fluid viscosities are illustrated.

In Figure 5, it is observed that, for infinite fluid viscosity ($\mathrm{Re} = 0$), the fluid flows at infinitely small velocity, and no change in thickness is observed. As he viscosity decreases, the fluid flows faster, needing less and less time to reach the equilibrium configuration.

If the fluid viscosity gets very low (Figure 6), the viscous forces are not intense enough to dissipate at once all the fluid initial potential energy, and a damped oscillatory motion is observed ($Re = 5 \times 10^{5}$). For the extreme case of zero fluid viscosity ($Re = \infty$), the equilibrium configuration cannot be reached, since no viscous damping for the fluid kinetic energy is available.

It is worth to mention at this point that, for these cases where oscillatory motions are expected, the present simple model may not be appropriate. The reason is that it is most probable that recirculations occur, as well as sharp ripples at the interface. In fact, the case

($Re = \infty$) shown in Figure 6 refused to yield a plausible solution for larger times than the ones shown. However, even for these cases, the present model serves to generate some qualitative information that may be useful in developing more sophisticated models.

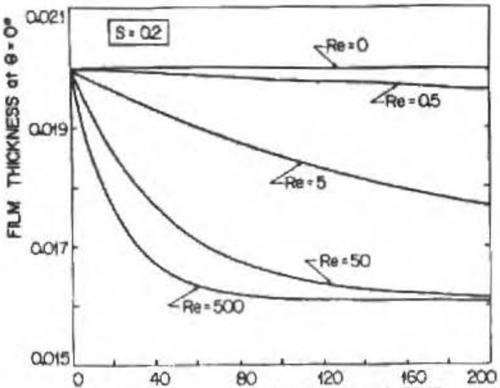

Figure 5. Film thickness at $\theta = 0^{\circ}$ versus time for various Re's

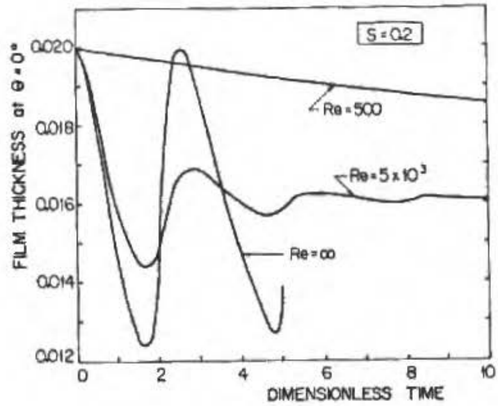

Figure 6. Film thickness at $\theta = 0^{\circ}$ versus time for various Re's

The effect of surface tension σ on the flow under study will now be analyzed. In Figure 7, the effect of the parameter S is illustrated. It can be seen that, for $S = 0$ (infinite surface tension), there is no flow, since gravity is not strong enough to move the fluid. For larger values of S, i.e., for lower values of σ, fluid motion is observed. The lower is the surface tension, the longer it takes for the fluid to reach the equilibrium configuration. Moreover, the equilibrium configuration departs further from the initial configuration of uniform

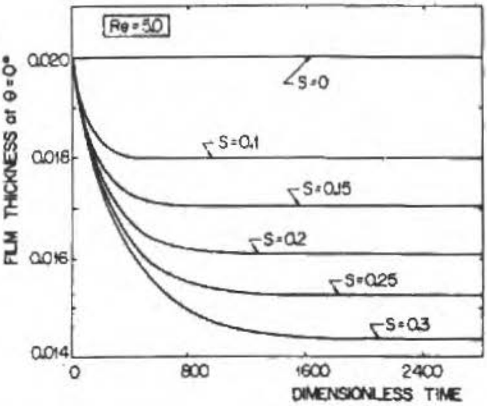

Figure 7. Film thickness at $\theta = 0^0$ versus time for various S's

thickness, since the low value of σ must be compensated for by a high variation of δ with θ, in order to balance gravity.

FINAL REMARKS

The purpose of the research reported here was to develop a simple methodology to simulate the motion of a falling film around a horizontal film, aiming at the process of wire coating. In the range of parameters that is important for this industrial process, the present simulation seems to be appropriate, lacking, however, experimental confirmation to validate the procedure. For example, from what is experimentally observed in other geometries, instability phenomena might be expected for Re values larger than ≈ 800.

It is worth to emphasize, however, that the present model is not valid for $\delta_0 \approx 1$ or larger, i.e., in the cases that the surface tension forces are never intense enough to balance with gravity. In these cases, there will be no equilibrium configuration, and the fluid will fall and separate from the cylinder.

REFERENCES

[1] TAYLOR, G.I. - Deposition of a viscous fluid on a plane surface, J. Fluid Mech. 9, pp. 218-224, 1960.

[2] SAVAGE, M.D. - Mathematical models for coating processes, J. Fluid Mech. 117, pp. 443-455, 1982.

[3] KISTLER, S.F., and SCRIVEN, L.E. - Coating flows, in computational analysis of polymer processing, edited by J.R.A. Pearson and S.G. Richardson, Applied Science Publishers Ltd., Barking, Essex, England, pp. 243-298, 1983.

[4] COYLE, D.J., MACOSKO, C.W., and SCRIVEN, L.E. - Film-splitting flows in forward roll coating, J. Fluid Mech. 171, pp. 183-207, 1986.

RBCM - J. of the Braz.Soc.Mech.Sc.
Vol. XI - nº 3 - pp. 211-246 - 1989

ISSN 0100-7386
Impresso no Brasil

A DETAILED REVIEW OF A SOLUTION PROCEDURE FOR SHOCK-WAVE TRANSPIRED TURBULENT BOUNDARY LAYER INTERACTION PROBLEMS

UMA REVISÃO DETALHADA DE UM PROCEDIMENTO DE SOLUÇÃO PARA PROBLEMAS DE INTERAÇÃO ENTRE ONDAS DE CHOQUE E CAMADAS LIMITE TURBULENTAS COM TRANSPIRAÇÃO

Átila Pantaleão Silva Freire
COPPE/UFRJ - Programa de Engenharia Mecânica
Laboratório de Mecânica dos Fluidos/Aerodinâmica
Caixa Postal 68.503 - Cidade Universitária
Rio de Janeiro, RJ - Brasil - CEP 21.945

ABSTRACT

In this work perturbation techniques are used to study the problem of the interaction between a shock wave and a transpired turbulent boundary layer at transonic speeds. In the case considered here, the Mach number is assumed to be high enough for the sonic line to penetrate deep into the boundary layer so that it ends close to the wall. A detailed analysis of the whole flow field is carried out and solutions valid in the double limit as Reynolds number tends to infinity and Mach number tends to one are proposed. The analysis yields solutions for the pressure and skin-friction profiles. In the construction of a solution for the undisturbed region ahead of the shock, a new expression is proposed for the law of the wake for transpird turbulent boundary layers.

Keywords: Turbulent Boundary Layer ▪ Transpiration ▪ Shock Wave ▪ Interaction

RESUMO

No presente trabalho, técnicas de perturbação são utilizadas para se estudar o problema da interação entre uma onda de choque e uma camada limite turbulenta com transpiração a velocidades transônicas. No caso a ser considerado, assume-se ser o número de Mach grande o suficiente para que a onda de choque penetre fundo na camada limite terminando perto da parede. Uma análise detalhada do escoamento é realizada e soluções válidas nos limites $R \to \infty$ *e* $M \to 0$ *são propostas. Esta análise prevê soluções para os perfis de pressão e de fricção. Na busca de uma solução para a região não perturbada à frente de onda de choque, propõe-se uma nova expressão para a "lei da esteira" para camadas limite com transpiração.*

Palavras-chave: Transpiração ▪ Camada Limite Turbulenta ▪ Onda de Choque ▪ Interação

Submetido em Novembro/88 Aceito em Agosto/89

INTRODUCTION

The problem of the interaction between a shock wave and a boundary layer occurs in many situations of practical importance. In aviation, examples include flow on transonic aerofoils, in supersonic air intakes, in propelling nozzles at off-design conditions, and around deflected controls at supersonic speeds. As a result, there has been a continuous interest over the past thirty years in gaining a good understanding of this problem. This has motivated a considerable number of theoretical and experimental researches into this phenomenon. This research has vastly improved our knowledge of the problem, providing a fairly good understanding of the interaction process including a number of simple rules for estimating certain of its properties; and some theoretical treatments for particular types of flow. However, the phenomenon of the interaction manifests itself in diverse forms and hence a single theoretical framework which embraces all the aspects of the problem is very difficult to develop. For example, the four practical situations described in the beginning of this section include flow over forward-facing and reward-facing steps, flow over compression corners, and interaction between normal and oblique shock waves with boundary layers. Solutions for these problems are very complex since they must account not only for the geometry of the problem but also for the nature of the boundary layer, i.e., whether it is laminar or turbulent, and for the strength of the shock. If the pressure rise across the shock is moderate the boundary layer will remain attached through the interaction, giving a situation which can be treated analytically. Once separation occurs, however, the flow pattern changes drastically [1,2,3] and analytical solutions become very difficult to obtain. Three-dimensional effects may further complicate these situations.

The aim of this work is to review in detail a solution procedure for a specific type of interaction which occurs on transonic aerofoils. The general pattern of the flow over a transonic aerofoil at constant incidence angle is shown in Figure 1 [4]. We assume that the conditions are such that the flow remains attached well beyond the point where the critical Mach number is achieved. By definition, the critical Mach number is that free-stream Mach number at which sonic line is first encountered on the aerofoil.

For M_∞ slightly higher than M_{cr}, the local Mach numbers are close to unity, a weak shock wave develops on the aerofoil and a small supersonic region forms ahead of the shock. As M_∞ increases, the shock position moves downstream, and both the size of the supersonic region and the strength of the shock increase. When the shock is sufficiently strong, boundary layer flow separation occurs. A further increase in M_∞ moves the shock to the trailing edge of the aerofoil yielding a flow pattern which is predominantly supersonic. Finally, for M_∞ much larger than unity, a detached bow wave and oblique trailing-edge shocks are produced.

The nature of the boundary layer is of fundamental importance for the definition of the pattern of the flow on the aerofoil. For situations of technological interest the transition point is located at around the 10%-chord position and therefore the shock wave normally interacts with a turbulent boundary layer. In an inviscid flow region, the pressure rise through the shock is discontinuous. However, in the inner viscous layers of the boundary layer, the flow is subsonic and hence cannot undergo a discontinuous change in pressure. The boundary layer adjusts itself so that the rise in the wall pressure is abrupt but continuous. This pressure rise thickens the boundary layer at the foot of the shock and, depending on the flow conditions, it may even detach the flow from the wall. Once separation occurs, the flow configuration changes dramatically leading to a spectacular change in the flow properties. The separated region provokes a sudden fall in the trailing edge pressure and a marked increase in wave drag, both of which seriously compromise the aerofoil's performance.

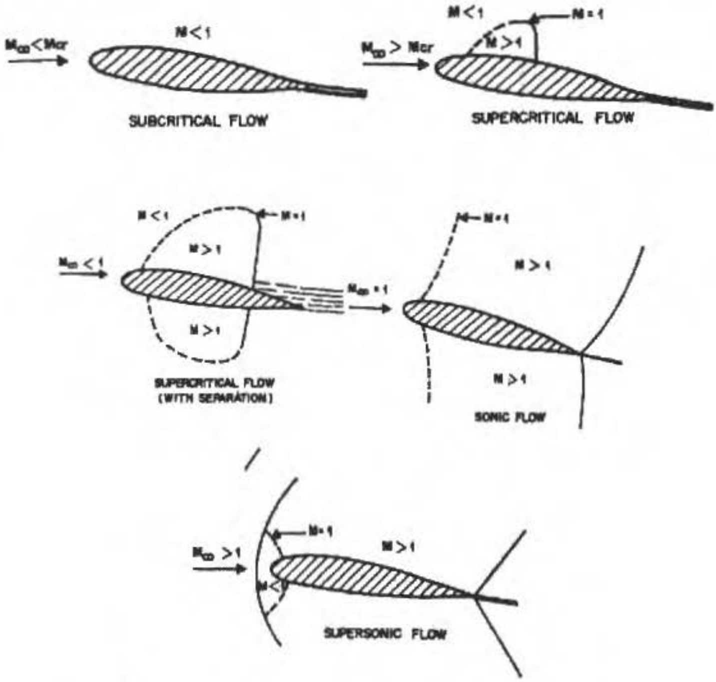

Figure 1. Flow pattern for a transonic aerofoil

The demands for more efficient air transport require these adverse effects of transonic flight to be reduced. Aerofoils which delay the onset of the transonic drag rise, thus allowing high aerodynamic efficience at higher Mach numbers, have been designed recently. These aerofoils are termed supercritical aerofoils.

The general shape of a conventional aerofoil and of a supercritical aerofoil are shown in Figure 2 [5]. Supercritical aerofoils are characterized by substantially reduced curvature of the middle region and considerable camber near the trailing edge. The reduced curvature eliminates the flow acceleration on the top surface ahead of the shock, resulting in a decrease of the shock strength. As can be seen, the shock is located significantly aft of the midchord position. The re-energization of the boundary layer by mixing, which takes place after it moves through the shock and before it moves through the pressure gradient near the trailing edge, is one of the important factors which allows the flow to remain attached to the surface. Unfortunately, supercritical aerofoils are very sensitive to small changes in Mach number and angle of attack and at off-design conditions separation may occur resulting in poor performance.

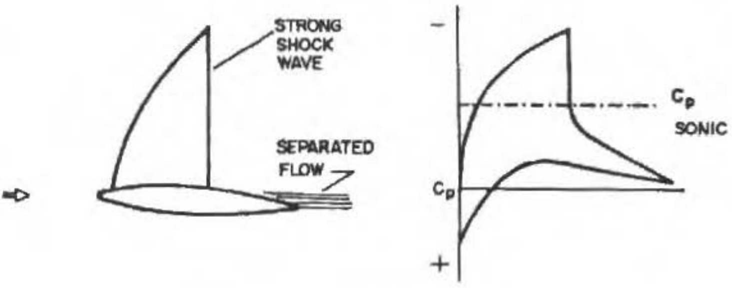

CONVENTIONAL AEROFOIL

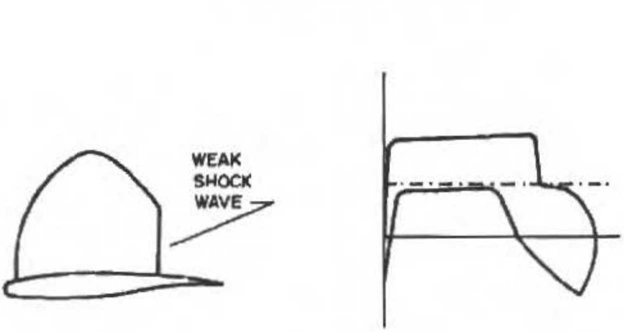

SUPERCRITICAL AEROFOIL

Figure 2. Typical pressure profiles for conventional and supercritical aerofoils

In order to widen the off-design margins of supercritical aerofoil performance, one possibility is to make the surface in the vicinity of the shock porous. Transpiration can then be used to control the shock/boundary layer interaction (SBLI). Active control may be achieved, for example, by applying suction or tangential blowing. Passive control provides a more economic means of controlling the SBLI. A passive control technique consists of placing a porous surface over a plenum chamber in the interaction region. The higher pressure downstream of the shock forces fluid into the cavity and out ahead of the shock.

This secondary flow thickens the boundary layer upstream of the shock generating compression waves in the supersonic region which meet and weaken the nearly normal shock wave terminating the supersonic flow. These effects minimize the overall entropy rise across the shock and hence decrease the wave drag.

Experimental investigations by several authors have shown that passive control can be an effective means of improving the performance of supercritical aerofoils at off-design conditions. SAVU et al [6,7] considered a symmetric aerofoil with a porous surface which extends from near the leading edge to near the trailing edge. They observed that the resulting flow configuration was shock-free and that an increase in the drag rise Mach number was obtained.

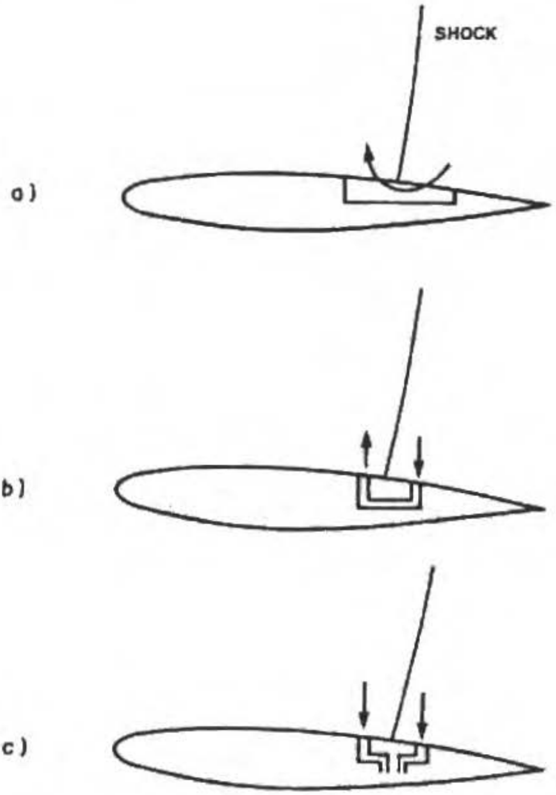

Figure 3. a) Passive control with plenum chamber; b) passive control with double slot; c) active control with double slot

NAGAMATSU et al [8] studied a supercritical aerofoil with a uniformly perforated surface. The porosity extended from the 56% to 81% chord positions, i.e. a porosity of 2.8% of the total surface area. The studies were conducted for Mach numbers varying from 0.75 to 0.90. It was reported that a distributed porosity of 2.8% decreased the drag by 46% compared with the solid aerofoil surface at $M = 0.865$. At Mach numbers less than $M = 0.84$, a decrease in aerofoil drag was not achieved by this method.

RAGHUNATHAN AND MABEY [9] investigated the passive effect on circular arc models with porous surfaces extending from 53% to 93% of the chord length. The porosity was variable from zero to 3.16%. The interesting feature of this study is that the porous surfaces were obtained by drilling holes normal to the surface and inclined to the surface in the forward-facing and backward-facing direction. The results show that the normal hole models present a small reduction in drag whereas the inclined hole models show an appreciable increase in drag.

KROGMANN et al [10] experimentally studied a supercritical aerofoil with a porous surface of 7.5% of the chord length. The drag coefficient was considerably reduced for a high angle of incidence whereas at a low angle of incidence the drag decreased only slightly. In this work, the effects of active suction, and of passive suction and blowing, using a double slot with a cavity beneath the interaction region were also studied.

Since the majority of the works on the passive control technique have been conducted experimentally, it has become increasingly important to develop a theory to explain the main features of this control technique in a rational way. So far, most of the theoretical studies of viscous-inviscid interaction for porous aerofoils have basically used the same approach [11,6,7]. In these works viscous-inviscid interaction is used to compute two-dimensional flows over porous aerofoils. The results suggest that the transpiration leads to a decrease in the drag coefficient and an increase in the lift coefficient.

Recently several researchers [12,13,14,15,16,17] have applied perturbation methods to the problem of the interaction between a normal shock wave and a turbulent boundary layer over a solid flat plate with a fair degree of success. This approach has been particularly useful in identifying the relevant length scales of the problem, and in revealing the primary dependence of the flow variables on the flow parameters. Thus it seems that an analysis of the passive control technique under this theoretical framework would help to further understanding of this problem. The objective of this work is to show in detail how such analysis can be carried out.

Most of the studies which use this theoretical approach divide the flow field into a region of strong interaction and regions of weak interaction upstream and downstream of the shock wave (Figure 4). The region of strong interaction is that in which the Reynolds stresses can be neglected in most of the defect layer. This leads to a three-deck formulation for this region. A blending layer is introduced to ensure that the solutions for the defect layer and for the wall layer can be matched. The two weak interaction regions have a classical two-deck structure (AFZAL [18], SILVA FREIRE [19]). To obtain a smooth solution for the whole flow field we must match the solutions for the various regions in both the x-direction and the y-direction. Thus, it follows that the solution for the defect layer in the strong interaction region will depend strongly on the solution for the defect layer in the upstream weak interaction region. Hence, before one proceeds to the analysis of the interaction problem, it becomes necessary to obtain asymptotic solutions for the undisturbed flow ahead of the shock, that is, for transpired turbulent boundary layers. Unfortunately, the majority of the works on this subject are experimental and, in particular, no solution of this problem obtained through perturbation methods was found by the present author in the literature. In fact, further research revealed that even for the incompressible case no asymptotic solution was available. Moreover, several authors [14,15,17] pointed out that application of a three-deck model to compressible turbulent boundary layer caused some problems in the matching of the defect layer and of the wall layer, which could not be rectified.

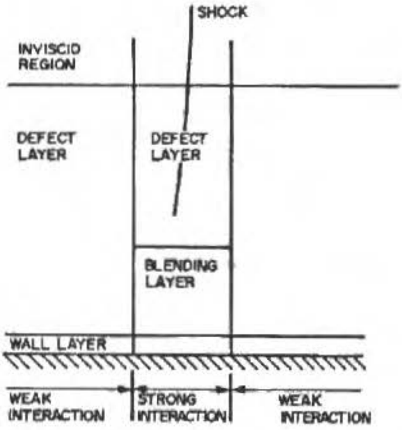

Figure 4. Flow structure for SBLI phenomenon

To tackle the interaction problem we then adopt the following procedure. First we apply the matched asymptotic expansion method to transpired incompressible turbulent boundary layers [20] to derive profiles for the defect and wall layers. Next, a careful study of the application of perturbation techniques to compressible flow is carried out [19] to justify the choice of the profiles for the undisturbed region ahead of the shock (Figure 4). With these results we extend the analysis developed in Refs. [19,20] for transpired incompressible flow to compressible flow [21].

Having obtained expressions for the initial profiles, we extend the theory developed in Refs. [14,17], for the interaction between shock waves and turbulent boundary layers, to our case of interest. The overall procedure is illustrated in Figure 5. A review of the main work on shock interaction is presented in Section 5.

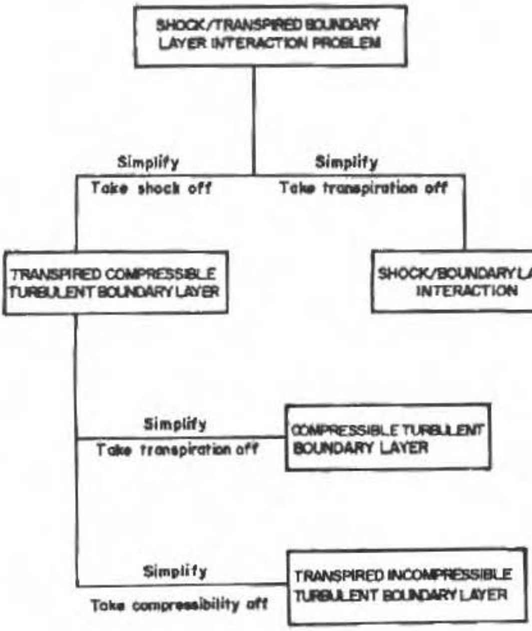

Figure 5. Solution procedure

TRANSPIRED INCOMPRESSIBLE TURBULENT BOUNDARY LAYERS

Turbulent boundary layers with injection or suction of fluid have been the subject of many theoretical and experimental works [22,23,24,25]. Much of these studies have concentrated on the investigation of the law of the wall and of the law of the wake. The theoretical analyses normally use the mixing-length theory of Prandtl together with the assumption that the mixing-length is proportional to the distance of the wall. This procedure leads to equations which have some parameters that need to be determined with the aid of experimental data and that for this reason depend strongly on measured values of the skin friction-coefficient. Unfortunately, these values are normally obtained through the use of some form of the momentum integral equation which is very sensitive to small changes in the flow parameters and so tends to be very inaccurate.

To overcome this difficulty, we have studied this problem in Ref. [20] using perturbation methods. The main outcome of this analysis was the derivation of a skin-friction equation which is much less sensitive to small changes in the injection velocity and in the Reynolds number, so that it gives much more reliable results. The analysis also proposes a new expression for the law of the wake. This expression is used to cross check the results obtained by the skin-friction equation.

The analysis adopts a classical two-deck model for the boundary layer and shows that, as for the solid surface case, the defect layer is scaled by $\delta = O(\varepsilon l)(\varepsilon = u_\tau/U_\infty = \sqrt{\tau/\rho U_\infty^2})$, whereas the wall layer is scaled by $\hat{\delta} = O(\delta\hat{\varepsilon}) = O(\nu/u_\tau)$. The boundary conditions at the wall define the small regular parameter $\bar{\varepsilon} = V_w/U_\infty$.

In solving our problem we find solutions similar to those of SIMPSON [23], STEVENSON [25] and MCQUAID [22]. The solutions are shown to give good results for flows with either injection or suction of fluid.

The analysis which follows deals only with the two innermost layers, the defect layer and the wall layer. A solution is obtained assuming proper asymptotic expansions for these regions, and then using the matched asymptotic expansion method to derive the equations for the various orders of approximation.

The wall layer solution is shown to be given by

$$\hat{u}(x,\hat{y}) = \varepsilon\left(\frac{1}{K}\ln\hat{y} + \hat{A}\right) + \bar{\varepsilon}\left(\frac{1}{4K^2}\ln^2\hat{y} + \hat{C}\ln\hat{y} + \hat{D}\right), \tag{1}$$

where $\hat{y}\,(= Y/\varepsilon\hat{\varepsilon})$ is the stretched wall layer co-ordinate, K is the Von Karman constant and $\hat{A}, \hat{C}$ and $\hat{D}$ are parameter to be determined. The circumflex is used to denote a wall layer variable.

Equation (1) is the classical law of the wall for transpired turbulent boundary layers. A comparison of this equation with the equation derived by other authors is presented in Ref. [20].

The defect layer solution on the other hand is given by

$$u = 1 + \varepsilon\left(\frac{1}{K}\ln y - \frac{\pi}{K}(2 - w(y))\right) + \bar{\varepsilon}\left(B\ln^2 y + C\ln y - \frac{\bar{\pi}}{K}(2 - w(y))\right), \tag{2}$$

where

y - Y/δ
π - Coles' profile parameter
$w(y)$ - Coles' wake functions
$\bar{\pi}$ - profile parameter of the wake component due to the transpiration
B, C - parameters to be determined

Comparison of Equations (1) and (2) in the overlap region requires that

$$B = \frac{1}{4K^2} \,, \tag{3}$$

$$C = \frac{1}{2K^2} \ln \frac{\delta}{\tilde{\delta}} + \hat{C} \,, \tag{4}$$

and

$$1 = \varepsilon \left(\frac{1}{K} \ln \frac{\delta}{\tilde{\delta}} + \hat{A} + \frac{2\pi}{K} \right) + \tilde{\varepsilon} \left(\frac{1}{4K^2} \ln^2 \frac{\delta}{\tilde{\delta}} + \hat{C} \ln \frac{\delta}{\tilde{\delta}} + \hat{D} + \frac{2\tilde{\pi}}{K} \right) . \tag{5}$$

Equation (5) is the skin-friction equation for transpired turbulent boundary layer layers. The novelty of Equations (2) and (5) is the introduction of a profile parameter, $\tilde{\pi}$, distinct from π.

Parameter $\hat{A}, \hat{C}, \hat{D}$ and $\tilde{\pi}$ are determined through a careful analysis of the data of ANDERSEN [26] for different flowing rates (Table 1). This data set is recommended by SQUIRE [27] as a basic test case for flows with zero pressure gradient and constant injection rates. Thus we find that A is given by

$$A = 5 - 512\, \tilde{\varepsilon} \,, \tag{6}$$

whereas $\tilde{\pi}$ is given by

$$\tilde{\pi} = -\, 1.95 \ln \tilde{\varepsilon} - 3.1 \;. \tag{7}$$

Table 1. Experimental flow conditions

FI	$\tilde{\varepsilon}$	U_∞ $[ft/s]$
1	0.0	31.0
2	0.00102	31.0
3	0.00200	31.0
4	0.00375	31.0
5	0.00800	31.0

Values of the skin-function predicted by Equation (5) are compared with experimental conditions in Figure 6 and in Table 2. To check Equation (5) for sucked flow we have used the data of SIMPSON [23] and of FAVRE et al [28]. As can be seen the agreement is quite good. The predicted velocity profiles are shown in Figures 7 to 8.

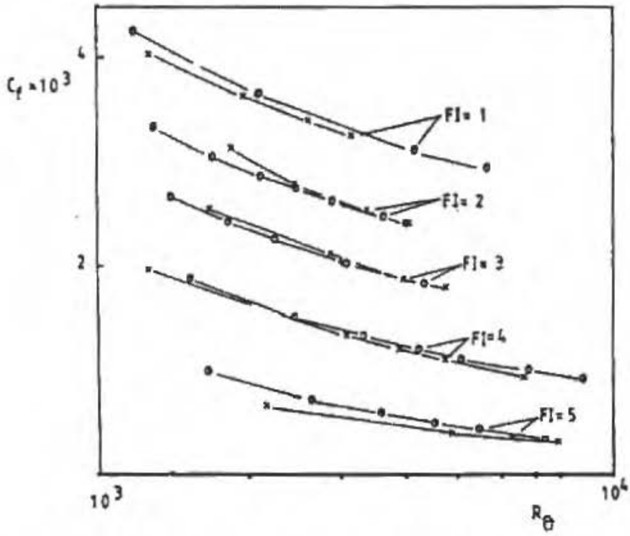

Figure 6. Comparison of results for various injection rates and R_θ. °, Equation (5); x, Andersen's results

Table 2. Suction results

Investigator	FS	$\bar{\varepsilon}$	ε Theor.	ε Exp.	R_δ
Simpson	1	-0.00115	0.0474	0.0469	31010
	2	-0.00117	0.0484	0.0482	24070
	3	-0.00231	0.0554	0.0558	22620
	4	-0.00242	0.0576	0.0558	12840
	5	-0.00462	0.0770	0.0663	1526
Favre	6	-0.0119	0.0493	0.0469	18570
	7	-0.00252	0.0573	0.0534	17730
	8	-0.00516	0.0730	0.0663	15960

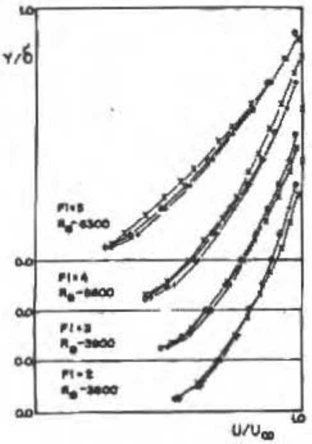

Figura 7. Velocity profile correlation for injection data. x, experimental data; °, Equation (2), +, previous formulation

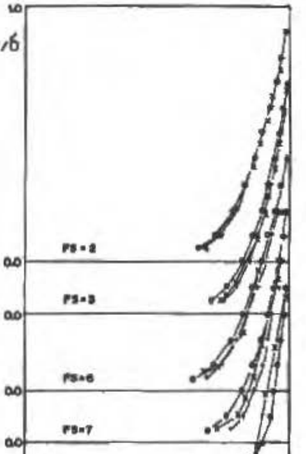

Figura 8. Velocity profile correlation for suction data. x, experimental data; °, Equation (2), +, previous formulation

THE TWO-DECK MODEL FOR COMPRESSIBLE TURBULENT BOUNDARY LAYERS

Several authors [29,30] developed in recent years asymptotic theories for incompressible turbulent boundary layers using the matched asymptotic expansion method, together with asymptotic hypotheses describing the order of magnitude of the fluctuations of the several flow parameters.

AFZAL [18] extended the theories developed for incompressible flow to compressible flow. He worked with an underdetermined system of equations and showed that, as for the incompressible case, two layers are required. Unfortunately, Afzal's solution was quickly dismissed since various authors [14,15,17] pointed out that Afzal had worked with an underdetermined system of equations and had not showed that the wall and the defect solutions did, in fact, match. The difficulty stemmed from the fact that the density varied by order unity from wall to free stream values, which could not be accounted for by Afzal's solution. It is important to note that up to then no systematic study about the domains of validity of the solutions had been carried out.

To study the domains of validity of the solutions, the present author applied the intermediate variable technique [19] to the problem of a compressible turbulent boundary layer. The theory's underlying idea is to characterize the solutions by their domains of vality so that overlapping is promptly determined.

Asymptotic Hypotheses and Domains of Validity. The velocity fluctuations are assumed, according to Kistler's data [31], to be of the order of the non-dimensional friction velocity, ε, i.e.,

$$u' = 0\left[\frac{u_\tau}{U_\infty}\right] = 0\left[\frac{1}{U_\infty}\sqrt{\frac{\overline{\tau}_w}{\rho_w}}\right] = 0(\varepsilon) \ . \tag{8}$$

Further measurements of KISTLER & CHEN [32] and of MORKOVIN [33] show that the density and temperature fluctuations have the same order of magnitude, ε, and that the root-mean-square value of p' is also of order ε.

The domains of validity are studied using the intermediate variable technique [34,35,36]. This method uses the concept of intermediate limit to study the importance of the various terms of the governing equations in the distinct regions of the flow. Thus a careful analysis of the problem presents approximate solutions for the various flow regions which are associated to domains of validity. The intermediate equations [36] are shown to coincide with the usual approximate equations for the logarithmic and laminar regions whereas the principal equations coincide with the boundary layer equations. Thus, for the defect layer the governing equations are:

· x-momentum:

$$\bar{\rho}\tilde{u}\frac{\partial\tilde{u}}{\partial x} + \bar{\rho}\tilde{v}\frac{\partial\tilde{u}}{\partial y} = -\frac{\partial\bar{p}}{\partial x} + \frac{\partial[\bar{\rho}\,\overline{\tau_{uv}}]}{\partial y} \tag{9}$$

· energy:

$$\bar{\rho}\tilde{u}\frac{\partial\tilde{t}}{\partial x} + \bar{\rho}\tilde{v}\frac{\partial\tilde{t}}{\partial y} - D\left[\tilde{u}\frac{\partial\bar{p}}{\partial x} + \tilde{v}\frac{\partial\bar{p}}{\partial y}\right] = \frac{\partial\,[\bar{\rho}\,\overline{\tau_{vt}}\,]}{\partial y} + D\,\frac{\partial\,[\overline{\tau_{vp}}\,]}{\partial y}\ . \tag{10}$$

In the above equations the bars denote conventional time averaging, the tildes denote mass-weighted averaging and $D = (\gamma - 1)\,M_\infty^2$. Correlations of the type $\overline{u'v'}$ are denoted by τ_{uv}.

The analysis also shows that according to Lagerstrom and Casten's definition of formal domain of validity of a solution, the domain of validity of Equations (9) and (10) is given by:

$$D_0 = \left\{\eta / ord\ \eta > ord\ \hat{\varepsilon}\right\} \tag{11}$$

where η is an arbitrary function of ε.

For the wall layer we find that the approximate governing equations are:

· x-momentum:

$$\frac{\partial\,[\bar{\mu}\,\frac{\partial\tilde{u}}{\partial y}\,]}{\partial y} + \frac{\partial\,[\bar{\rho}\,\overline{\tau_{uv}}\,]}{\partial y} = 0 \tag{12}$$

· energy:

$$\frac{1}{\sigma}\,\frac{\partial\,[\bar{\mu}\,\frac{\partial\tilde{t}}{\partial y}\,]}{\partial y} + \frac{\partial\,[\bar{\rho}\,\overline{\tau_{vt}}\,]}{\partial y} + D\,\frac{\partial\,[\overline{\tau_{vp}}\,]}{\partial y} = 0\ , \tag{13}$$

where σ is the Prandtl number.

The domain of validity of the above equations is, in its turn, given by

$$D_i = \{\eta / ord\ \eta < ord\ \varepsilon^2\} \tag{14}$$

We are now in a position to evaluate the overlap domain of the defect and wall layers. In fact, application of Kaplun's matching principle [34] to sets (11) and (14) yields that the overlap region is given by

$$D_0 \cap D_i = \{\eta / ord\ \hat{\varepsilon} < ord\ \eta < ord\ \varepsilon^2\} \tag{15}$$

This result does suggest that, if a two-deck model is assumed to a compressible turbulent boundary layer, then the defect and the wall layer solutions do have a common region of validity.

Asymptotic Analysis. In Ref. [19] it is also presented an analysis where we show how asymptotic solutions for the defect and wall layers can be proposed which do match in an overlap domain. The analysis uses the matched asymptotic expansion method and focus its attention on the defect and wall layers.

An important finding of this analysis is the ocurrence of second-order bilogarithmic terms in the velocity profiles. In fact, it is demonstrated that the first-order terms are logarithmic terms and that this condition is enough to ensure the appearance of second-order bilogarithmic terms. Thus a similar conclusion is reached for the temperature profiles.

The second order bilogarithmic terms play an important role in the performance of the matching since they change their order of magnitude in the overlap region, so increasing the number of parameters avaliable for the matching operation. In previous analyses the matching could not be carried out because the number of available parameters was smaller than the number of equations. This caused difficulties with the matching of the density profiles which could not be overcome.

TRANSPIRED COMPRESSIBLE TURBULENT BOUNDARY LAYERS

The majority of the works published on transpired compressible turbulent boundary layers is the result of research undertaken by SQUIRE and his students at Cambridge University [37,38,39,40,41]. These results cover the Mach number range 1.8 to 3.6 at various injection rates. As for the incompressible case, the analyses concentrate on deriving expressions for the law of the wall and for the law of the wake. Unfortunately, a definitive check on those expressions is not possible since values of the skin-friction are evaluated using the momentum-integral equation which is very inaccurate.

Aiming to extend the solution developed in Ref. [20] for incompressible flow to compressible flow, the present author [21] applied the concept of generalized velocity (VAN DRIEST [42]) to expressions (1) and (2). For a boundary layer with a finite wake, MAISE & MCDONALD [43] showed that

$$u^{*}_{\infty} - u^{*} = u_{\tau}\left[-\frac{1}{K}\ln\frac{y}{\delta} + \frac{\pi}{K}(2 - w(y/\delta))\right] , \tag{16}$$

where

$$u^{*} = \frac{U_{\infty}}{\xi}\,arcsin\,\left[\frac{\xi U}{U_{\infty}}\right] ,$$

$$\xi^{2} = (\gamma - 1)M^{2}/(2 + (\gamma - 1)M^{2}) ,$$

and $w =$ Coles' wake function.

Application of Van Driest's transformation directly to the expression derived in Ref. [20] is then made in Ref. [21] so that a skin-friction equation can be derived for transpired compressible turbulent boundary layers.

This procedure gives a defect velocity profile which reads

$$\begin{aligned} u^{*}_{\infty} - u^{*} = {} & u_{\tau}\left[-\frac{1}{K}\ln\frac{y}{\delta} + \frac{\pi}{K}(2 - w(y/\delta))\right] + v_{w0}\left[-\frac{1}{4K^{2}}\ln^{2}\frac{y}{\delta} - \right. \\ & \left. - \left[\frac{1}{2K^{2}}\ln\frac{\delta}{\hat{\delta}} + \frac{A}{2K}\right]\ln\frac{y}{\delta} + \frac{\tilde{\pi}}{K}(2 - w(y/\delta)\right] . \end{aligned} \tag{17}$$

Parameters A, π and $\tilde{\pi}$ are assumed to vary as defined in Section 2, Equations (6) and (7). Parameter v_{w} in Equation (2) is replaced by v_{w0} in Equation (17) due to the flow compressibility. In a compressible flow the normal velocity varies to order unity and hence a reference velocity needs to be defined.

In Ref. [21], it is shown that

$$v_{w0} = \text{characteristic normal velocity in the overlap region} = v(0.1) . \tag{18}$$

Matching arguments applied to the defect and wall layer solutions yield the skin-friction equation which reads

$$u_{e} = \frac{u_{\tau}}{K}\ln\frac{\delta}{\hat{\delta}} + \frac{v_{w0}}{4K^{2}}\ln^{2}\frac{\delta}{\hat{\delta}} + u_{\tau}A + \frac{v_{w0}}{2K}A\ln\frac{\delta}{\hat{\delta}} + u_{\tau}\frac{2\pi}{K} + \left[\frac{A^{2}}{4} + \frac{2\tilde{\pi}}{K}\right]v_{w0} , \tag{19}$$

where

$$u_e = U_\infty (\arcsin \xi)/\xi \ .$$

The above equation determines C_f for given values of M, U_∞, δ and v_{w0}. Predicted values of C_f are compared with the experimental data of SQUIRE [39] in Figures 9 to 11. The agreement is reasonable despite clear indication that the strength of the wake function due to the transpiration does vary with Mach number. The predicted velocity profiles are shown in Figures 12 to 14.

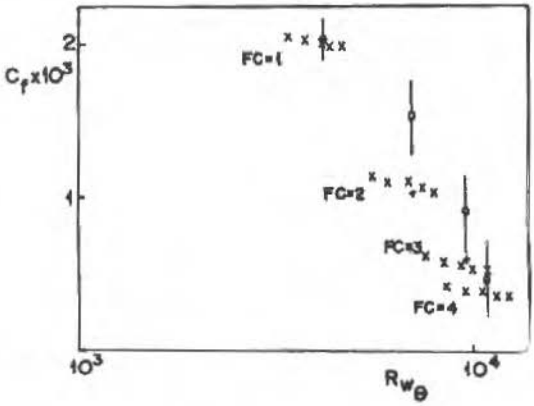

Figure 9. Predictions of C_f for $M = 1.8$. x, Equation (19); °, Squire's results

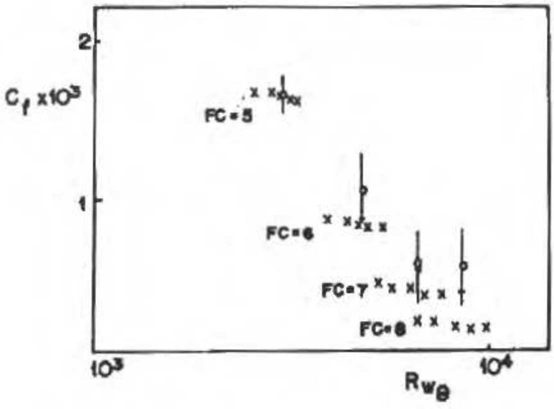

Figure 10. Predictions of C_f for $M = 2.4$. x, Equation (19); °, Squire's results

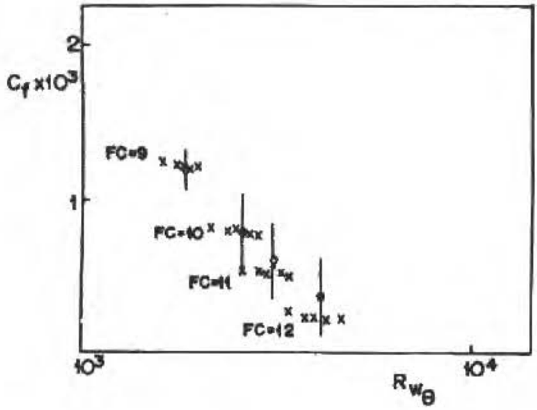

Figure 11. Predictions of C_f for $M = 3.6$. x, Equation (19); °, Squire's results

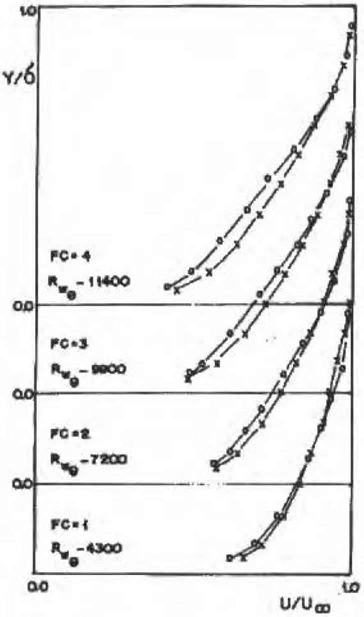

Figure 12. Velocity profiles for $M = 1.8$. x, Equation (17); °, experimental results

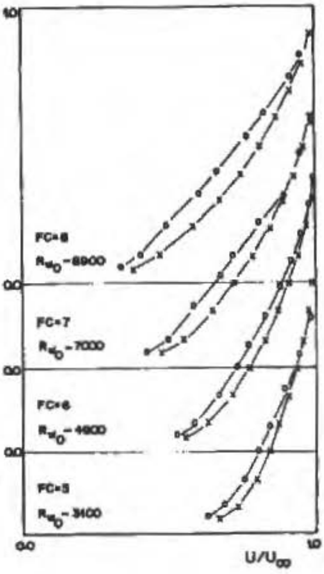

Figure 13. Velocity profiles for $M = 2.4$. x, Equation (17); °, experimental results

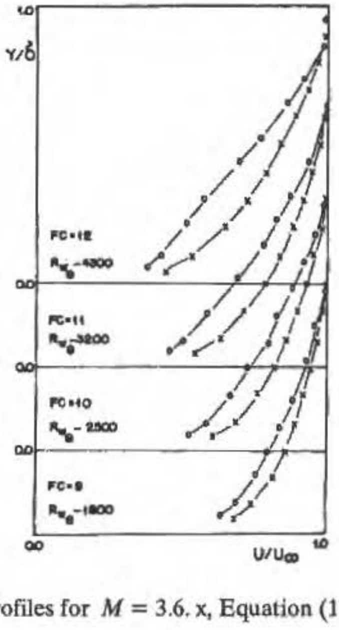

Figure 14. Velocity profiles for $M = 3.6$. x, Equation (17); °, experimental results

INTERACTION BETWEEN SHOCK WAVES AND TRANSPIRED TURBULENT BOUNDARY LAYERS

In the present section, we shown how the problem of the interaction of a normal shock wave and a turbulent boundary layer over a porous surface with a cavity beneath is solved (Ref. [44]). The study employs asymptotic techniques and is basically an extension of the works of MESSITER [17] and of LIOU & ADAMSON [14] for the permeable surface case. Thus, Ref. [44] deals with flows at high transonic speeds.

Interaction between Normal Shock Waves and Turbulent Boundary Layers. Here we briefly review the various theories developed in the past for the interaction problem when the surface is solid. For comments on experimental works the reader is referred to the reviews of GREEN [3], STANEWSKY [45] and HANKEY and HOLDEN [46].

The first serious attempt at developing a rational theory for the interaction problem was made by Lighthill in 1953. In his paper, Lighthill identified the physical mechanisms of the interaction, recognizing that in most of the boundary layer the stream-wise pressure gradient is large compared to the shear stress so that the local interaction can be described by the inviscid flow equations. The inviscid rotational flow model for strong viscid-inviscid interactions proposed by Lighthill became the basis for most of the theoretical works on this subject. In fact, years after, these ideas led to the development of the triple deck-theory by the late Keith Stewartson. Most of the details in Lighthill's theory are generally correct for laminar flow. However, for turbulent flow some modifications need to be made since the original procedure is inconsistent with the now well known [18,29,30] structure of the turbulent boundary layer near the wall.

In recent years several authors [1,14,15,17] have perfected Lighthill's theory for turbulent flow using carefully chosen initial profiles. These theories have usually dealt with normal shock waves on flat, solid, surface because of the important applications of this case. The two basic parameters of the problem are the free stream Mach number, M_∞, and Reynolds number, R_∞. The limit as R tends to infinity can also be represented by the limit as the non-dimensional friction velocity, $\varepsilon = u_\tau/U_\infty$, tends to zero since $\varepsilon = 0(\ln R_\infty)^{-1}$ [18,29]. Thus solutions obtained with the use of asymptotic techniques are characterized by the double limit $M \to 1$ and $\varepsilon \to 0$. MELNIK [48] has classified the structure of the flow field according to the order of magnitude of a parameter χ_τ defined by

$$\chi_\tau = \frac{M_\infty^2 - 1}{\varepsilon} .$$

Four different cases to be studied occur depending on the relative rates at which parameters $(M_\infty^2 - 1)$ and ε approach their respective limits. They are:

a) very weak shock wave, $\chi_\tau \to 0$

b) weak shock wave, $\chi_\tau = 0(1)$

c) moderate shock wave, $\chi_\tau \to \infty$

d) strong shock wave, $\chi_\tau \to \infty$. $(M_\infty \text{ large} \neq 1)$

Parameter χ_τ expresses the ratio between the velocity change across the shock wave and the velocity change across the boundary layer; in other words, it accounts for how deep the shock penetrates the boundary layer. Cases a through *d* are illustrated in Figure 15 which is taken from reference [48].

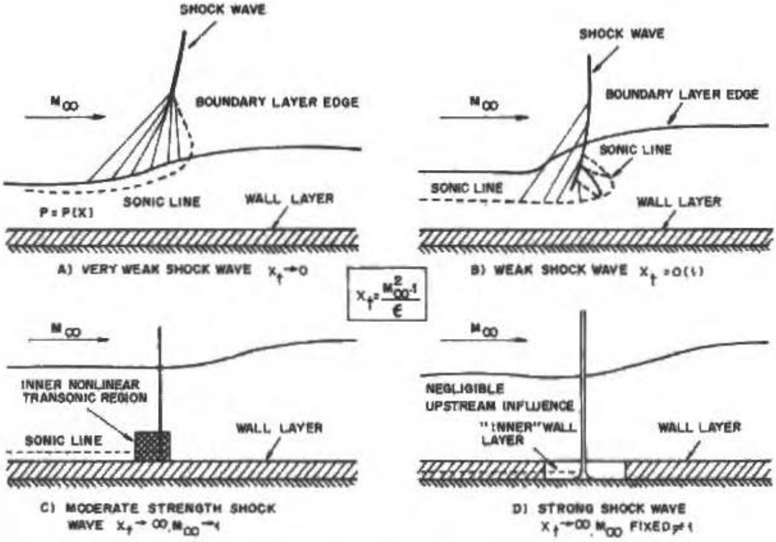

Figure 15. Flow configuration according to values of parameter χ_τ

The very weak shock limit was studied by ADAMSON and FEO [12]. For this case the sonic line is located close to the edge of the boundary layer and compression waves generated by the thickening of the boundary layer weaken the shock so that it remains outside the boundary layer. The stream-wise pressure gradient is shown to spread over a distance large compared to the boundary layer thickness whereas the normal pressure gradient is shown to be negligible in the inner regions. The flow in the outer part of the boundary layer is governed by inviscid equations.

The weak shock limit was studied by MELNIK and GROSSMAN [38]. The main feature of this case is that the velocity change across the shock and the velocity change across the boundary layer have the same order of magnitude and consequently the sonic line is located somewhere in the main part of the boundary layer. The flow is considered inviscid in the outer region. The flow region was divided into regions of strong and weak interaction and expressions were obtained for the pressure and skin-friction profiles. The novelty of this study was the use of three decks to describe the structure of the boundary layer in the strong interaction region as opposed to the commonly used two-deck structure.

MESSITER [17] and LIOU & ADAMSON [14] analysed the moderate strength shock limit. In this case, the shock wave penetrates deep into the boundary layer but remains outside the wall layer. The sonic line is located close to the wall and hence the upstream influence is negligible. The flow downstream of the shock is described by a linear perturbation to the undisturbed flow upstream the shock.

The fourth case, the strong shock wave, is not of interest in the present study and since no rational study of this problem has been performed no further comments about it will be made here.

The Flow Regions. As mentioned before, Mach number in our case of interest is such that the normal shock wave penetrates deep into the boundary layer. Hence, the structure of the flow is that depicted in Figure 16. This structure is similar to that introduced by MESSITER and by LIOU & ADAMSON in [14] and [17]. Indeed, it is shown in Refs. [20] and [21] that the influence of the blown or sucked flow is such that the various flow regions are preserved.

The assumed three-deck structure of the undisturbed region ahead of the shock is justified in Sections 2 to 4. The disturbed region requires the inclusion of a fourth layer, the Reynolds layer, since now for most of the defect layer the Reynolds stress is negligible when compared to the pressure gradient provoked by the shock wave. Thus, the defect layer in the interaction region is governed by inviscid equations and momentum is transferred from the wall layer to the defect layer through the Reynolds layer.

The order of magnitude of the various flow regions are shown in Figure 16. Note that the solutions are expressed in terms of four small parameters; two parameters related to the external flow and, two parameters related to the blowing and the suction of fluid, v_{wu} and v_{wd}. The subscripts w, u and d refer to conditions at the wall, upstream of the shock and downstream of the shock respectively.

$\varepsilon = \dfrac{U_\infty}{a^*} - 1$, a^* = critical sound speed in the external flow just ahead of the shock

$u_\tau = \dfrac{1}{a^*}\sqrt{\dfrac{\tau_w}{\rho_w}}$, τ_w = laminar stress at the wall

ρ_w = density at the wall

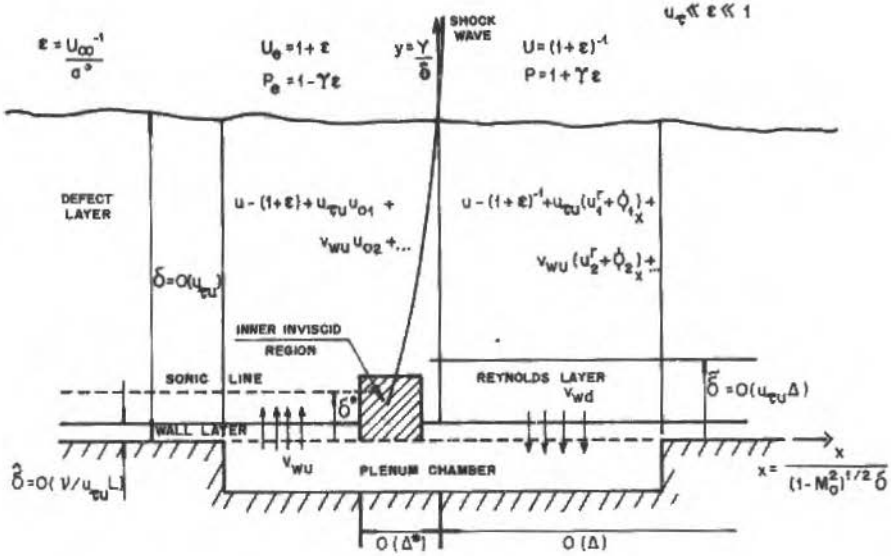

Figure 16. The flow regions

In solving our problem, solutions for adjacent layers must be matched so that a smooth solution is obtained. Finally, it can be shown [1] that in Figure 16, $\Delta >> \Delta^*$ and $\delta >> \delta^*$, which implies that the inviscid flow region at the shock foot is exponentially small when compared to the interaction region scaled by Δ and δ.

The Pressure Distribution in the Interaction Region. Since in the defect layer the turbulence terms are very small when compared with the inertia and the pressure terms, it follows that the motion of the flow is governed by the gas dynamic equation, the momentum equation, the vorticity equation and the state equation [17].

The gas dynamic equation and the vorticity equation imply that the length scales in the interaction region are $\Delta = 0\,(b_0\,\delta)$, $b_0^2 = 1 - M_0^2$ (M_0 = Mach number in the external flow behind the shock wave), and δ. Hence, the stretched co-ordinates for the defect layer are

$$x = X/(b_0\,\delta) \qquad , \quad y = Y/\delta \tag{20-21}$$

where

$$b_0 = (\gamma + 1)^{1/2}\,\varepsilon^{1/2}\,(1 - \frac{1}{4}(2\gamma + 1)\,\varepsilon + \dots)\ . \tag{22}$$

The boundary conditions are determined by the normal shock wave jump conditions and by the wall. The velocity profiles for this region, separated into a rotational and an irrotational part, are written as

$$u_d = (1 + \varepsilon)^{-1} + u_{\tau u}\,u_1^r(x,y,\varepsilon) + u_{\tau u}\,\varphi_{1_x}(x,y,\varepsilon) + v_{wu}\,u_2^r(x,y,\varepsilon) +$$

$$+ v_{wu}\,\varphi_{2_x}(x,y,\varepsilon) \tag{23}$$

$$v_d = b_0\left[u_{\tau u}\,\varphi_{1_y}(x,y,\varepsilon) + v_{wu}\,\varphi_{2_y}(x,y,\varepsilon)\right] + v_{w0d}\,v_1(x) \tag{24}$$

The equation of state, together with the fact that along a streamline the entropy is constant, gives [17]

$$p/p_e = 1 - \gamma\,(u - u_u) - \gamma^2\,(u_u - 1)\,(u - u_u) \tag{25}$$

Substitution of Equations (23) and (24) (Ref. [44]) into the governing equations gives, for the irrotational part of u_d,

$$u_i^r = (1 + 2\gamma\,\varepsilon + \gamma\,(2\gamma - 1)\,\varepsilon^2 + \dots)\,u_{oi}(y)\ , \qquad i = 1, 2 \tag{26a-b}$$

where

$$u_{01} = \frac{1}{K}\ln y - \frac{\pi}{K}(2 - w(y))\ ,$$

and

$$u_{02} = \frac{1}{4K^2}\ln^2 y + \left[\frac{1}{2K^2}\ln\frac{\delta}{\tilde{\delta}} + \frac{A_u}{K}\right]\ln y - \frac{\pi_u}{K}(2 - w(y))\ .$$

For the rotational part of u_d, we have

$$\varphi_{i_{xx}} + \varphi_{i_{yy}} = 0 \ . \tag{27}$$

The solution of the above equation subject to appropriate boundary conditions [44] gives

$$\varphi_{i_x}(x,y) = -\frac{4}{\pi}\left[1 + (\gamma - 1)\,\varepsilon + [\,\gamma\,[\,\gamma - \frac{1}{2}]\, + 3]\ \varepsilon^2\right]\int_0^\infty \frac{x\,u_{oi}(y)}{x^2 + (y - \eta)^2}\,d\eta. \tag{28}$$

Substitution of expression (23) with results (26) and (28) into Equation (25) gives the pressure distribution across the boundary layer. Hence, the pressure at the wall, given by the limiting form of the pressure expression as $y \to 0$, is

$$\frac{p_w(x)}{p_e} = 1 + \gamma\left[2\varepsilon + (2\gamma - 1)\,\varepsilon^2\right] - \gamma\left[1 + \gamma\varepsilon + \varepsilon^2\,[\,(\gamma - 1)^2 + \frac{7\gamma - 7}{2}]\right]\cdot$$

$$\cdot\left[u_{\tau u}\,\varphi_{1_x}(x,0) + v_{wu}\,\varphi_{2_x}(x,0)\right] \ , \tag{29}$$

with

$$p_e = 1 - \gamma\varepsilon + \frac{\gamma\,\varepsilon^2}{2} \ .$$

The Skin-Friction Equation. The evaluation of the skin-friction requires the study of the two inner layers. The Reynold layer and the wall layer. It is clear from the defect layer solution that solutions for the inner layers must depend on $u_{\tau u}$ and v_{wu}. Moreover, in these layers the shear stress terms are important so that we must expect the effects of the suction to be strongly felt near the wall. Consequently, solutions for these layers must also depend on v_{wd}.

a) Reynolds Layer

The Reynolds layer is, as shown in Ref. [14], governed by standard turbulent boundary layer equations. This result follows from the fact that in this region the characteristic length in y-direction, $\delta = 0(u_\tau\,\Delta)$, is small compared with the characteristic length in x-direction.

To find a solution for the governing equations we adopt a classical clossure model, the mixing-length theory of Prandtl, together with the hypothesis that the mixing length is proportional to the distance of the wall. Thus, substitution of an appropriate [44] set of asymptotic expansions into the equations gives the several order approximate equations. Unfortunately, the resulting equations and solutions are very complex and hence are omitted here for the sake of simplicity. Of course, the Reynolds layer solution as $\tilde{y} \to \infty$ matches the defect layer solution as $y \rightarrow 0$. Here, the tilde is used to denote a Reynolds layer quantity.

b) Wall Layer

Since the two previously introduced layers cannot satisfy the no-slip condition it becomes necessary to consider a new layer adjacent to the wall to do so. Thus, viscous effects in this layer must be such that the fluid is brought to rest at the wall. From these considerations, we get

$$\hat{\delta} = \delta/(u_{\tau u} R_w) \ ,$$

so that the stretched co-ordinate for this region is

$$\hat{y} = y/(u_{\tau u} R_w) \ .$$

The Reynolds layer solution suggests that

$$\hat{u}\,(x,\hat{y}) = u_{\tau d}\,(x)\,\hat{u}_{01}\,(\hat{y}) + v_{wu}\,\hat{u}_{02}\,(\hat{y}) + v_{wd}\,u_{03}\,(\hat{y}) \ , \tag{30}$$

where, in general, $u_{\tau d}$ is a function of $x, \varepsilon, u_{\tau u}, v_{wu}, v_{wd}, \delta, \tilde{\delta}$, and $\hat{\delta}$; $\hat{u}_{01}$, represents a logarithmic function and $\hat{u}_{02}$ and $\hat{u}_{03}$ represent bilogarithmic functions. The underlying idea is to separate $\hat{u}$ into two parts: one to account for the shock and upstream injection, and another to account for the downstream suction. Now, if adequate functions are chosen to represent $u_{\tau d}\,(x), \hat{u}_{01}\,(y), \hat{u}_{02}\,(y)$ and $\hat{u}_{03}\,(y)$, the matching conditions give [44]

$$u_{\tau u}\,(x) = u_{\tau u}\left[1 + a_1\varepsilon + a_2\varepsilon^2 + u_{\tau u}u_1\,(x) + \varepsilon u_{\tau u}\frac{1}{K}\ln\frac{\delta}{\delta}\,u_{1_l}\,(x) + \varepsilon u_{\tau u}u_{11}\,(x)\right] +$$

$$+ \left[v_{wu}u_2\,(x) + v_{wu}\,\varepsilon\ln^2\frac{\delta}{\delta}\,u_{2_l}\,(x) + v_{wu}\,\varepsilon\ln\frac{\delta}{\delta}\,u_{2_m}\,(x) + v_{wu}\,\varepsilon\,u_{22}\,(x)\right]$$

where a_1, a_2 and the functions $u_1\,(x), u_{1_l}\,(x), u_{11}\,(x), u_2\,(x), u_{2_l}\,(x), u_{2_m}\,(x)$, and $u_{22}\,(x)$ are defined in Ref. [44].

The above equation gives the skin-friction in the interaction region. This expression will be compared with experimental results in the next section.

RESULTS

To find a solution for our problem we need to couple both the external flow solution and the solution for the flow inside the plenum chamber. This is done through the boundary condition at the wall which may be very complex if one is dealing with fluid which is blown or sucked through orifices or slots. Here, to simplify the calculations we assume that the velocity normal to the surface is essentially homogeneous, i.e., that the specified mathematical condition at the surface, $v_w(x)$, reproduces well the physical conditions. Thus if the velocity of the flow through the plate's surface is assumed to be directly proportional to the pressure difference between the external and the internal regions, we can write

$$v_w(x) = \sigma (p_h - p_w) \tag{31}$$

where

p_w = external pressure,

p_h = internal pressure,

σ = plate factor.

Since the net mass flow rate over the porous region is zero, that is,

$$\int_L \rho_w v_w \, dx = 0 \quad , \quad L = \text{length of porous bed} \; , \tag{32}$$

it follows that, for a surface of constant porosity, substitution of Equation (32) into Equation (31) gives

$$p_h = \frac{\int_L \rho_w p_w(x) \, dx}{\int_L \rho_w \, dx} \; . \tag{33}$$

The wall velocity is then determined by Equations (31) and (33).

Before comparing our theoretical results with the data obtained for the interaction with flow through a porous surface, let us first consider the solid surface case. unfortunately, even for this case, the performing of experiments is a very difficult task. In fact, several practical problems such as the control of the position of the shock, are very difficult to overcome which make the planning and execution of such experiments a rather complex job. As a result only few works are available in the literature which cover our Mach number range of interest. Furthermore our theory corresponds to the case of two-dimensional, non-separated flow, and hence we need to be sure that any eventually considered experimental data set reproduces well those two conditions.

A review of the literature shows that the most adequate results to test the theory are those of GADD [49] and of SAWYER and LONG [50]. Unfortunately, a careful examination reveals that even these results do not posses the flow conditions desired here [44]. Despite that, Sawyer and Long's experiment is, to the present author's knowledge, the most detailed investigation of this phenomenon for the Mach number range 1.2 to 1.4. Because of that, we have compared our theory with the results given in Ref. [50]. This is done in Figures 17 to 20. The flow conditions are shown in Table 3.

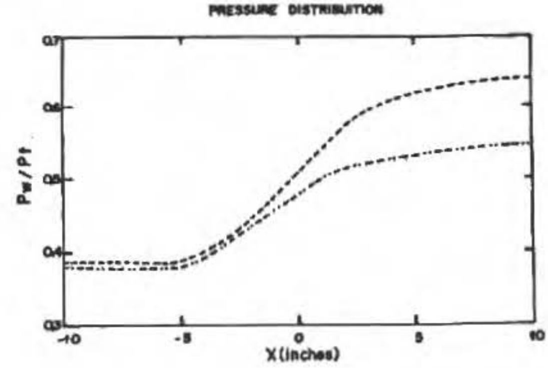

Figure 17. Results for solid plate, $M = 1.27$. — · · —, experiment; —, theory

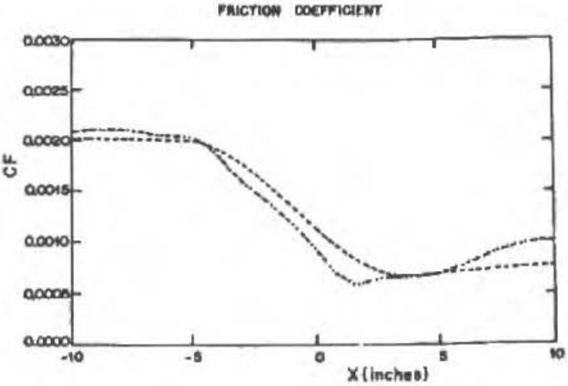

Figure 18. Results for solid plate, $M = 1.27$. — · · —, experiment; —, theory

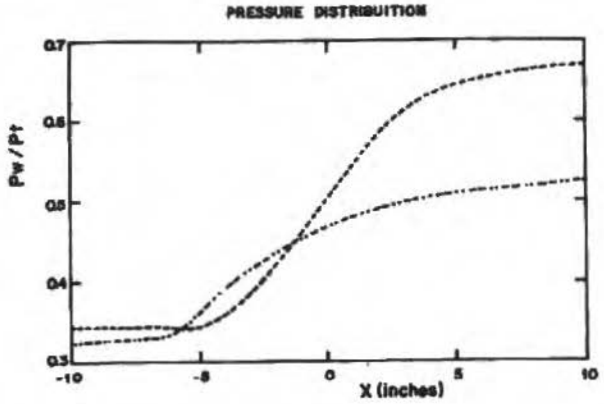

Figure 19. Results for solid plate, $M = 1.37$. — · · —, experiment; —, theory

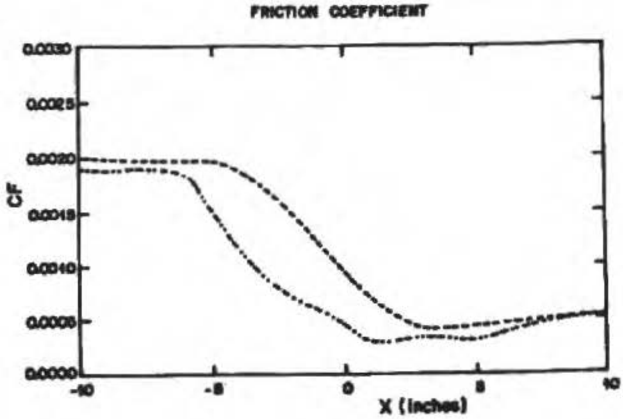

Figure 20. Results for solid plate, $M = 1.37$. — · · —, experiment; —, theory

Table 3. Experimental flow conditions

Conditions	M	ϵ	R/foot	δ_0 ($x = -20$")
a	1.27	0.214	1.12x10	1.55"
b	1.37	0.292	1.12x10	1.43"

No experimental data set was found for the porous surface case which satisfied the conditions assumed to hold in this work. Therefore, to study the effects that a bleed system like the one studied here would have on the properties of a shock wave/boundary layer interaction, we just replaced part of Sawyer and Long's surface by a porous plate with a chamber beneath. The possible cases of interest are illustrated by short ($\approx 6\delta$) and long surfaces ($\approx 24\delta$) with porosities that yield weak ($\sigma = 0.005$) and moderate ($\sigma = 0.02$) injection rates. The results are shown in Figures 21 to 26.

As can be seen, the theoretical results show the general expected trend. Thus a significant increase in C_f downstream of the shock is obtained for moderate injection and suction rates, which suggests that the control technique under present study can be used as a means of preventing separation.

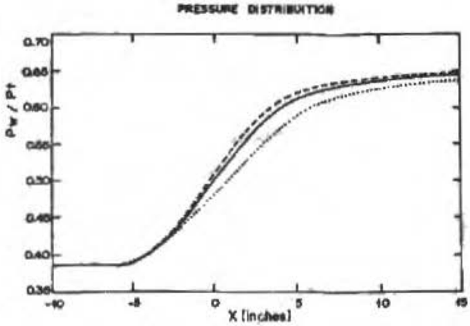

Figure 21. Results for a long stretch of porous surface, $M = 1.27$. ---, $\sigma = 0.0$, —, $\sigma = 0.005$, ..., $\sigma = 0.02$

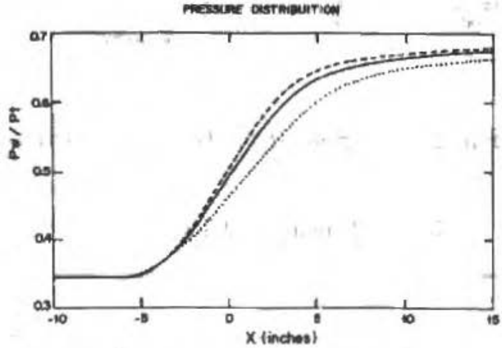

Figure 22. Results for a long stretch of porous surface, $M = 1.37$. ---, $\sigma = 0.0$, —, $\sigma = 0.005$, ..., $\sigma = 0.02$

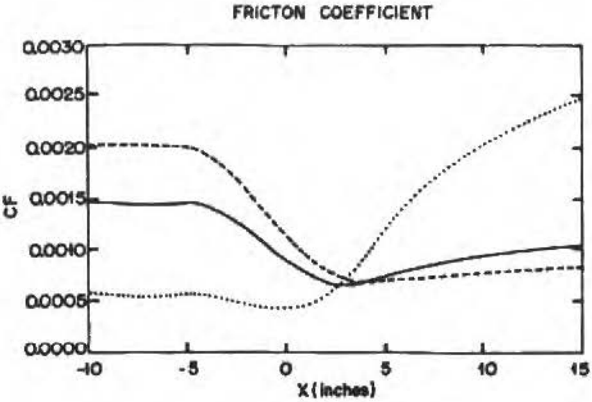

Figure 23. Results for a long stretch of porous surface, $M = 1.27$. ---, $\sigma = 0.0$, — , $\sigma = 0.005$, ... , $\sigma = 0.02$

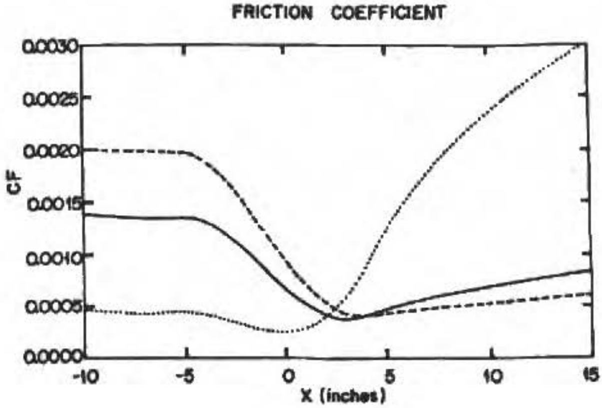

Figure 24. Results for a long stretch of porous surface, $M = 1.37$. ---, $\sigma = 0.0$, — , $\sigma = 0.005$, ... , $\sigma = 0.02$

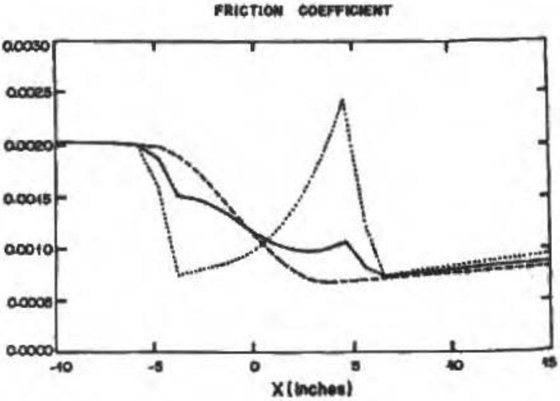

Figure 25. Results for a short stretch of porous surface, $M = 1.27$. ---, $\sigma = 0.0$, — , $\sigma = 0.005$, ... , $\sigma = 0.02$

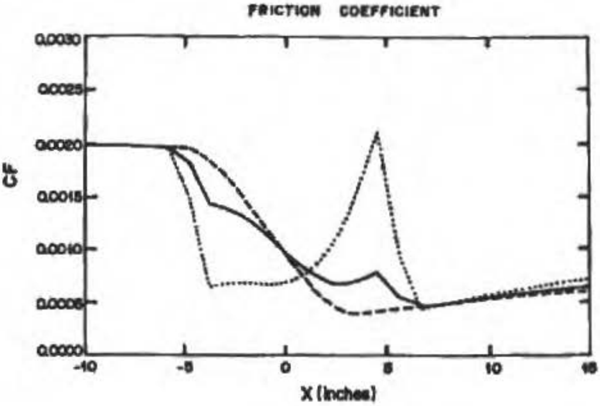

Figure 26. Results for a short stretch of porous surface, $M = 1.37$. ---, $\sigma = 0.0$, — , $\sigma = 0.005$, ... ; $\sigma = 0.02$

CONCLUSION

We have shown in this paper how the problem of the interaction of a shock-wave with a boundary layer can be tackled using perturbation techniques. Thus, the solution in the disturbed region downstream of the shock is completely determined by the undisturbed profiles and by the flow structure assumed in Figure 16.

Unfortunately, the proposed theory could not be compared with experimental results since none were available. It is worth noting that porous surfaces make the use of probes or tubes impossible near the wall since they would block the openings thus affecting the local transpiration rates. This greatly complicates the obtaining of experimental skin-friction values.

Another interesting feature of the theory is that it can be applied to active control cases. The theory can also be easily extended to the case of a curved wall.

ACKNOWLEDGEMENTS

Many interesting discussions with Dr. L.C. Squire of Cambridge University have greatly contributed to the present article. Indeed, many ideas contained in this work are his. Useful comments were also received from Dr. N. Chokani. The work was financially supported partially by the CNPq and partially by an ORS award.

REFERENCES

[1] ADAMSON, T.C. Jr. and MESSITER, A.F. - Analysis of two-dimensional interations between shock waves and boundary layers, Ann. Rev. of Fluid Mech., 12, p. 103-138, 1980.

[2] DELERY, J.M. - Shock wave/turbulent boundary layer interaction and its control, Progress in Aerospace Science, 22, p. 209-280, 1985.

[3] GREEN, J.E. - Interactions between shock waves and turbulent boundary layers, Progress in Aerospace Science, 11, p. 235-341, 1970.

[4] NIEUWLAND, G.Y. and SPEE, B.M. - Transonic airfoils: recent developments in theory, experiment and design, Ann. Rev. Fluid Mech. 5, p. 118-150, 1973.

[5] WHITCOMB, R.T. - Review of Nasa supercritical airfoils, ICAS paper nº 74-10.

[6] SAVU, G.; TRIFU, O.; DUMITRESCU, L.Z. - Supression of shocks on transonic airfoils, 14th Int. Symp. on Shock Tubes and Waves, p. 92-101, 1983.

[7] SAVU, G. and TRIFU, O. - Porous airfoil in transonic flow, AIAA J., 22, p. 989-991, 1984.

[8] NAGAMATSU, H.T.; FICARRA, R.V.; DYER, R. - Supercritical airfoil drag reduction by passive shock wave/boundary layer control in the Mach number range .75 to .90, AIAA paper nº 85-0207, 1985.

[9] RAGHUNATHAN, S.; MABEY, D.G. - Passive shock-wave/boundary-layer control on a wall-mounted model, AIAA J. 25, p. 275-278, 1987.

[10] KROGMANN, P.; STANEWSKY, E.; THIEDE, P. - Effects of suction on shock/boundary layer interaction and shock-induced separation, J. Aircraft, 22, p. 37-42, 1985.

[11] OLLING, C.R.; KULIKRAVICH, G.S. - Porous airfoil analysis using viscous-inviscid coupling at transonic speeds, Int. J. Num. Methods in Fluids, 7, p. 103-121, 1987.

[12] ADAMSON, T.C. Jr.; FEO, A. - Interaction between a shock wave and a turbulent boundary layer at transonic speeds, SIAM J. Appl. Math., 29, p. 121-145, 1975.

[13] ADAMSON, T.C. Jr.; MESSITER, A.F. - Normal shock wave-turbulent boundary layer interactions in transonic flow near separation, Transonic Flow Problems in Turbomachinery, Ed. T.C. Adamson Jr. and M.F. Platzer, p. 392-414, 1977.

[14] LIOU, M.S.; ADAMSON, T.C. Jr. - Interaction between a normal shock wave and a turbulent boundary layer at high transonic speeds. Part II: Wall shear stress, ZAMP, 31, p. 227-246, 1980.

[15] MELNIK, R.E.; GROSSMANN, B. - Analysis of the interaction of a weak normal shock wave with a turbulent boundary layer, AIAA paper nº 74-598, 1974.

[16] MELNIK, R.E.; GROSSMANN, B. - Interactions of normal shock waves with turbulent boundary layers at transonic speeds, Transonic Flow Problems in Turbomachinery, Ed. T.C. Adamson Jr. and M.F. Platzer p. 414, 433, 1977.

[17] MESSITER, A.F. - Interaction between a normal shock wave and a turbulent boundary layer at high transonic speeds. Part I: Pressure distribution, ZAMP, 31, p. 204-227, 1980.

[18] AFZAL, N. - A high order theory for compressible turbulent boundary layers at moderately large Reynolds number, JFM, 57, p. 1-23, 1973.

[19] SILVA FREIRE, A.P. - On the matching conditions for a two deck compressible turbulent boundary layer model, ZAMM, vol. 69, p. 100-104, 1989.

[20] SILVA FREIRE, A.P. - An asymptotic solution for transpired incompressible turbulent boundary layers, Int. J. Heat and Mass Transfer, vol. 31, p. 1011-1021, 1988.

[21] SILVA FREIRE, A.P. - An extension of the transpired skin-friction equation to compressible turbulent boundary layers, Int. J. Heat and Mass Transfer, vol. 31, p. 2395-2398, 1988.

[22] MCQUAID, J. - Incompressible turbulent boundary layers with distributed injection, Ph.D. dissertation, Cantab, 1966.

[23] SIMPSON, R.L.; KAYS, W.M.; MOFFAT, R.J. - The turbulent boundary layer on a porous surface: an experimental study of the fluid dynamics with fluid injection or suction, Stanford University Report, nº HMT-2, 1967.

[24] STEVENSON, T.N. - A law of the wall for turbulent boundary layers with suction or injection, Cranfield College of Aero, Aero Rep., nº 166, 1963.

[25] STEVENSON, T.N. - A modified defect law for boundary layers with suction or injection, Cranfield College of Aero, Aero Rep., nº 170, 1963.

[26] ANDERSEN, P.S.; KAYS, W.M.; MOFFAT, R.J. - The turbulent boundary layer on a porous plate: An experimental study of the fluid mechanics for adverse free-stream pressure gradient, Stanford University, Rep. nº HMT-15, 1972.

[27] SQUIRE, L.C. - Turbulent boundary layers with suction or injection, Conference on data and computation for complex turbulent flows, Rep. of Evaluator, 1980.

[28] FAVRE, A.; DUMAS, R.; VEROLLET, E.; COANTIC, M. - Couche limit turbulent sur paroi poreusse avec transpiration, Journal de Mecanique, 5, p. 3-28, 1966.

[29] MELLOR, G. - The large Reynolds number asymptotic theory of turbulent boundary layers, Int. J. Engn. Sci., 10, p. 851-873, 1972.

[30] YAJNIK, K.S. - Asymptotic theory of turbulent shear flow, JFM, 42, p. 411-427, 1970.

[31] KISTLER, A.L. - Fluctuation measurements in a supersonic turbulent boundary layer, Phys. Fluids, 2, p. 290-296, 1959.

[32] KISTLER, A.L. & CHEN, W.S. - A fluctuating pressure field in a supersonic turbulent boundary layer, JFM, 16, p. 41-64, 1963.

[33] MORKOVIN, M.V. - Effects of compressibility on turbulent flows, Int. Symp. on Mecanique de la Turbulence, p. 367-380, 1962.

[34] KAPLUN, S. - Fluid mechanics and singular perturbation, Academic Press, N.Y., 1967.

[35] LAGERSTROM, P.A. & CASTEN, R.G. - Basic concepts underlying singular perturbation techniques, SIAM Review, vol. 14, p. 63-120, 1972.

[36] SILVA FREIRE, A.P. & HIRATA, M.H. - Approximate solutions to singular perturbation problems: The intermediate variable technique, to appear in J. Math. Anal. Appl.

[37] SQUIRE, L.C. - A law of the wall for compressible turbulent boundary layers with air injection, JFM, 37, p. 449-456, 1969.

[38] SQUIRE, L.C. - Eddy viscosity distributions in compressible turbulent boundary layers with injection, Aero Quarterly, XXIII, p. 169-182, 1971.

[39] SQUIRE, L.C. - Further experimental investigations of compresible turbulent boundary layers with air injection, ARC R & M, nº 3627, 1970.

[40] SQUIRE, L.C. & VERMA, V.K. - The calculation of compressible turbulent boundary layers with fluid injection, ARC CP, nº 1265, 1970.

[41] JEROMIN, L.O.F. - An experimental investigation of the compressible turbulent boundary layer with air injection, R & M, nº 3526, 1966.

[42] VAN DRIEST, E.R. - Turbulent boundary layer in a compressible fluid, J. Aero Sci., 18, p. 145-160, 1951.

[43] MAISE, G. & MCDONALD, H. - Mixing length and kinematic eddy viscosity in a compressible boundary layer, AIAA J., 6, p. 73-80, 1968.

[44] SILVA FREIRE, A.P. - An asymptotic approach for shock-wave/transpired turbulent boundary layer interactions, ZAMP, 39, p. 478-503, 1988.

[45] STANEWSKY, E. - Shock-boundary layer interaction in transonic and supersonic flow, Transonic flows in turbomachinery, Von Karman Inst. Fluid Dyn., Lec. Ser., 59, 1973.

[46] HANKEY, W.L. Jr. & HOLDEN, M.S. - Two-dimensional shock-wave boundary layer interactions in high speed flows, AGARDograph, nº 203, 1975.

[47] LIGHTHILL, M.J. - On boundary layers upstream influence. II: Supersonic flow without separation, Proc. R. Soc. London, Ser. A217, p. 478-507, 1953.

[48] MELNIK, R.E. - Turbulent interactions on airfoils at transonic speeds - recent developments, Symposium on computation of Viscous-Inviscid Flows, paper nº 10, 1981.

[49] GADD, G.E. - Interaction between shock waves and turbulent boundary layers, ARC R & M 3262, 1961.

[50] SAWYER, W.G. & LONG, C.J. - A study of normal shock-wave turbulent boundary-layer interactions at Mach numbers 1.3, 1.4 and 1.5, RAE TR nº 82099, 1982.

RBCM - J. of the Braz.Soc.Mech.Sc.
Vol. XI - nº 3 - pp. 247-272 - 1989

ISSN 0100-7386
Impresso no Brasil

ANÁLISE TERMODINÂMICA DE CICLOS TÉRMICOS EM SISTEMAS COM ESTADOS GIBBS INSTÁVEIS SOB ISOLAMENTO

THERMODYNAMIC ANALYSIS OF THERMAL CYCLES IN SYSTEMS WITH UNSTABLE GIBBS STATES UNDER ISOLATION

Márcio Arab Murad
LNCC/CNPq
Rua Lauro Müller, 455
Rio de Janeiro, RJ - Brasil - CEP 22.290

Rubens Sampaio
PUC/RJ - Departamento de Engenharia Mecânica
Rua Marquês de São Vicente, 225
Rio de Janeiro, RJ - Brasil - CEP 22.453

RESUMO

Este trabalho visa analisar termodinamicamente ciclos térmicos cujo fluido de trabalho é um sistema físico que não possui a propriedade de convexidade em uma das variáveis de seu espaço de estados. Na ref. [8] foi abordado o problema valendo-se do conceito de função de acumulação, utilizando como fluido de trabalho um gás ideal, cujo espaço de estados admite a propriedade de convexidade. O mesmo não ocorre quando o sistema físico é por exemplo, um fluido de Van der Waals, cujo modelo oriundo de sua equação de estado permite a existência de duas fases em equilíbrio, fato este explicado pela existência de estados termodinâmicos que violam o critério de estabilidade sob isolamento proposto por Gibbs.

Palavras-chaves: Estabilidade Termodinâmica ▪ Função de Acumulação ▪ Ciclos Térmicos

ABSTRACT

The present work intends to the thermodynamic analysis of thermal cycles which working fluid is a physical system that doesn't have the characteristic of convexity in one of the variables of its state space. In ref. [8] the same problem was discussed using the concept of accumulation function and employing an ideal gas as the working fluid which state space possesses the property of convexity. The same doesn't occur when the physical system is, for example, a Van der Walls' fluid, whose model derived from its equation of state allows for the possibility of two phases in equilibrium, what is explained by the existence of thermodynamic states that violates the stability criterion under isolation, as proposed by Gibbs.

Keywords: Thermodynamic Stability ▪ Accumulation Function ▪ Thermal Cycles

---

Submetido em Maio/88 Aceito em Novembro/89

INTRODUÇÃO

Uma das versões da Termodinâmica Racional pertencentes as chamadas "Teorias sem Entropia a Priori" foi estruturada por Serrin admitindo uma classe mais restrita de conceitos primitivos. Na referida versão, a existência de grandezas tais como entropia e energia interna é mostrada mediante hipóteses constitutivas, não valendo portanto num universo termodinâmico qualquer de sistemas físicos. Valendo-se somente de conceitos primitivos nesta estrutura, os autores em [8] analisam termodinamicamente os ciclos de Carnot e Rankine utilizando um gás ideal como fluido de trabalho. Esta análise enfoca o comportamento da função de acumulação, presente na forma do segundo axioma nesta teoria, e não apresenta grandes dificuldades devido as propriedades de convexidade do espaço de estados do gás ideal. Entretanto, ainda no universo termodinâmico dos sistemas ideais, quando o fluido em questão viola o critério de estabilidade termodinâmica proposto por Gibbs em certas regiões do plano, ocorre a não convexidade do seu espaço de estados. Este fato acarreta uma maior complexidade na abordagem do problema. A extensão desta análise para a presente situação constitui o principal objetivo deste trabalho.

No início apresentaremos as grandezas primitivas e os dois axiomas presentes nesta teoria racional enfocando o conceito de função de acumulação. Mais adiante definiremos o universo termodinâmico dos sistemas ideais, aonde enquadraremos o fluido de trabalho dos ciclos de Carnot e Rankine, no caso um fluido de Van de Waals. Na Seção 5 será apresentado o conceito de Estabilidade Termodinâmica sob isolamento introduzido por Gibbs, expresso pelos princípios de Entropia Máxima e Energia Mínima. O teorema enunciado a seguir estabelece, no contexto abordado por Serrin, condições necessárias e suficientes para um estado termodinâmico homogêneo, satisfazer as condições de estabilidade. Finalmente, baseado num corolário do teorema aplicado a classe de fluidos simples, será determinado o espaço de estados de um fluido de Van der Waals, o qual não apresentará a propriedade de convexidade devido ao fato da violação do critério de estabilidade em uma região do plano.

ESTRUTURA PRIMITIVA DA TEORIA

Postulamos a existência de um universo termodinâmico N, cujos elementos são sistemas físicos **s**. A cada sistema associamos um conjunto de processos termodinâmicos **P**(s). O subconjunto de **P**(s) de particular interesse neste trabalho é o processo cíclicos $\mathbf{P}_c$ (s), que são caracterizados por não se distinguir os estados inicial e final do sistema.

Não questionamos a existência de uma escala empírica de temperatura. Supomos a existência de uma variedade topológica **v**, denominada variedade de níveis térmicos. Uma escala empírica de temperatura é um mapeamento injetivo definido na variedade com valores nos reais, ou seja:

$$\tau : \mathbf{v} \rightarrow R$$

$$N \rightarrow \tau(N)$$

aonde N é definido como um nível térmico do sistema.

O trabalho $W(P)$ e o calor $Q(P)$ trocados pelo sistema físico **s** durante o processo P são definidos como funções reais da forma:

$$W : \mathbf{P}(\mathbf{s}) \rightarrow R \qquad Q : \mathbf{P}(\mathbf{s}) \rightarrow R$$

$$P \rightarrow W(P) \qquad P \rightarrow Q(P)$$

A informação qualitativa da troca de calor realizada pelo sistema físico é dada pela função de acumulação $Q(P, N)$. Esta função mede o calor trocado por níveis térmicos inferiores ou iguais a N por um sistema físico **s** durante o processo P.

$$Q(\cdot, \cdot) : \mathbf{P}(\mathbf{s}) \times \mathbf{v} \rightarrow R$$

$$(P, N) \rightarrow Q(P, N)$$

Definimos N_i e N_s respectivamente como os níveis térmicos inferior e superior do sistema. Abaixo de N_i e acima de N_s não há troca de calor. Portanto temos que:

$$Q(P, N) = 0 \ , \qquad \text{para} \quad N < N_i$$

$$Q(P, N) = Q(P) \ , \qquad \text{para} \quad N \geq N_s$$

Definimos o espaço de estados do sistema Σ como um conjunto cujos elementos são estados termodinâmicos do sistema. Um estado termodinâmico $\underline{x}, \underline{x} \in \Sigma$, é descrito por uma n-upla da forma:

$$\underline{x} = (x_1, x_2, \dots, x_n)$$

Neste trabalho trataremos somente de processos homogêneos em fluidos simples, cujos estados termodinâmicos são descritos por dois parâmetros e portanto $\Sigma \subset R^2$. Cabe salientar que no caso não homogêneo Σ é um espaço de funções, possuindo assim dimensão infinita.

De posse dos conceitos apresentados podemos enunciar as leis da termodinâmica no presente contexto. A priori não se assume a interconvertibilidade de calor em trabalho. Entretanto pode-se mostrar que para a classe de fluidos simples a 1ª Lei se comporta tal como na teoria clássica (ver [1], [3]). A 1ª Lei da termodinâmica é então enunciada na sua forma forte.

1ª Lei (forma forte). Seja $P \in \mathbf{P}_c(\mathbf{s})$, então:

$$W(P) = Q(P)$$

Um processo P é dito ser adiabático se $Q(P, N) = 0$, para todo $N \in \mathbf{v}$. Enunciamos agora a 2ª Lei na sua forma mais geral.

2ª Lei (forma fraca). Seja $P \in \mathbf{P}_c(\mathbf{s})$, P não adiabático, então existe N_0, $N_0 \in \mathbf{v}$, tal que:

$$Q(P, N_0) < 0$$

Pode-se provar que esta forma fraca da 2ª Lei engloba os princípios de KELVIN-PLANCK e CLAUSIUS (ver [3]).

A forma forte, conhecida como Teorema da Acumulação, é válida no universo termodinâmico dos sistemas físicos compatíveis com um gás ideal. Informações mais detalhadas podem ser encontradas em [1], [3].

CICLOS TÉRMICOS

A aplicação dos conceitos enunciados anteriormente será restrita a dois ciclos freqüentemente estudados pela Termodinâmica Clássica. O ciclo de Carnot e o ciclo de Rankine.

O Ciclo de Carnot. Definimos um ciclo de Carnot positivo P em Σ, como sendo o ciclo no qual:

$$P \in \mathbf{P}_c(\mathbf{s})$$

$$\tau = \tau^+ \quad \text{em} \quad I^+$$

$$\tau = \tau^- \quad \text{em} \quad I^-$$

aonde I^+ e I^- são respectivamente os intervalos de tempo associados a absorção e rejeição de calor, τ^+ e τ^- valores da temperatura empírica sendo que:

$$\tau^+ > \tau^-$$

O Ciclo de Rankine. Definimos um ciclo de Rankine positivo em Σ como sendo o ciclo no qual:

$$P \in \mathbf{P}_c\,(s)$$

$$p = p^+ \quad \text{em} \quad I^+$$

$$p = p^- \quad \text{em} \quad I^-$$

aonde p^+ e p^- são respectivamente os valores das pressões constantes sendo que:

$$p^+ > p^-$$

SISTEMAS IDEAIS

O fluido de trabalho dos ciclos térmicos apresentados será enquadrado num universo termodinâmico particular de sistemas físicos denominado universo dos sistemas ideais.

Um sistema ideal é caracterizado pelos seus possíveis estados termodinâmicos serem dados pelos valores de suas propriedades para cada tempo num espaço de estados de dimensão finita. Os processos termodinâmicos são associados a caminhos no espaço de estados. Matematicamente um processo ideal pode ser descrito pelo mapeamento:

$$\underline{x}\ ;\ I \rightarrow \Sigma \tag{1}$$

$$t \rightarrow \underline{x}\,(t) \tag{2}$$

aonde I é o intervalo de tempo de duração do processo.

O calor e o trabalho trocados pelo sistema ideal no processo ideal P podem ser calculados através das expressões:

$$Q(P) = \int_\Gamma q \qquad \text{com} \qquad q = \sum_{i=1}^{n} Q_i\,(\underline{x})\,dx_i \tag{3}$$

$$W(P) = \int_\Gamma w \qquad \text{com} \qquad w = \sum_{i=1}^{n} W_i\,(\underline{x})\,dx_i \tag{4}$$

aonde Γ é um caminho em Σ; q e w são respectivamente as 1-formas diferenciais de calor e trabalho, as quais em cada ponto $\underline{x} \in \Sigma$ possuem componentes $Q_i(\underline{x})$ e $W_i(\underline{x})$ na base canônica dos funcionais lineares dx_i.

Pode-se mostrar (ver [1], [2], [9]), a partir dos resultados anteriores, a existência para sistemas ideais de funções continuamente diferenciáveis tais como temperatura absoluta (T), energia interna (U) e entropia (S), definidas da forma:

$$T : \mathrm{v} \to R^+$$

$$N \to T(N)$$

$$U : \Sigma \to R$$

$$\underline{x} \to U(x)$$

$$S : \Sigma \to R$$

$$\underline{x} \to S(\underline{x})$$

satisfazendo a equação de Gibbs:

$$q = T\,dS = dU + w \tag{5}$$

aonde R^+ são os reais positivos.

Relações termodinâmicas conhecidas (ver [10]) entre os coeficientes Q_i e W_i das formas diferenciais q e w podem ser facilmente obtidos ao aplicarmos o Teorema de Schwarz aos potenciais termodinâmicos. Para o potencial energia livre de Helmotz, $F = U - TS$ obtemos, no caso de particular interesse neste trabalho em que $X_1 = T$ e $W_1 = 0$, a relação $\partial S/\partial X_j = \partial W_j/\partial T$ $(j = 2, \ldots, n)$ a qual juntamente com (3) e (5) fornece:

$$Q_j = T\frac{\partial W_j}{\partial T} \qquad (j = 2, \ldots, n) \tag{6}$$

Para o potencial S obtemos de forma análoga, e adicionando (6), a relação.

$$\frac{\partial Q_1}{\partial X_j} = T\frac{\partial^2 W_j}{\partial T^2} \qquad (j = 2, \ldots, n) \tag{7}$$

Os sistemas abordados pela Termodinâmica Clássica, denominados fluidos simples, constituem uma subclasse dos sistemas ideais aonde seu estado termodinâmico é descrito por duas variáveis ($\Sigma \subset R^2$), sendo $x_1 = T$, $x_2 = v$, $W_1 = 0$, $W_2 = p$, $Q_1 = C_v$ e $Q_2 = \mathbf{v}$ aonde v é o volume específico, C_v o calor específico a volume constante e $\mathbf{v}$ o valor latente, as formas diferenciais de calor e trabalho são dadas por:

$$w = p(T, v)\, dv \tag{8}$$

$$q = C_v\,(T, v)\, dT + \mathbf{v}\,(T, v)\, dV \tag{9}$$

Decorre de (6) e (7) que para um fluido simples valem as relações:

$$\mathbf{v} = T\,\frac{\partial p}{\partial T} \tag{10}$$

$$\frac{\partial C_v}{\partial v} = T\,\frac{\partial^2 p}{\partial T^2} \tag{11}$$

ESTABILIDADE TERMODINÂMICA

Quando se quer determinar o espaço de estados de um sistema físico, é necessário que seus elementos satisfaçam determinadas condições de estabilidade a serem impostas a cada caso. Neste sentido estabelecemos que o domínio de validade da teoria em questão não contém estados termodinâmicos instáveis.

Na literatura encontramos alguns critérios de estabilidade em Termodinâmica, como por exemplo, segundo LIAPUNOV [5] e segundo GIBBS [6], os quais são introduzidos no contexto de teorias que utilizam a desigualdade de Clausius-Duhem como forma de expressar o segundo axioma [7]. O objetivo aqui é apresentar, no contexto da presente estrutura, o conceito de estabilidade segundo Gibbs. O estado que satisfaz as condições de estabilidade a serem enunciadas será dito Gibbs estável sob isolamento.

Tal denominação salienta o fato de sua validade ser restrita a termostática, ou seja, só se aplica em estados termodinâmicos em equilíbrio com o meio ($Q = Q(\cdot, T) = W = 0$).

Consideremos o universo termodinâmico $\mathbf{U}$ aonde existam as funções energia interna específica, u, entropia específica s e temperatura absoluta T, como por exemplo o universo dos sistemas ideais. Estas funções estão relacionadas entre si por intermédio da equação de Gibbs (5) derivada da equação fundamental:

$$u = u(s, \underline{x}) \quad ; \qquad \underline{x} = (x_1, \ldots, x_n)$$

Enunciamos agora os princípios que expressam matematicamente o conceito de estabilidade termodinâmica sob isolamento segundo Gibbs.

Princípio de Entropia Máxima. "Um estado termodinâmico $(s, \underline{x})$ de um sistema físico $\mathbf{s}$ é dito ser Gibbs estável sob isolamento se e somente se, qualquer estado de $\mathbf{s}$ distinto de $s(\underline{x})$ tal que:

$$U' \overset{def}{=} \int_{\mathbf{s}} u'(\underline{x}'(\underline{\mathbf{x}}), s'(\underline{\mathbf{x}}))\, dm = \int_{\mathbf{s}} u(\underline{x}(\underline{\mathbf{x}}), s(\underline{\mathbf{x}}))\, dm \overset{def}{=} U$$

$$\underline{X}' \overset{def}{=} \int_{\mathbf{s}} \underline{x}'(\underline{\mathbf{x}})\, dm = \int_{\mathbf{s}} \underline{x}(\underline{\mathbf{x}})\, dm \overset{def}{=} \underline{X}$$

satisfaz

$$S' \overset{def}{=} \int_{\mathbf{s}} s'(\underline{\mathbf{x}})\, dm < \int_{\mathbf{s}} s(\underline{\mathbf{x}})\, dm \overset{def}{=} S \text{ "}$$

aonde $\underline{\mathbf{x}} = \underline{\mathbf{x}}(p', t)$ é o ponto espacial ocupado pela partícula p' do sistema físico $\mathbf{s}$ no tempo t.

Princípio de Energia Mínima. "Um estado termodinâmico $(s, \underline{x})$ de um sistema físico $\mathbf{s}$ é dito ser Gibbs estável sob isolamento se e somente se, qualquer estado $(s', \underline{x}')$ de $\mathbf{s}$ distinto de $(s, \underline{x})$ tal que:

$$S' \overset{def}{=} \int_{\mathbf{s}} s'(\underline{\mathbf{x}})\, dm = \int_{\mathbf{s}} s(\underline{\mathbf{x}})\, dm \overset{def}{=} S$$

$$\underline{X}' \overset{def}{=} \int_{\mathbf{s}} \underline{x}'(\underline{\mathbf{x}})\, dm = \int_{\mathbf{s}} \underline{x}(\underline{\mathbf{x}})\, dm \overset{def}{=} \underline{X}$$

satisfaz

$$U' \overset{def}{=} \int_{\mathbf{s}} u'(\underline{x}'(\underline{\mathbf{x}}), s'(\underline{\mathbf{x}}))\, dm > \int_{\mathbf{s}} u(\underline{x}(\underline{\mathbf{x}}), s(\underline{\mathbf{x}}))\, dm \overset{def}{=} U \text{ "}$$

O teorema a seguir enuncia uma condição necessária e suficiente para um estado termodinâmico *homogêneo* ser *localmente* Gibbs estável sob isolamento. É importante salientar que a condição de estabilidade local é mais fraca do que aquela apresentada nos Princípios de Entropia Máxima e Energia Mínima. Tal fato pode ser elucidado pela condição a ser satisfeita no referido teorema, a qual compara o estado termodinâmico em questão somente com estados na sua vizinhança, não possuindo assim, ao contrário dos Princípios enunciados, caráter global. Neste sentido observamos que nem todo estado localmente estável será globalmente estável.

Teorema. Seja $\underline{y}_0$ um estado termodinâmico homogêneo de um sistema físico **s**. Sejam $u = u\,(\underline{y})$ e $w = \sum_{i=1}^{n} W_i\, dx_i$ com $x_1 = T$ e $W_1 = 0$ respectivamente a equação fundamental e a 1-forma diferencial de trabalho de **s**. Então uma condição necessária e suficiente para $\underline{y}_0$ ser localmente Gibbs estável sob isolamento é que a matriz:

$$a_{ij} = \frac{\partial W_i}{\partial x_j} \quad ; \qquad i,j = 2, \ldots, n$$

Seja negativa definida em $\underline{y}_0$.

Prova. Consideremos as funções $\hat{T}, \hat{W}_i, \ldots, \hat{W}_n$ de $(s, \underline{x})$. Para cada estado termodinâmico $\underline{y} \in \Sigma$, diferenciando a equação de Gibbs (5) e aplicando (4) obtemos a seguinte relação entre formas bilineares:

$$d^2u = \Big(\frac{\partial \hat{T}}{\partial s}\Big)\, d^2s + 2 \sum_{i=2}^{n} \Big(\frac{\partial \hat{T}}{\partial x_i}\Big)_s\, dx_i\, ds -$$

$$- \sum_{i=2}^{n} \sum_{j=2}^{n} \Big(\frac{\partial \hat{W}_i}{\partial x_j}\Big)_s\, dx_i\, dx_j \tag{12}$$

Relacionando W_i e $\hat{W}_i$ pela regra da cadeia, (12) pode ser escrita da forma:

$$d^2u = \Big(\frac{\partial \hat{T}}{\partial s}\Big)\, ds^2 + 2 \sum_{i=2}^{n} \Big(\frac{\partial \hat{T}}{\partial x_i}\Big)\, dx_i\, ds -$$

$$- \sum_{i=2}^{n} \sum_{j=2}^{n} \Big(\Big(\frac{\partial W_i}{\partial x_j}\Big) + \frac{\partial W_i}{\partial T}\Big(\frac{\partial \hat{T}}{\partial x_j}\Big)\Big)\, dx_i\, dx_j \tag{13}$$

Sendo $x_1 = T$ e $Q_1 = C_v$, podemos combinar (3) e (5) e aplicar (6) para obter as relações:

$$\frac{\partial \hat{T}}{\partial s} = \frac{T}{C_v} \quad ;$$

$$\frac{\partial \hat{T}}{\partial x_i} = -\frac{Q_i}{C_v} = -\frac{\partial \hat{W}_i}{\partial s}$$

$$\frac{\partial s}{\partial x_i} = \frac{Q_i}{T}$$

$$\frac{\partial s}{\partial x_i} = \frac{\partial W_i}{\partial T}$$

$$i = 2, \ldots, n$$

Definindo $a_{ij} = \dfrac{\partial W_i}{\partial x_j}$ e valendo-se das relações acima (13) pode ser escrita da forma:

$$d^2 u = \frac{1}{C_v T}\left(T\,ds - \sum_{i=2}^{n} Q_i\,dx_i\right)^2 - \sum_{i=2}^{n}\sum_{j=2}^{n} a_{ij}\,dx_i\,dx_j$$

Definindo a função φ_0 da forma:

$$\varphi_0\,(s, x_2, \ldots, x_n) = u\,(s, x_2, \ldots, x_n) - u_0 - T_0\,(s - s_0) + \sum_{i=2}^{n} W_{i_0}\,(x_i - x_{i_0}) \qquad (14)$$

aonde $x_{i_0}, W_{i_0}, T_0, u_0$ e s_0 são referentes ao estado $\underline{y}_0 = (s_0, x_{2_0}, \ldots, x_{n_0})$, sendo:

$$\left(\frac{\partial u}{\partial s}\right)_{\underline{y}_0} = T_0$$

$$\left(\frac{\partial u}{\partial x_i}\right)_{\underline{y}_0} = -W_{i_0} \quad ; \qquad i = 2, \ldots, n$$

Então é fácil observar que:

$$f_0\,(s, x_2, \ldots, x_n) = u_0 + T_0\,(s - s_0) - \sum_{i=2}^{n} W_{i_0}\,(x_i - x_{i_0})$$

é a equação do plano tangente em $(\underline{y}_0, u(\underline{y}_0))$. Logo pela equação (14), $\varphi_0(\underline{y})$ mede a diferença entre o valor da função u e o respectivo valor no plano tangente a superfície no ponto $(\underline{y}_0, u(\underline{y}_0))$:

$$\varphi_0(\underline{y}) = u(\underline{y}) - f_0(\underline{y})$$

Supomos agora que matriz a_{ij} seja não negativa definida. Portanto existe $\xi = (\xi_2, \ldots, \xi_n) \in R^{n-1}$, $\underline{\xi} \neq \underline{0}$, tal que $\sum_{i=2}^{n} \sum_{j=2}^{n} a_{ij}\, \xi_i\, \xi_j \geq 0$. Mostraremos então que o estado $\underline{y}_0$ não satisfaz a condição de estabilidade imposta pelo Princípio de Energia Mínima.

Consideramos então o vetor $\underline{L} \in R^n$ de coordenadas (s, ξ_i), $i = 2, \ldots, n$ tal que:

$$s = \sum_{i=2}^{n} \frac{Q_{i_0}}{T_0} \xi_i$$

No estado $\underline{y}$ temos que:

$$\varphi_0 = 0$$

$$du = T_0\, ds - \sum_{i=2}^{n} W_{i_0}\, dx$$

$$d\varphi_0 = du - T_0\, ds + \sum_{i=2}^{n} W_{i_0}\, dx_i = 0$$

$$d^2 \varphi_0 = d^2 u = \frac{1}{C_{v_0} T_0} \left(T_0\, ds - \sum_{i=2}^{n} Q_{i_0}\, dx_i\right)^2 -$$

$$- \sum_{i=2}^{n} \sum_{j=2}^{n} a_{(ij)_0}\, dx_i\, dx_j$$

Portanto em $\underline{y}_0$ vale:

$$d^2 u\, L^2 = -\sum_{i=2}^{n} \sum_{j=2}^{n} a_{(ij)_0}\, \xi_i\, \xi_j \tag{15}$$

Como por hipótese:

$$\sum_{i=2}^{n} \sum_{j=2}^{n} a_{(ij)_0}\, \xi_i\, \xi_j \geq 0 \tag{16}$$

Vale então:

$$d^2 u\, (\underline{y_0})\, L^2 \leq 0$$

Consideramos agora um estado $\underline{y}'$ não-homogêneo definido a partir de $\underline{y_0}$ por:

$$x_i' = x_{i_0} + \varepsilon\, \xi_i\, t\,(p') \;; \quad i = 2, \ldots, n \tag{17}$$

$$s' = s_0' + \varepsilon\, t\,(p') \sum_{i=2}^{n} \frac{Q_{i_0}}{T_0}\, \xi_i \tag{18}$$

aonde: $\varepsilon > 0$ e $t \cdot \mathbf{s} \to R$ uma função a ser determinada.

Integrando (17) a (18) no sistema físico $\mathbf{s}$ vem:

$$X_i' = \int_{\mathbf{s}} x_i'\, dm = \int_{\mathbf{s}} x_{i_0}\, dm + \varepsilon\, \xi_i \int_{\mathbf{s}} t\,(p')\, dm \;; \quad i = 2, \ldots, n \tag{19}$$

$$S' = \int_{\mathbf{s}} s'\, dm = \int_{\mathbf{s}} s_0'\, dm + \varepsilon \sum_{i+2}^{n} \frac{Q_{i_0}}{T_0}\, \xi_i \int_{\mathbf{s}} t\,(p')\, dm \tag{20}$$

Impondo:

$$X_i' = X_{i_0} = \int_{\mathbf{s}} x_{i_0}\, dm \;; \quad i = 2, \ldots, n \tag{21}$$

$$S' = S_0 = \int_{\mathbf{s}} s_0\, dm \tag{22}$$

Obtemos então através de (19), (20), (21) e (22) que:

$$\int_{s} t\,(p')\,dm = 0 \tag{23}$$

Para cada partícula p' expandimos $u(\underline{y})$ em série de Taylor em torno de $\underline{y}_0$ obtendo:

$$u(\underline{y}') = u(\underline{y}_0) + du(\underline{y}_0)\,\underline{v} + d^2\,u\,(\underline{y}_0)\,\frac{v^2}{2} + r(\underline{v}) \tag{24}$$

aonde impomos $\underline{v}/\!/\underline{L}$ de coordenadas:

$$\underline{v} = \Big(\varepsilon\, t\,(p')\sum_{i=2}^{n}\frac{Q_{i_0}\,\xi_i}{T_0}\;,\;\varepsilon\,\xi_2\,t\,(p'),\,\ldots,\,\varepsilon\,\xi_n\,t\,(p')\Big) =$$

$$= (s - s_0, x_2{}' - x_{2_0}, \ldots, x_n{}' - x_{n_0}) \tag{25}$$

Então:

$$du\,(\underline{y}_0)\,\underline{v} = \Big(T_0\,ds - \sum_{i=2}^{n} W_{i_0}\,dx_i\Big)\,\underline{v} =$$

$$= \varepsilon\, t\,(p')\Big(T_0\sum_{i=2}^{n}\frac{Q_{i_0}\,\xi_i}{T_0} - \sum_{i=2}^{n} W_{i_0}\,\xi_i\Big) =$$

$$= \varepsilon\, t\,(p')\sum_{i=2}^{n}(Q_{i_0} - W_{i_0})\,\xi_i \tag{26}$$

e

$$d^2\,u\,(\underline{y}_0)\,v^2 = -\,\varepsilon^2\,t^2\,(p')\sum_{i=2}^{n}\sum_{j=2}^{n} a_{(ij)_0}\,\xi_i\,\xi_j \tag{27}$$

Integrando (24) e aplicando (26) e (27) vem:

$$U(\underline{y}') - U(\underline{y}_0) = \int_{\mathbf{s}} (u(\underline{y}') - u(\underline{y}_0))\, dm =$$

$$= \varepsilon \sum_{i=2}^{n} (Q_{i_0} - W_{i_0})\, \xi_i \int_{\mathbf{s}} t(p')\, dm -$$

$$- \frac{\varepsilon^2}{2} \sum_{i=2}^{n} \sum_{j=2}^{n} a_{(ij)_0}\, \xi_i \xi_j \int_{\mathbf{s}} t^2(p')\, dm +$$

$$+ \int_{\mathbf{s}} r(\underline{v})\, dm$$

Escolhendo $t : \mathbf{s} \rightarrow R$ de tal forma que (23) é satisfeita e:

$$\int_{\mathbf{s}} t^2(p')\, dm = 1$$

obtemos:

$$U(\underline{y}') - U(\underline{y}_0) = \Big(- \frac{\varepsilon^2}{2} \sum_{i=2}^{n} \sum_{j=2}^{n} a_{(ij)_0}\, \xi_i \xi_j + r(\underline{v}) \Big) M \tag{28}$$

aonde M é a massa do sistema físico $\mathbf{s}$.

Como $u(\underline{y})$ é suposta continuamente diferenciável, vale então:

$$\lim_{\underline{v} \to 0} \frac{r(\underline{v})}{|\underline{v}|^2} = 0$$

Fazendo $\varepsilon \rightarrow 0$, obtemos de (16), (28) e (29) que:

$$U(\underline{y}') - U(\underline{y}_0) \leq 0 \tag{29}$$

Então $\underline{y}_0$ não é Gibbs estável sob isolamento pois não satisfaz as condições impostas pelo Princípio de Energia Mínima.

A condição (29) é necessária. Mostraremos agora que é também suficiente.

Supondo a_{ij} negativa definida em $\underline{y}_0$, então para $\forall \underline{\alpha} = (\alpha_1, \ldots, \alpha_n) \in R^n$ vale:

$$\sum_{i=2}^{n} \sum_{j=2}^{n} a_{(ij)_0} \alpha_i \alpha_j < 0 \tag{30}$$

Logo vem que:

$$d^2 \varphi_0 (\underline{y}_0) \alpha^2 = d^2 u (\underline{y}_0) \alpha^2 =$$

$$= \frac{1}{C_{v_0} T_0} \left(T_0 \alpha_1 - \sum_{i=2}^{n} Q_{i_0} \alpha_i \right)^2 -$$

$$- \sum_{i=2}^{n} \sum_{j=2}^{n} a_{(ij)_0} \alpha_i \alpha_j \tag{31}$$

Aplicando (30) em (31) e utilizando os resultados anteriores obtemos:

$$d^2 \varphi_0 (\underline{y}_0) \alpha^2 > 0 \ ; \quad d\varphi_0 (\underline{y}_0) \underline{\alpha} > 0 \ ; \quad \varphi_0 (\underline{y}_0) = 0 \quad \text{para} \quad \forall \underline{\alpha} = (\alpha_1, ..., \alpha_n) \tag{32}$$

Para cada partícula, uma nova expansão em série de Taylor fornece:

$$\varphi_0 (\underline{y}) = \varphi_0 (\underline{y}_0) + d\varphi_0 (\underline{y}_0) \underline{\alpha} + \frac{d^2 \varphi_0}{2} (\underline{y}_0) \alpha^2 + r (\underline{\alpha}) \tag{33}$$

De (32) e (33) vem que:

$$\varphi_0 (\underline{y}) = \frac{d^2 \varphi_0}{2} (\underline{y}_0) \alpha^2 + r (\underline{\alpha}) \tag{34}$$

Fazendo $\alpha \to 0$, supondo φ_0 continuamente diferenciável, obtemos de (32) e (34) que $\varphi_0 > 0$ para $\underline{y} \in \text{viz} (\underline{y}_0)$.

Sendo:

$$d\varphi_0 = du - T_0 \, ds + \sum_{i=2}^{n} W_{i_0} \, dx_i \tag{35}$$

Integrando (35) de $\underline{y}_0$ a $\underline{y}$ e aplicando (32) vem:

$$u(\underset{\sim}{y}) - u(\underset{\sim}{y}_0) = \varphi_0(\underset{\sim}{y}) + T_0(s - s_0) - \sum_{i=2}^{n} W_{i_0}(x_i - x_{i_0}) \tag{36}$$

Integrando (36) no sistema físico e impondo:

$$S = \int_{s} s\, dm = \int_{s} s_0\, dm = S_0$$

$$X_i = \int_{s} x_i\, dm = \int_{s} x_{i_0}\, dm = X_{i_0}\ ; \qquad i = 2, \ldots, n$$

Obtemos:

$$U(\underset{\sim}{y}) - U(\underset{\sim}{y}_0) = \int_{s} \varphi_0(\underset{\sim}{y})\, dm$$

como $\varphi_0(\underset{\sim}{y}) > 0$, *então* $U(\underset{\sim}{y}) > U(\underset{\sim}{y}_0)$.

Logo pelo Princípio de Energia Mínima, $\underset{\sim}{y}_0$ é localmente Gibbs estável sob isolamento e a prova do teorema está completa.

Podemos observar que a condição (30) expressa a convexidade da função energia interna específica em $\underset{\sim}{y}_0$. Com efeito se $\underset{\sim}{y}_0$ é um ponto de convexidade para *u,vale*:

$$u(\underset{\sim}{y}) > u(\underset{\sim}{y}_0) + T_0(s - s_0) - \sum_{i=2}^{n} W_{i_0}(x_i - x_{i_0})\ , \quad \text{para } \underset{\sim}{y} \in \text{viz}(\underset{\sim}{y}_0) \tag{37}$$

Comparando (37) com (14) obtemos que $\varphi_0(\underset{\sim}{y}) > 0$.

Portanto o estado termodinâmico homogêneo $\underset{\sim}{y}_0$ é localmente Gibbs estável sob isolamento, se e somente se $\underset{\sim}{y}_0$ é um ponto de convexidade para a função energia interna específica.

Consideremos agora algumas aplicações do teorema nos sistemas físicos abordados pela Termodinâmica Clássica.

1) Fluido Simples: Para um fluido simples temos $n = 2$ então a matriz a_{ij} é 1×1 com:

$$a_{11} = \frac{\partial W_2}{\partial x_2} = \frac{\partial p}{\partial v}$$

Para $\underset{\sim}{\xi} = \xi_2 \neq 0$ temos que:

$$\sum_{i=2}^{n} \sum_{j=2}^{n} a_{ij} \xi_i \xi_j = \xi_2^2 \frac{\partial p}{\partial v} < 0$$

Portanto o critério de estabilidade para um fluido simples se reduz a:

$$\frac{\partial p}{\partial v} < 0 \tag{38}$$

2) Fluido de Van der Waals: Um fluido de Van der Waals é um fluido simples que satisfaz a equação de estado:

$$p\,(T, v) = \frac{RT}{v - b} - \frac{a}{v^2} \tag{39}$$

aonde R, a, b são constantes positivas e $v > b$.

Decorre de (11) que para um fluido de Van der Waals $\partial C_v / \partial v = 0$ e a 1-forma q e dada por:

$$q = C_v\,(T, v)\,dT + \frac{RT}{v - b}\,dv \tag{40}$$

O critério de estabilidade (38)[1] aplicado a (39) fornece $T > 2a\,(v - b)/Rv^3$ e a restrição de $p > 0$ impõe $T > a\,(v - b)/Rv^2$. Logo Σ é dado por:

$$\Sigma \equiv \begin{cases} v > b & \\ T > \dfrac{2a\,(v-b)^2}{Rv^3} & \text{quando } v \geq 2b \\ T > \dfrac{a(v-b)}{Rv^2} & \text{quando } b < v < 2b \end{cases}$$

Observamos que no caso de fluido de Van der Waals, ao contrário de um gás ideal, Σ não é convexo na variável v. Decorre então que embora valha $\partial C_v / \partial v = 0$, C_v depende explicitamente de v. Entretanto podemos dividir em duas regiões Σ_l e Σ_g, convexas na variável v, representando respectivamente as fases líquida e gasosa. Com efeito temos:

---

[1] É importante salientar que no caso de um gás ideal, as condições de estabilidade termodinâmica e pressão positiva são satisfeitas para $T > 0$ e $v > 0$.

- Região Σ_l - fase líquida

$$\Sigma_l \equiv \begin{cases} b < v < 3b & \\ T > \dfrac{2a\,(v-b)^2}{Rv^3} & \text{quando } 2b \le v \le 3b \\ T > \dfrac{a\,(v-b)}{Rv^2} & \text{quando } b < v \le 2b \\ T \le \dfrac{8a}{28Rb} & \end{cases}$$

- Região Σ_g - fase gasosa

$$\Sigma_g \equiv \begin{cases} v > b & \\ T > \dfrac{8a}{28Rb} & \text{quando } b < b < 3b \\ T > \dfrac{2a}{Rv^3}(v-b)^2 & \text{quando } v \ge 3b \end{cases}$$

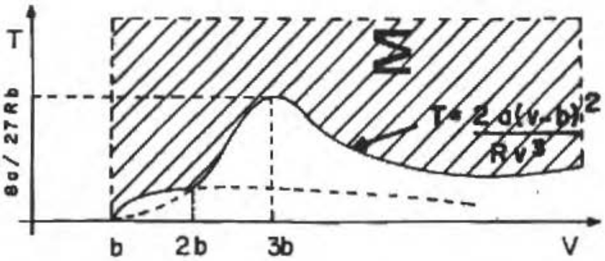

Figura 1. Espaço de estados de um fluido de Van de Waals

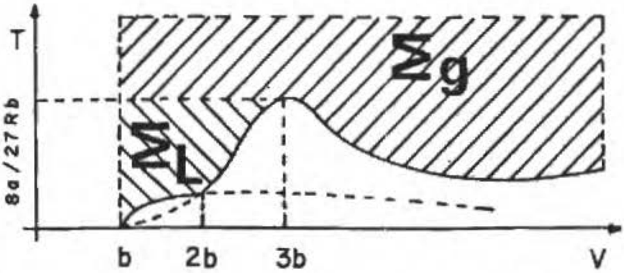

Figura 2. Regiões Σ_l e Σ_g do espaço de estados de um fluido de Van der Waals

Portanto vale:

$$C_v \equiv \begin{cases} C_{v_l}(T) & ; \quad \text{para a região } \Sigma_l \\ C_{v_g}(T) & ; \quad \text{para a região } \Sigma_g \end{cases}$$

aonde C_{v_l} e C_{v_g} são respectivamente os calores específicos a volume constante das fases líquida e gasosa. Sendo que:

$$C_{v_l}\left(\frac{8a}{27Rb}\right) = \lim_{T \to \frac{8a}{27Rb}} C_{v_g}(T)$$

O CICLO DE CARNOT PARA UM FLUIDO DE VAN DER WAALS

Ao contrário de um gás ideal, a análise termodinâmica dos ciclos térmicos para um fluido de Van der Waals deve ser parcelada em região convexas na variável v. Abordaremos aqui os ciclos em Σ_g. A sistemática utilizada poderá ser facilmente aplicada nos outros dois casos: (ciclo em Σ_l, ciclo em Σ_l e Σ_g).

O Ciclo em Σ_g. Para um fluido de Van der Waals temos o seguinte esboço do ciclo de Carnot em Σ_g.

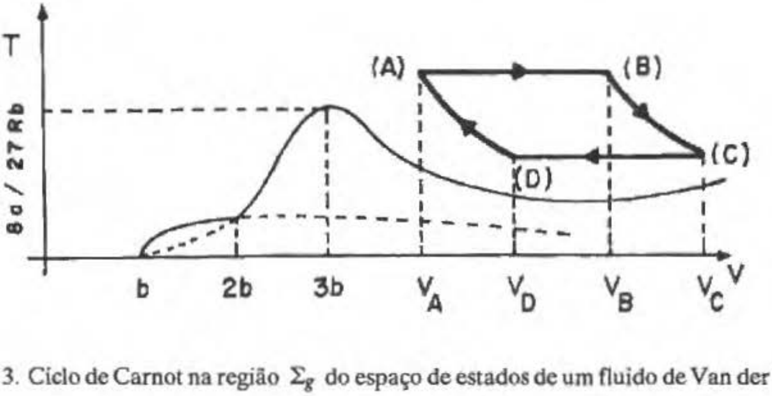

Figura 3. Ciclo de Carnot na região Σ_g do espaço de estados de um fluido de Van der Waals

aonde a equação das adiabáticas A-D e B-C que passam por $(T_0, v_0) \in \Sigma$ é dada por:

$$(v-b) = (v_0 - b)\exp\left(-\frac{1}{R}\int_{T_0}^{T} \frac{C_{v_g}(T')}{T'}\,dT'\right) \quad \text{em } \Sigma_g$$

$$(v-b) = (v_0 - b)\exp\left(-\frac{1}{R}\int_{T_0}^{T} \frac{C_{v_L}(T')}{T'}\,dT'\right) \quad \text{em } \Sigma_L$$

De (40), com T constante, temos que as 1-formas diferenciais de calor absorvido e rejeitado são dadas por:

$q^+ = \frac{RT^+}{v-b}\,dv$, para o caminho que liga A a B, associado a Γ^+

$q^- = \frac{RT^-}{v-b}\,dv$, para o caminho que liga C a D, associado a Γ^-

Portanto as funções de acumulação são dadas por:

$$Q^+(P,T) = \begin{cases} 0 & , \text{ para } T < T^+ \\ RT^+ \ln\left(\frac{v_B - b}{v_A - b}\right) & , \text{ para } T \geq T^+ \end{cases}$$

$$Q(P,T) = \begin{cases} 0 & , \text{ para } T < T^- \\ -RT^- \ln\left(\frac{v_C - b}{v_D - b}\right) & , \text{ para } T^- \leq T < T^+ \\ R(T^+ - T)\ln\left(\frac{v_B - b}{v_A - b}\right) & , \text{ para } T \geq T^+ \end{cases}$$

aonde vale:

$$\frac{v_B - b}{v_A - b} = \frac{v_C - b}{v_D - b}$$

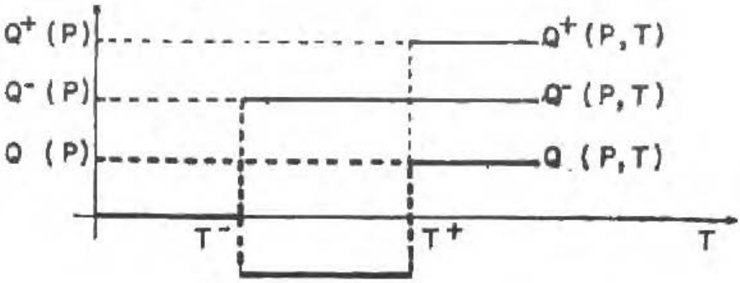

Figura 4. Comportamento das funções de acumulação de calor no ciclo de Carnot para um gás ideal

Sendo:

$$Q^+(P) = Q^+(P,T) \quad , \quad \text{para } T \geq T^+$$

$$Q(P) = Q(P,T) \quad , \quad \text{para } T \geq T^+$$

Portanto:

$$Q(P) = R(T^+ - T^-)\ln\frac{v_B}{v_A}$$

$$Q^+(P) = RT^+ \ln\frac{v_B}{v_A}$$

Aplicando a 1ª Lei na forma forte vem que:

$$W(P) = R(T^+ - T^-)\ln\frac{v_B}{v_A}$$

A eficiência de um ciclo termodinâmico com $Q(P) > 0$ é definida por:

$$Efc(P) = \frac{W(P)}{Q^+(P)}$$

Logo obtemos o conhecido resultado:

$$Efc\,(P) = 1 - \frac{T^-}{T^+}$$

Podemos mostrar de uma maneira análoga que o resultado obtido acima para a eficiência é o mesmo para o ciclo de Carnot nas outras regiões.

A expressão para a eficiência do ciclo de Carnot retifica o conhecido resultado da Termodinâmica Clássica de independência desta com o fluido de trabalho.

O CICLO DE RANKINE PARA UM FLUIDO DE VAN DER WAALS

Tal como procedido no caso anterior a análise será apresentada para o ciclo em Σ_g, podendo esta ser facilmente estendida para os outros casos.

O Ciclo em Σ_g. Para um fluido de Van der Waals temos o seguinte esboço do ciclo de Rankine em Σ_g.

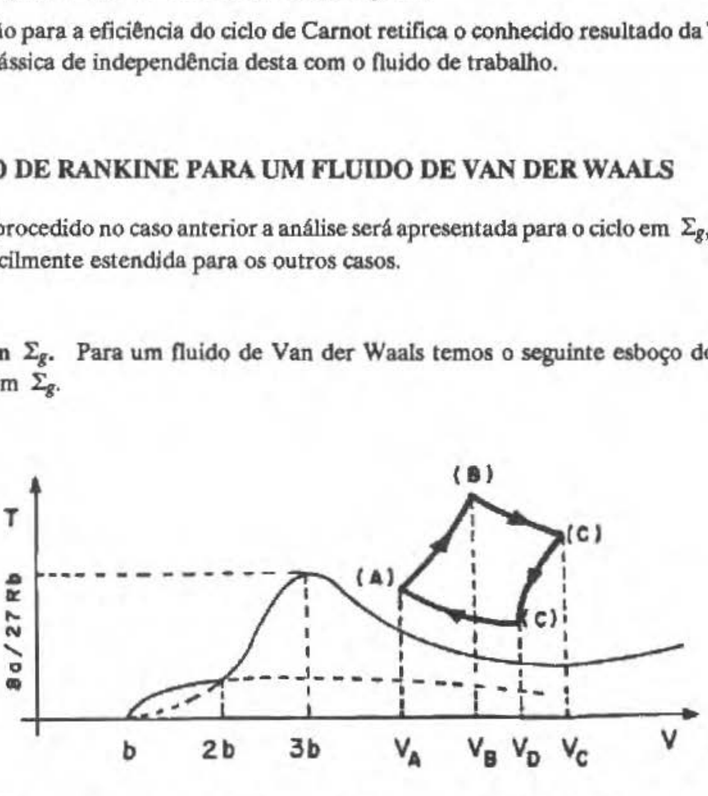

Figura 5. Ciclo de Rankine na região Σ_g do espaço de estados de um fluido de Van der Waals

aonde as curvas B-C e A-D são adiabáticas e as curvas A-B e C-D são isobáricas, cuja equação passando por $(T_0, v_0) \in \Sigma$ é dada por:

$$T + \left(\frac{v-b}{R}\right)\left(\frac{RT_0}{v_0 - b} + a\left(\frac{1}{v^2} - \frac{1}{v_0^2}\right)\right)$$

Para p constante, temos que as 1-formas diferenciais de calor absorvido e rejeitado são dadas por:

$$q^+ = C_{v_g}(T)\,dT + \left(p^+ + \frac{a}{v^2}\right)dv \ , \quad \text{para o caminho que liga A a B associado a } \Gamma^+$$

$$q^- = C_{v_g}(T)\,dT + \left(p^- + \frac{a}{v^2}\right)dv \ , \quad \text{para o caminho que liga C a D associado a } \Gamma^-$$

Portanto as funções de acumulação são dadas por:

$$Q^+(P,T) = \begin{cases} 0 \qquad , \qquad \text{para } T < T_A \\ \int_{T_A}^{T} C_{v_g}(T)\,dT + p^+(v^+(T) - v_A) - a\left(\frac{1}{v^+(T)} - \frac{1}{v_A}\right) \ , \\ \qquad \text{para } T_A \le T < T_B \\ \int_{T_A}^{T_B} C_{v_g}(T)\,dT + p^+(v_B - v_A) - a\left(\frac{1}{v_B} - \frac{1}{v_A}\right) \ , \\ \qquad \text{para } T \ge T_B \end{cases}$$

$$Q(P,T) = \begin{cases} 0 \qquad , \qquad \text{para } T < T_D \\ -\int_{T_D}^{T} C_{v_g}(T)\,dT + p^-(v^-(T) - v_D) - a\left(\frac{1}{v^-(T)} - \frac{1}{v_D}\right) \ , \\ \qquad \text{para } T_D \le T < T_A \\ -\int_{T_D}^{T_A} C_{v_g}(T)\,dT + p^+(v^+(T) - v_A) - p^-(v^-(T) - v_D) - \\ - a\left(\frac{1}{v^+(T)} - \frac{1}{v_A} - \left(\frac{1}{v^-(T)} - \frac{1}{v_D}\right)\right) \ , \quad \text{para } T_A \le T < T_C \\ \int_{T_A}^{T} C_{v_g}(T)\,dt - \int_{T_D}^{T_C} C_{v_g}(T)\,dT + p^+(v^+(T) - v_A) - p^-(v_c - v_D) - \\ - a\left(\frac{1}{v^+(T)} - \frac{1}{v_A} - \left(\frac{1}{v_C} - \frac{1}{v_D}\right)\right) \ , \quad \text{para } T_C \le T < T_B \\ \int_{T_A}^{T_B} C_{v_g}(T)\,dT - \int_{T_D}^{T_C} C_{v_g}(T)\,dT + p^+(v_B - v_A) - p^-(v_C - v_D) - \\ - a\left(\frac{1}{v_B} - \frac{1}{v_A} - \left(\frac{1}{v_C} - \frac{1}{v_D}\right)\right) \ , \quad \text{para } T \ge T_B \end{cases}$$

aonde v^+ e v^- são funções crescentes de T, obtidas diretamente através da equação de estado fixando respectivamente $p = p^+$ e $p = p^-$.

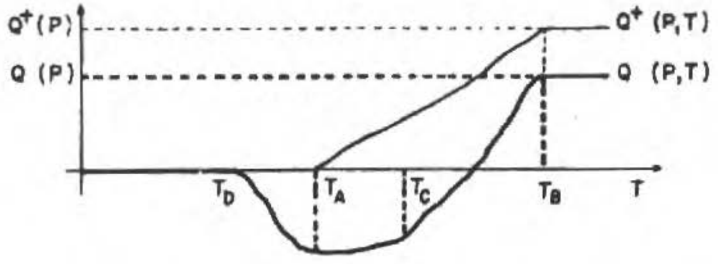

Figura 6. Comportamento das funções de acumulação de calor no ciclo de Rankine para um fluido de Van der Waals

Portanto:

$$Q^+(P) = \int_{T_A}^{T_B} C_{v_g}(T)\,dT + p^+(v_B - v_A) - a\left(\frac{1}{v_B} - \frac{1}{v_A}\right)$$

$$W(P) = Q(P) = \int_{T_A}^{T_B} C_{v_g}(T)\,dT - \int_{T_D}^{T_C} C_{v_g}(T)\,dT + p^+(v_B - v_A) -$$

$$- p^-(v_C - v_D) - a\left(\frac{1}{v_B} - \frac{1}{v_A} - \left(\frac{1}{v_C} - \frac{1}{v_D}\right)\right)$$

$$Efc(P) = 1 - \frac{\int_{T_D}^{T_C} C_{v_g}(T)\,dT + p^-(v_C - v_D) - a\left(\frac{1}{v_C} - \frac{1}{v_D}\right)}{\int_{T_A}^{T_B} C_{v_g}(T)\,dT + p^+(v_B - v_A) - a\left(\frac{1}{v_B} - \frac{1}{v_A}\right)}$$

Para o caso particular de $C_{v_g}(T) = C_{v_g} =$ constante vale:

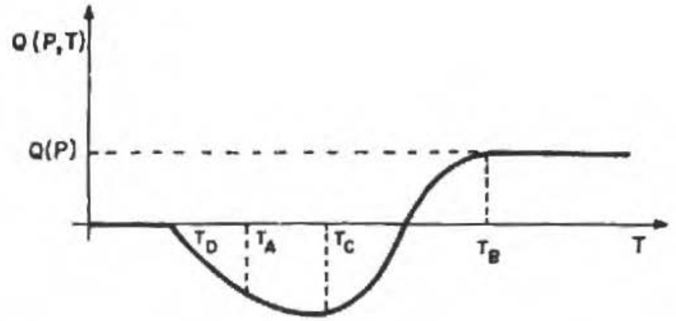

Figura 7. Comportamento da função de acumulação no ciclo de Rankine para um fluido de Van der Waals com C_p constante

Neste caso a eficiência é dada por:

$$Efc\,(P) = 1 - \frac{C_{v_g}(T_C - T_D) + p^+\,(v_C - v_D) - a\left(\frac{1}{v_C} - \frac{1}{v_D}\right)}{C_{v_g}(T_B - T_A) + p^+\,(v_B - v_A) - a\left(\frac{1}{v_B} - \frac{1}{v_A}\right)}$$

CONCLUSÕES

Foi apresentado neste trabalho os principais conceitos da teoria termodinâmica proposta por SERRIN em [1]. Sua principal virtude consiste em não postular *a priori* a existência de funções tais como entropia e energia interna. Portanto as formas propostas dos dois axiomas ao contrário das "Teorias Tipo Clausius-Duhem", não estão expressas em função destas grandezas. Desse modo na classificação das estruturas apresentada em [7], a presente versão se enquadra nas chamadas "Teoria sem Entropia a Priori".

O conhecimento da função de acumulação, presente no segundo axioma, fornece uma informação qualitativa da troca de calor efetuada pelo sistema físico, ou seja, em que níveis térmicos esta foi realizada. Com esta ferramenta podemos obter maiores informações a respeito dos processos termodinâmicos que ocorrem por exemplo em ciclos térmicos.

Foi proposto, no contexto desta estrutura, o conceito de estabilidade termodinâmica segundo Gibbs, apresentado em [6] no contexto de uma "Teoria Tipo Clausius-Duhem".

O teorema 5.3, para estados homogêneos, possui uma grande aplicação na determinação do espaço de estados de um sistema físico. Foi abordado o caso do Fluido de Van der Waals.

A metodologia utilizada neste trabalho pode ser estendida para outros ciclos com outros fluidos de trabalho. A complexidade da análise aumenta quando o sistema físico não pertence ao universo termodinâmico dos sistemas ideais. Neste caso é adicionado um termo dissipado no cálculo da função de acumulação, não sendo esta simplesmente a integral de uma 1-forma diferencial ao longo de um caminho no espaço de estados.

REFERÊNCIAS

[1] SERRIN, J. - New perspectives in thermodynamics, Springer-Verlag, 1986.

[2] SERRIN, J. - Lectures on mathematical thermodynamics, Univ. of Minnesota, 1982.

[3] SERRIN, J. - Conceptual analysis of the classical second law of thermodynamics, Archive for Rational Mechanics and Analysis ARMA, 70: 355-371, 1979.

[4] OWEN, D.R. - A first course in the mathematical foundations of thermodynamics, Springer-Verlag, 1984.

[5] GURTIN, E.G. - Thermodynamics and stability, Archive for Rational Mechanics and Analysis, vol. 59, p. 63-96, 1971.

[6] COLEMAN, B.D. - On the stability of equilibrium states of general fluids, Archive for Rational Mechanics and Analysis, vol. 36, p. 1-32, 1969.

[7] HUTTER, K. - The foundations of thermodynamics, its basic postulates and implications. A review of modern thermodynamics, Acta Mechanica, vol. 27, p. 1-54, 1977.

[8] MURAD, M.A. e SAMPAIO, R. - Estudo de ciclos térmicos no contexto da termodinâmica Racional, Anais do 1º Encontro Nacional de Ciências Térmicas, ENCIT, p. 275-278, 1986.

[9] MURAD, M.A. - As várias faces da termodinâmica dos meios contínuos e aplicações, Tese de Mestrado, PUC, Rio de Janeiro, RJ, 1986.

[10] CALLEN, H.B. - Thermodynamics, John Wiley & Sons, New York, 1960.

RBCM - J. of the Braz.Soc.Mech.Sc.
Vol. XI - nº 3 - pp. 273-291 - 1989

ISSN 0100-7386
Impresso no Brasil

TRANSFERÊNCIA DE CALOR ENTRE SÓLIDO E GÁS NO TRANSPORTE PNEUMÁTICO

GAS-SOLID HEAT TRANSFER IN THE PNEUMATIC TRANSPORT

J.M. Jesus
UFS - Departamento de Engenharia Química
Campus Universitário
São Cristóvão, SE - Brasil - CEP 49.100

Dermeval José Mazzini Sartori - Membro da ABCM
José Teixeira Freire - Membro da ABCM
UFSCar - Departamento de Engenharia Química
Caixa Postal 676
São Carlos, SP - Brasil - CEP 13.560

RESUMO

Foi projetado e construído um equipamento para estudo fluido-térmico no transporte pneumático. Serão apresentados os seguintes resultados: a) Testes fluidodinâmicos para areia e esferas de vidro; b) Medidas de coeficiente de transferência de calor entre o sólido e o fluido para esferas de vidro de diâmetro igual a 10^{-3}*m; c) Análise do desempenho de dois tipos de alimentadores de sólido; d) Método matemático que permite determinar os perfis de temperatura do fluido e dos sólidos.*

Palavras-chave: Transporte Pneumático ▪ Transferência de Calor Gás-Sólido ▪ Testes em Dinâmica dos Fluidos ▪ Coeficiente de Transferência de Calor entre Partículas e Fluido ▪ Modelo Matemático

ABSTRACT

An experimental rig for flow and thermal studies in pneumatic transport has been designed and built. The main aspects presented are: a) Fluidynamics tests for sand and glass spheres; b) Measurement of the particle-to-fluid heat transfer coefficient for glass spheres of particle diameter equal to 10^{-3}*m; c) Analysis of the performance of two different solid feeders; d) Mathematical method for temperature profile determination for the fluid and solids.*

Keywords: Pneumatic Transport ▪ Gas-Solid Heat Transfer ▪ Fluidynamics Tests ▪ Particle-to-fluid Heat Transfer Coefficient ▪ Mathematical Model

---

Submetido em Maio/88 Aceito em Outubro/89

NOMENCLATURA

A	parâmetro, adimensional
A_t	área de troca térmica, definida pela Equação (2), $[L^2]$
A'	definido pela Equação (12), $[\theta]$
B	parâmetro, adimensional
B'	definido pela Equação (13), adimensional
Bi	$= h(dp/2)\, k_s$, número de Biot, adimensional
C	calor específico, $[L^2\, T^{-2}\, \theta^{-1}]$
d_p	diâmetro médio de partícula, $[L]$
d_t	diâmetro da esfera que circunscreve a partícula, $[L]$
D	diâmetro do tubo, $[L]$
G	densidade de fluxo de massa, $[ML^{-2}\, T^{-1}]$
h	coeficiente de transferência de calor gás–partícula, $[MT^{-3}\, \theta^{-1}]$
Nu	$= h\, dp/k_f$, número de Nusselt, adimensional
Re_p	$= \rho_f\, (v_f - v_s)\, d_p/\mu$, número de Reynolds de partícula, adimensional
r	coordenada radial, $[L]$
S	área da superfície das partículas por unidade de volume do leito, $[L^{-1}]$
t	temperatura, $[\theta]$
v	velocidade, $[LT^{-1}]$
W	vazão de massa, $[MT^{-1}]$
Z	coordenada na direção do escoamento do fluido e do sólido,$[L]$
β_v	$= (W_s\, v_f/\rho_s\, (W_f\, v_s/\rho_f)$, concentração volumétrica de sólidos, adimensional
Δt_m	média logarítmica da diferença de temperatura, definida pela Equação (3), $[\theta]$
ε	razão entre o volume da fase fluida e o volume da mistura, porosidade, adimensional
λ	definido pela Equação (14), $[L^{-1}]$
μ	viscosidade, $[ML^{-1}\, T^{-1}]$

ρ	massa específica, $[ML^{-3}]$
φ	d_p/d_l, esfericidade, adimensional
k	condutividade térmica, $[MLT^{-3}\theta^{-1}]$
Ψ	definido pela Equação (15), adimensional
f	fluido
s	sólido
w	mistura
0 ou 1	entrada da célula
2	saída da célula

INTRODUÇÃO

O ótimo contato entre os constituintes sólido e fluido proporcionado no transporte pneumático tem motivado inúmeras aplicações tecnológicas, principalmente, devido à grande ampliação nos coeficientes de transporte tanto de calor como de massa.

Um grande potencial destas aplicações está nos processos de secagem, resfriamento e armazenamento de produtos agrícolas.

Apesar da importância desta técnica ser muito reconhecida, os estudos sobre a transferência de calor no transporte pneumático ainda estão pouco desenvolvidos. Com relação ao coeficiente de troca térmica entre o sólido e o fluido, h, o número excessivo de definições deste parâmetro tem dificultado não só o estabelecimento de correlações mais amplas em função das variáveis do processo, assim como, impossibilitado a análise dos resultados dos diversos pesquisadores, uma vez que estes pesquisadores não apresentam seus dados originais, mas apenas o número de Nusselt em função do Reynolds de partícula e da concentração volumétrica de sólidos. Isto leva, como afirma TORREZAN [1], à não existência, até o momento, de uma correlação confiável para a estimativa do número de Nusselt.

O conhecimento preciso sobre o fenômeno de troca térmica entre a fase sólida e a fase fluida é de importância fundamental para o relacionamento entre as variáveis dinâmicas e térmicas; tais como, as velocidades e temperaturas de fluido e partículas, tempo de residência das partículas e consumo de energia no processo.

Entre as poucas referências bibliográficas que tratam da transferência de calor entre o sólido e o gás com ambas as fases em movimento, os trabalhos de BANDROWSKY e KACZMARZYK [2,3] estão sendo os mais usados como citação básica. Em princípio, estes trabalhos são fundamentados em um balanço global de energia, no qual, o coeficiente de transferência de calor entre o sólido e o gás é definido segundo a equação,

$$h = \frac{W_f C_f (t_{f_1} - t_{f_2})}{A_t \, \Delta t_m} \tag{1}$$

onde,

A_t é a área de transferência de calor entre a partícula e o fluido que no caso de partículas esféricas é dada por,

$$A_t = \frac{6(1 - \varepsilon)}{d_p} \frac{\pi D^2}{4} Z \tag{2}$$

e Δt_m definido como sendo a média logarítmica da diferença de temperatura entre as fases,

$$\Delta t_m = \frac{(t_{f_1} - t_{s_1}) - (t_{f_2} - t_{s_2})}{\ln[\,(t_{f_1} - t_{s_1})/(t_{f_2} - t_{s_2})\,]} \tag{3}$$

t_{f_1} e t_{s_1} são as temperaturas de entrada do fluido e do sólido, respectivamente, e t_{f_2} e t_{s_2} as temperaturas de saída do fluido e do sólido, respectivamente.

Devido às diferenças nos perfis de temperatura experimental em vários níveis do tubo de teste, BANDROWSKI e KACZMARZYK [2,3] decidiram interpretar o dado de saída usando um valor para a temperatura do ar obtido a partir de uma equação que melhor ajustasse os dados experimentais, ou seja,

$$\frac{t_{f_1} - t_f(Z)}{t_f(Z) - t_W} = A\, Z^B \tag{4}$$

onde,

$t_f(Z)$ é a temperatura do fluido na posição Z,

t_W é a temperatura média da mistura na entrada, dada pela igualdade,

$$t_W = (W_s C_s t_{s_1} + W_f C_f t_{f_1})/(W_s C_s + W_f C_f) \tag{5}$$

e os parâmetros A e B são determinados a partir de dados experimentais.

É comum, JESUS [4], subdividir o método de BANDROWSKI e KACZMARZYK [2,3] em dois modelos, ou seja:

Modelo I: Constituído pelas Equações (1 e 3), onde as temperaturas de entrada e saída são os valores obtidos experimentalmente.

Modelo II: Constituído pelas Equações (1 e 3), onde o valor da temperatura do fluido na saída é obtido pelo uso da Equação (4).

A aplicação de qualquer um destes modelos exige a obtenção do valor da porosidade para a determinação da área de transferência de calor, A_t. Entretanto, o que se constata na literatura é que, até o momento, não se dispõe, devido às grandes dificuldades de ordem experimental, de técnicas de medidas diretas da porosidade com boa precisão. Em razão disso, tem-se feito a determinação por meio de técnicas indiretas, isto é, através da aplicação de modelos fluido-dinâmicos, onde a porosidade é uma variável a ser determinada, conforme realizado por BANDROWSKY e KACZMARZYK [2,3], TORREZAN [1] e JESUS [4].

Assim sendo, a partir da análise dos problemas sobre a transferência de calor no transporte pneumático, apresentada na literatura, e considerando a relevância do assunto, este trabalho tem como objetivos:

- Projeto, construção e montagem de um sistema experimental de transporte pneumático, com características similares às apresentadas na literatura, [1,2,3].
- Análise do desempenho de dois tipos de alimentação de sólido: gravitacional e com parafuso helicoidal.
- Desenvolvimento de uma técnica de medida de temperatura do sólido em diferentes posições na célula de medida.
- Desenvolvimento de um modelo matemático para o estudo da troca térmica entre as fases e determinação do coeficiente de transferência de calor entre o sólido e o fluido.

DESENVOLVIMENTO DO MODELO MATEMÁTICO

O volume de controle utilizado, de acordo com o esquema apresentado na Figura 1, é semelhante ao tradicionalmente usado em leito deslizante, conforme pode-se constatar nos desenvolvimentos realizados por FURNAS [5] e SARTORI [6].

O balanço térmico entre as fases sólida e fluida é efetuado levando-se em conta as seguintes considerações:

- escoamento unidimensional concorrente e na direção vertical ascendente;
- regime permanente;

- transferência de calor desprezível na direção normal em relação à transferência de calor na direção do escoamento da suspensão;
- efeito de entrada desprezível, portanto, o coeficiente de troca térmica é uniforme ao longo do leito;
- não há perda nem geração de calor no sistema;
- a resistência térmica interna das partículas é desprezível em relação à resistência de convecção na superfície da partícula, isto é, $Bi < 0,1$.

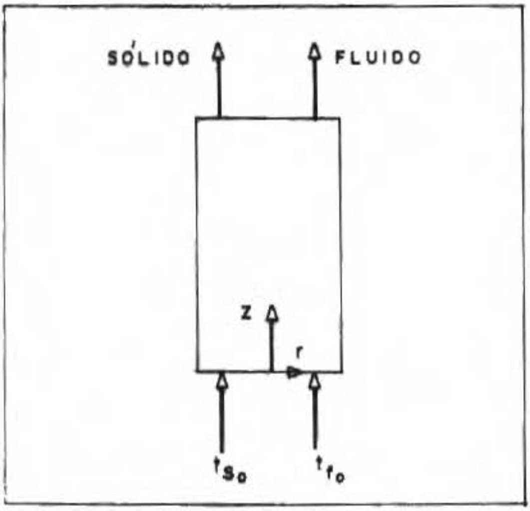

Figura 1. Esquema para os escoamentos concorrentes de sólido e de fluido

Levando em consideração a geometria cilíndrica do sistema e conforme as condições indicadas na Figura 1, as equações diferenciais de balanço de energia são dadas por:

$$\text{Fase fluida:} \quad C_f G_f \frac{dt_f}{dZ} + hS\,[t_f(Z) - t_s(Z)] = 0 \tag{6}$$

$$\text{Fase sólida:} \quad C_s G_s \frac{dt_s}{dZ} - hS\,[t_f(Z) - t_s(Z)] = 0 \tag{7}$$

Sujeitas às seguintes condições de contorno:

$$t_f(0) = t_{f_0} \tag{8}$$

$$t_s(0) = t_{s_0} \tag{9}$$

A solução do sistema constituído pelas Equações (6) e (7) com as condições de contorno (8) e (9) foi obtida em [6] através de uma adimensionalização. A solução é expressa na forma das Equações (10) e (11), para o fluido e o sólido, respectivamente.

$$\frac{A' + B' \, t_f(Z)}{A' + B' \, t_{f_0}} = \exp(\lambda Z) \tag{10}$$

$$\frac{A' + B' \, t_s(Z)}{A' + B' \, t_{f_0}} = -\Psi \exp(\lambda Z) \tag{11}$$

onde,

$$A' = \Psi \, t_{f_0} - t_{s_0} \tag{12}$$

$$B' = 1 + \Psi \tag{13}$$

$$\lambda = (hS/C_f G_f) \, B' \tag{14}$$

$$\Psi = (C_f G_f)/(C_s G_s) \tag{15}$$

$$S = [6 \, (1 - \varepsilon)]/\varphi \, d_p \tag{16}$$

ε = porosidade, (volume da fase fluida)/(volume da mistura)

$$\varphi = d_p/d_l \tag{17}$$

d_l = diâmetro da esfera que circunscreve a partícula

Deve-se notar que a dependência dos perfis de temperatura do fluido, Eq. (10), e do sólido, Equação (11), em relação ao coeficiente de transferência de calor se dá através de λ.

DETERMINAÇÃO DO COEFICIENTE DE TRANSFERÊNCIA DE CALOR

A Equação (14) relaciona o coeficiente de troca térmica, h, ao parâmetro λ. Este é determinado pelo método de ajuste dos mínimos quadrados aplicado à Equação (10), no caso em que as temperaturas de entrada de ambas as fases e a distribuição de temperatura do fluido ao longo da célula de medida são conhecidas, ou a partir da Equação (11), quando a temperatura de entrada e a distribuição de temperatura do sólido ao longo do leito são conhecidas.

Foi provado por SARTORI [6] que estas duas maneiras de obtenção do coeficiente de troca térmica conduz aos mesmos resultados. Como é possível obter a distribuição de temperatura do fluido com mais facilidade experimental em relação à obtenção da distribuição de temperatura do sólido ao longo do leito, optou-se por usar a distribuição de temperatura do fluido.

A partir deste método foi desenvolvido um algoritmo que originou um programa computacional. O programa foi implementado em um microcomputador, que permitiu calcular valores do coeficiente de transferência de calor para diferentes condições operacionais da unidade experimental.

As observações experimentais foram possíveis a partir da montagem de um sistema de transporte pneumático.

ENSAIO DA UNIDADE DE LABORATÓRIO

As medidas foram realizadas em uma unidade de laboratório operando em processos de aquecimento das partículas tendo o ar como fluido percolante. As propriedades destes materiais são descritas a seguir.

Propriedades Utilizadas dos Sólidos e do Fluido. Os valores das propriedades dos materiais são obtidos por meio de experimentos ou advindos da literatura [6,7]. As principais propriedades destes materiais encontram-se nas Tabelas 1 e 2.

Tabela 1. Propriedades dos sólidos

Sólido	d_p^* (10^{-3}m)	φ^x	ρ_s^+ (10^3kg/m^3)	C_s' $(J/\text{kg}\,K)$
vidro	1,00	1,00	2,50	753,48
vidro	1,70	1,00	2,50	753,48
vidro	2,85	1,00	2,50	753,48
areia	1,00	0,68	2,65	795,34
areia	1,69	0,68	2,65	795,34
areia	2,83	0,68	2,65	795,34

Técnica de medida:

* - diâmetro médio de peneira (peneiramento); + - picnometria;

- advindo da literatura [6]; ^{x} - medida por meio de projeção fotográfica

Tabela 2. Propriedades do fluido, ar à pressão de 1 atm, [7]

t (K)	ρ_f (kg/m^3)	μ $(10^{-5}\ kg/m\ s)$	C_f $(J/kg\ K)$	k_f $(J/m\ s\ K)$
300	1,1774	1,983	1004,64	0,0263
350	0,9980	2,075	1008,83	0,0300
400	0,8826	2,286	1013,01	0,0336
450	0,7833	2,484	1021,38	0,0371

O desenvolvimento experimental, empregando estes materiais, é realizado em uma unidade constituída por um conjunto de instalações típicas em equipamentos usados nos estudos sobre transferência de calor em sistemas particulados.

Desenvolvimento Experimental. A) Equipamento

O equipamento, conforme esquematizado na Figura 2, é constituído basicamente por sistemas de alimentação de materiais, medida, separação e resfriamento de sólidos.

- **Sistemas de alimentação**

No sistema de alimentação, o ar é impulsionado por um soprador de 7,36 KW, (Figura 2), para um aquecedor elétrico contendo três resistências elétricas de 19,1; 27,1 e 19,2Ω, sendo as duas primeiras ligadas a variac de 6KVA e 25A e a terceira ligada diretamente à rede elétrica. Este ar ao sair do aquecedor elétrico tem vazão controlada pela válvula V1 e medida no Venturi, após o qual está instalado o termopar T1 para a medida de temperatura de fluido. O sólido é alimentado por gravidade através da abertura de uma válvula gaveta, V2, de $2,54 \times 10^{-2}$ m de diâmetro interno.

- **Sistema de medida**

O sistema de medida consta de uma célula de medida e seus periféricos. A célula de medida é constituída por um tubo de ferro galvanizado, sem costura interna, de $5,38 \times 10^{-2}$ m de diâmetro interno e 3,88 m de comprimento. Ao longo deste tubo estão distribuídas oito tomadas de pressão, nas posições 0,08; 0,58; 1,08; 1,58; 2,58; 3,08 e 3,88 m, a partir da região de entrada de sólido, sete termopares tipo T de cobre-constantan, protegidos com tubo de aço inox de $1,8 \times 10^{-3}$ m de diâmetro externo, em posições idênticas às anteriores, com exceção da posição 0,08 m, e dez coletores de sólidos, (Figuras 3 e 4), nas posições 0,33 e 0,83 m, além das oito tomadas já existentes.

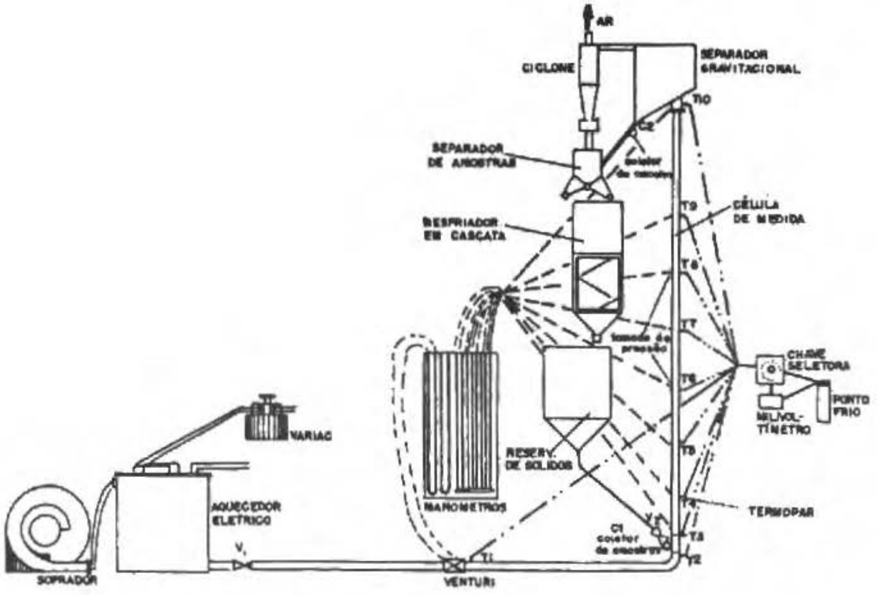

Figura 2. Esquema do equipamento

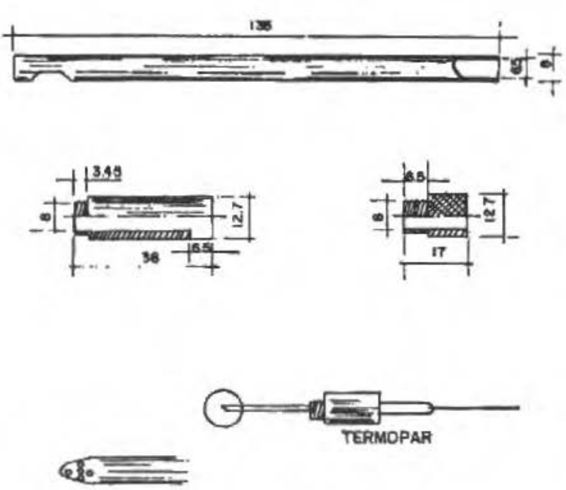

Figura 3. Esquema dos coletores de sólidos e dos termopares (unidade: 10^{-3} m)

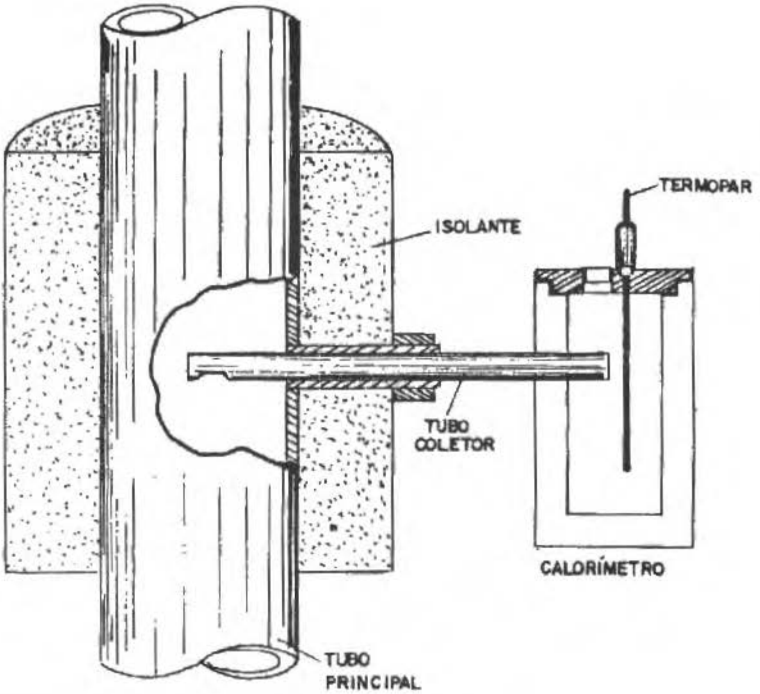

Figura 4. Detalhe do sistema de coleta e medida da temperatura de sólidos ao longo da célula

Os termopares e os coletores de sólido são instalados de modo a permitirem a medida de temperatura no centro da célula.

Além dos termopares e coletores já citados, têm-se também um termopar, sem proteção, T2, (Figura 2), para a medida da temperatura de entrada do fluido na célula e os coletores C1 e C2, para a medida das temperaturas de entrada e saída dos sólidos, respectivamente.

Os termopares são ligados a uma chave seletora de 20 pontos de marca REGULA. O circuito da medida da temperatura é completado por um ponto frio e um milivoltímetro digital de 4 1/2 dígitos e repetibilidade de 0,1%, fabricado pela ECB.

O isolamento térmico do aquecedor, da célula e da tubulação é feito por meio da aplicação de calhas e mantas de silicato de cálcio e lã de vidro, fabricados pela ROEKWOOLBRAS S/A e CARBORUNDUM, respectivamente. A proteção mecânica deste revestimento é feita com **cal-jack**, preso com cintas e selos de alumínio.

B) Procedimento Experimental

Foram desenvolvidos testes preliminares de pressão em função do comprimento da célula para cada material indicado na Tabela 1. Os objetivos são verificar o seu comportamento em relação ao previsto pela literatura e analisar o desempenho dos sistemas de alimentação de sólidos, gravitacional e com parafuso helicoidal.

A vazão do ar procedente do soprador, (Figura 2), é controlada pela válvula V1 e medida no Venturi através do desnível, pré-estabelecido, que é indicado em um manômetro acoplado às tomadas deste medidor, com incerteza de 4,5% na medida. Em seguida, são introduzidos os sólidos pela abertura parcial da válvula V2 e ajustada a válvula V1 até que o desnível inicial do fluido manométrico indicado pelo manômetro ligado ao Venturi seja restabelecido. Procede-se, então, à leitura manométrica para as diversas posições na célula. Finalmente, a vazão de sólidos na saída do resfriador em cascata é determinada pelo método gravimétrico, isto é, faz-se a determinação de uma certa quantidade de massa de sólido coletada em um intervalo de tempo cronometrado. Este método apresentou uma incerteza de medida igual a 2%.

Após o controle das vazões de ar e de sólidos, espera-se até que as temperaturas indicadas pelos termopares, distribuídos na célula de medida, e as temperaturas na entrada e na saída da célula fiquem constantes, quando então são obtidas as medidas. Nos experimentos realizados as temperaturas de entrada do fluido e do sólido variavam de 115,5 a 132,2°C e de 28,7 a 79°C, respectivamente, e as temperaturas de saída do fluido e do sólido variavam de 64 a 92,1°C e de 59,9 a 82,8°C, respectivamente.

A temperatura do fluido é medida pelos termopares com proteção, distribuídos ao longo da célula, e a temperatura do sólido em calorímetros. Todos os termopares foram calibrados utilizando termômetros de mercúrio com precisão de 0,1°C.

A Figura 4 apresenta um detalhe do sistema de coleta e medida de temperatura do sólido.

APRESENTAÇÃO DOS RESULTADOS E CONCLUSÕES

A Figura 5 ilustra o comportamento das curvas de pressão manométrica em função do comprimento da célula de medida para esferas de vidro de diâmetro médio igual a 10^{-3} m. As curvas obtidas para as demais partículas, mostraram-se semelhantes a estas, variando apenas em relação ao valor do comprimento de entrada que não superou a 1,5 m. Esses resultados apresentaram um afastamento máximo de 5% em relação aos dados da literatura [8], para materiais e equipamentos semelhantes.

Foram testados dois tipos de alimentadores: alimentação com parafuso helicoidal e alimentação gravitacional. A alimentação por meio de parafuso helicoidal, apesar de possibilitar um melhor controle da vazão de sólidos, mostrou-se ineficiente, uma vez que o parafuso era constantemente imobilizado pelas partículas finas que ficavam entre o eixo transportador e o tubo. Em função disso, foi usada a alimentação gravitacional, cujo maior inconveniente se verificava na situação em que as partículas eram de forma não-esférica, o que, para um bom escoamento tornava necessária uma vibração no tubo alimentador ocasionando, em conseqüência, uma alimentação pulsante.

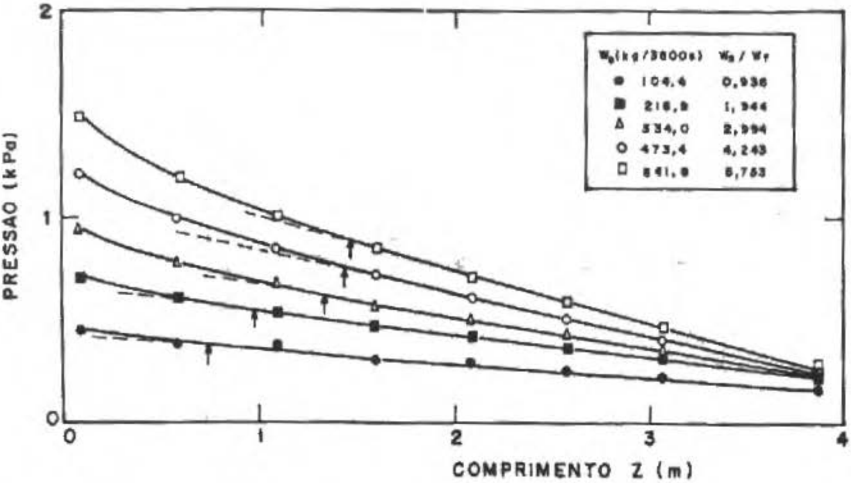

Figura 5. Pressão manométrica em função do comprimento da célula a uma vazão constante de ar, usando esferas de vidro com $d_p = 10^{-3}$ m

A Figura 6 ilustra as temperaturas do fluido e dos sólidos obtidas ao longo da célula de medida. Conforme se pode verificar neste gráfico, a temperatura experimental de sólido apresenta um comportamento anômalo. Observa-se que entre 0,08 e 1,5 m as temperaturas são sempre maiores que as previstas por balanço térmico e que a partir destes valores tornam-se ligeiramente inferiores. Observa-se ainda que a forma da curva assemelha-se mais com a da temperatura do fluido.

Assim sendo, acredita-se que:

1) Na entrada da célula, devido à grande diferença de temperatura entre o sólido e o fluido e como o ato de medir aumenta sensivelmente o contato entre ambas, há uma maior absorção de calor pelos sólidos do que o normal no ponto de coleta, indicando desta maneira uma temperatura superior à real.

2) Quando a diferença real da temperatura entre o sólido e o fluido é pequena, durante a medida de temperatura do sólido existe uma perda de energia, o que ocasiona um valor para a temperatura do sólido ligeiramente inferior ao valor obtido através de balanço térmico.

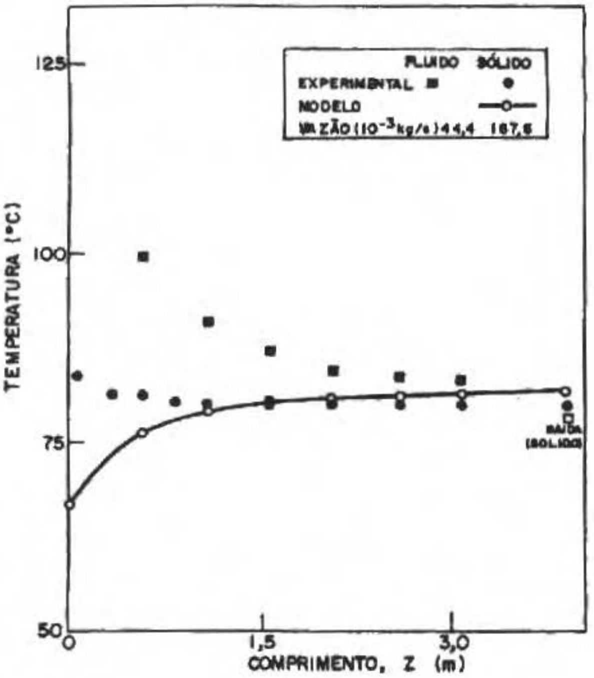

Figura 6. Temperatura do fluido e do sólido em função do comprimento da célula (esferas de vidro; $d_p = 10^{-3}$ m)

A técnica usada para a medida da temperatura dos sólidos ao longo do leito não reproduziu a temperatura real dos sólidos na célula. Isso deveu-se, principalmente, ao longo tempo de coleta em relação ao tempo de residência dos sólidos na célula. No entanto, as temperaturas de entrada e saída são confiáveis uma vez que sua medida é efetuada em tempo muito curto (inferior a 4 segundos), principalmente a de entrada.

O modelo matemático apresentado neste trabalho e o de BANDROWSKI e KACZMARZYK [1,2], foram testados com 35 experimentos em uma faixa de vazão de sólidos de 55×10^{-3} a $192{,}5\times10^{-3}$kg/s, de vazão de fluido de $26{,}9\times10^{-3}$ a $54{,}4\times10^{-3}$kg/s, de números de Reynolds de partículas de 357 a 611 e de concentração volumétrica de $1{,}4\times10^{-3}$ a $5{,}4\times10^{-3}$ m^3 de sólidos/m^3 de suspensão. Uma ilustração desses resultados, advinda de JESUS [4], encontra-se na Figura 7, onde se tem as temperaturas do fluido e dos sólidos em função do comprimento da célula de medida.

A determinação do perfil de temperatura por meio do modelo de BANDROWSKI e KACZMARZYK [2,3] é possível através da correlação,

$$t_f(Z) = (t_{f_0} + AZ^B t_W)/(1 + AZ^B) \quad (18)$$

Porém, para isso é necessário que sejam fornecidos os valores dos parâmetros A e B que por sua vez são conhecidos a partir da realização de experimentos.

No modelo que está sendo proposto neste trabalho, o cálculo de h envolve o conhecimento prévio dos dados de entrada e da distribuição da temperatura do fluido ou do sólido no sistema.

Conhecido o valor de h, torna-se possível a determinação da distribuição de temperatura do fluido pela Equação (10):

$$t_f(Z) = [(A' + B' t_{f_0}) \exp(\lambda Z) - A']/B'$$

ou da distribuição de temperatura do sólido pela Equação (11):

$$t_s(Z) = -[\Psi(A' + B' t_{f_0}) \exp(\lambda Z) + A']/B'$$

que são soluções do problema e onde A', B', Ψ e λ são determinados pelas Equações (12), (13), (15) e (14), respectivamente.

A partir da distribuição de temperatura é possível determinar não apenas a quantidade total de calor trocado como também a quantidade parcial, ou seja, em qualquer comprimento da célula.

Uma comparação gráfica entre os modelos e os valores experimentais é encontrada na Figura 7. Como pode-se observar, tanto o modelo deste trabalho, Figura 7a, quanto o modelo de BANDROWSKI e BACZMARZYK [2,3], Figura 7b, reproduzem com boa aproximação os valores experimentais de temperatura do fluido. O maior afastamento encontrado em relação a estes, ponto a ponto, foi de 5,1 e 7,0% para este trabalho e para o modelo de BANDROWSKI e KACZMARZYK [2,3], respectivamente, e este afastamento ocorre quase sempre na posição 0,5 m. Nesses gráficos, pode-se perceber que a troca térmica é predominante na região de entrada, aproximadamente 1,5 m, e que, quanto maior é a concentração de sólidos menor é a distância em que as temperaturas do sólido e do fluido entram em equilíbrio.

Tanto o modelo deste trabalho quanto o de BANDROWSKI e KACZMARZYK [2,3] apresentaram desvios muito pequenos em relação à temperaturas originalmente medidas. No entanto, com o modelo de BANDROWSKI e KACZMARZYK [2,3] não é possível se chegar a uma distribuição de temperatura ao longo da célula, enquanto que, com o modelo deste trabalho isto é possível, permitindo assim o cálculo da quantidade de calor trocado para qualquer comprimento da célula. E ainda, devido à boa concordância com os dados experimentais de temperatura do fluido, torna possível a estimativa da temperatura do sólido.

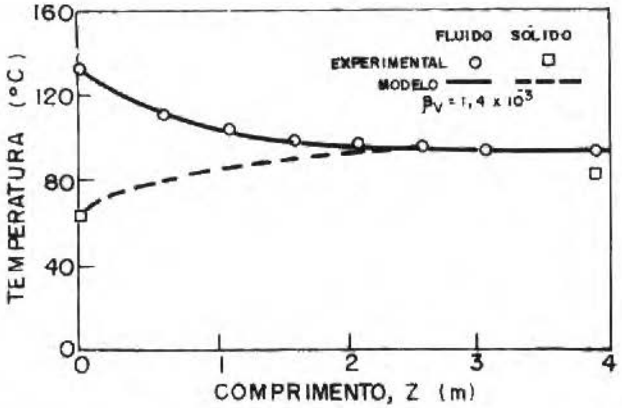

Figura 7a. Temperatura do fluido e do sólido em função do comprimento (Modelo deste trabalho

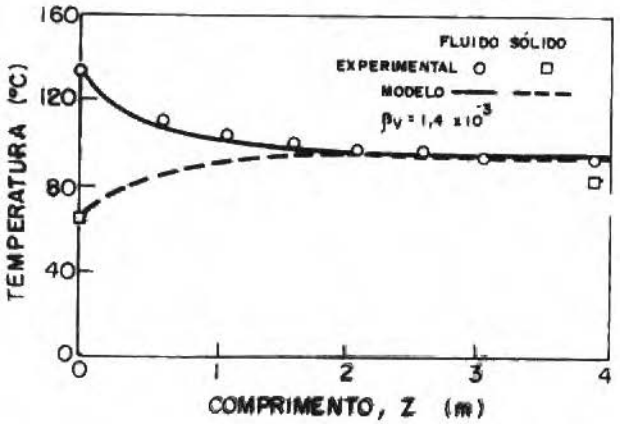

Figura 7b. Temperatura do fluido e do sólido em função do comprimento (Modelo de BANDROWSKI e KACZMARZYK [2,3]

Na Figura 8 são apresentados os valores $Nu/\mathrm{Re}_p^{0,8159}$ em função de β_v obtidos neste trabalho assim como os obtidos por TORREZAN [1], para o mesmo sistema e partícula, além dos valores previstos pela correlação de BANDROWSKY e KACZMARZYK [2,3],

$$Nu = 0{,}00114\,\beta_v^{-0{,}5984}\,\mathrm{Re}_p^{0{,}8159} \tag{19}$$

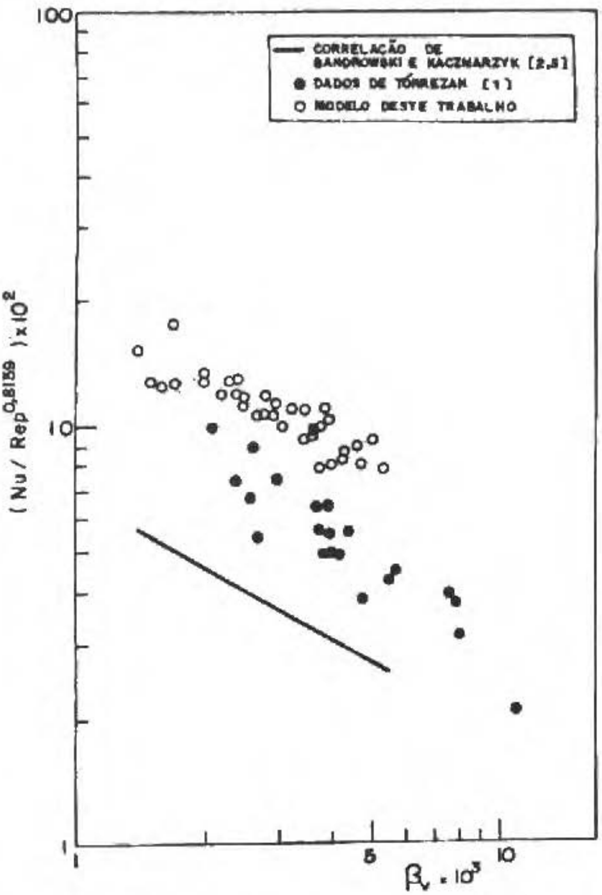

Figura 8. Comparação entre os valores obtidos neste trabalho, dados de TORREZAN [1] e a correlação de BANDROWSKI e KACZMARZYK [2,3]

A finalidade da Figura 8 não é de comparação numérica mas, principalmente, mostrar que mesmo partindo de uma definição única para o coeficiente de troca térmica (h), como é o caso do nosso modelo, dos dados de TORREZAN [1] e da previsão de BANDROWSKI e KACZMARZYK [2,3], ainda não se chegou a números de Nusselt comparáveis uma vez que cada autor usou um método diferente de obtenção do fator de atrito entre o sólido e a parede do tubo.

Portanto, pode-se concluir que:

O comportamento fluidodinâmico está em consonância com o da literatura para equipamento e material semelhantes.

A técnica usada para a medida da temperatura dos sólidos ao longo da célula não reproduziu a temperatura real dos sólidos. Dois outros sistemas estão sendo testados:

i) sistema que desvia todo o escoamento de sólido para um calorímetro. Assim, o tempo de coleta será minimizado;

ii) sistema "sensor" para desvio, coleta contínua no interior do transportador pneumático de uma parte do sólido em escoamento e medida da temperatura deste material.

A alimentação de sólidos apesar de limitante mostrou-se eficiente para partículas esféricas, podendo ser aumentada a faixa de vazão de sólidos com a elevação na altura do reservatório.

O modelo proposto é de simples aplicação e forneceu boa previsão para o perfil de temperatura. A principal vantagem em relação ao modelo proposto por BANDROWSKI e KACZMARZYK [2] é que fornece diretamente a distribuição de temperatura ao longo da célula, uma vez conhecido o coeficiente de troca térmica.

AGRADECIMENTO

Ao Conselho Nacional de Desenvolvimento Científico e Tecnológico (CNPq) pelo apoio financeiro para o desenvolvimento deste trabalho.

REFERÊNCIAS

[1] TORREZAN, L.M.V. - Transferência de calor no transporte vertical de partículas, Dissertação de Mestrado, UNICAMP, abril, 1986.

[2] BANDROWSKI, J. & KACZMARZYK, G. - Gas-to-particle heat transfer in vertical pneumatic conveying of granular materials, Chemical Engineering Science, 33 (10), pp. 1303-10, 1978.

[3] KACZMARZYK, G. & BANDROWSKI, J. - Gas-solid heat coefficient in vertical pneumatic transport, International Chemical Engineering, 20 (1), pp. 98-110, 1980.

[4] JESUS, J.M. - Transferência de calor gás-sólido no transporte pneumático, Dissertação de Mestrado, UFSCar, 1987.

[5] FURNAS, C.C. - Heat transfer from a gas stream to a bed of broken solids II, Industrial and Engineering Chemistry, 22 (7), pp. 721-31, 1930.

[6] SARTORI, D.J.M. - Transferência de calor em leito deslizante, Tese de Doutorado, COPPE/UFRJ, maio, 1986.

[7] PERRY, R.H. & CHILTON, C.H. - Chemical Engineer's Handbook, 5 ed. Ed. McGraw Hill Kogakusha, Ltd., 1973.

[8] da SILVA, M.G.C. - Dinâmica de transporte pneumático vertical de partículas, Dissertação de Mestrado, UNICAMP, junho, 1984.

OBJETIVO E ESCOPO

A Revista Brasileira de Ciências Mecânicas visa a publicação de trabalhos voltados ao projeto, pesquisa e desenvolvimento nas grandes áreas das Ciências Mecânicas. É importante apresentar os resultados e as conclusões dos trabalhos submetidos de forma que sejam do interesse de engenheiros, pesquisadores e docentes.

O escopo da Revista é amplo e abrange as áreas essenciais das Ciências Mecânicas, incluindo interfaces com a Engenharia Civil, Elétrica, Metalúrgica, Naval, Nuclear, Química e de Sistemas. Aplicacões de Física e de Matemática à Mecânica também serão consideradas.

Em geral, os Editores incentivam trabalhos que abranjam desenvolvimento e a pesquisa de métodos tradicionais bem como a introdução de novas idéias que possam potencialmente ser aproveitadas na pesquisa e na indústria.

AIMS AND SCOPE

The Journal of the Brazilian Society of Mechanical Sciences of concerned primarily with the publication of papers dealing with design, research and development relating to the general areas of Mechanical Sciences. It is important that the results and the conclusions of the submitted papers are presented in a manner which is appreciated by practising engineers, researchers, and educationalists.

The escope of the Journal is broad and encompasses essential areas of Mechanical Engineering Sciences. In addition, interface with Civil, Eletrical, Metallurgical, Naval, Nuclear, Chemical and System Engineering as well as in the areas of Physics and Applied Mathematics, are welcomed.

In general, the Editors are looking for papers covering both development and research of traditional methods and the introductions of novel ideas which have potential in science and manufacturing industry.

Note and Instructions To Contributors

1. The Editors are open to receive contributions from all parts of the world, and manuscripts for publication should be sent to the Editor-in-Chief or to the appropriate Associate Editor.
2. (i) Papers offered for publication must contain unpublished materials and will be refereed and assessed by reference to the aims of the Journal as stated above. (ii) Reviews should constitute outstanding critical appraisals of published materials and will be published by suggestion of the Editors. (iii) Letters and communications to the Editor should not exceed 400 words in length and may be: Criticisms of articles recently published in the Journal; Preliminary announcements of original work of importance warranting immediate publications; Comments on current engineering matters of considerable moment.
3. Only papers not previously published will be accepted and authors must agree not to publish elsewhere a paper submitted to and accepted by the Journal. Exception can be made in some cases of papers published in annals or proceedings of conferences. The decision on acceptance of papers is taken by the Editors on behelf of two reviews of outstanding scientists and will take into consideration their originality, contribution to science and/or technology.
4. All contribution are to be in English or portuguese. However Spanish will also be considered.
5. Manuscripts should begin with the title of the article, always including the english title the author's name, and the address from which communication comes. In the case of co-autors, respective addresses should be clearly indicated. Follow with the abstract in the paper's language; if different from english an extended summary in this language shell be included. Give also key words for the paper. Next, it possible, the nomenclature list shell be presented.
6. Manuscripts should be typed with double spacing with ample margins, in accordance to other published material submitted in triplicate. Pages should be numbered consecutively.
7. Figures and line drawing should be originals and include all relevant details; only excelent photocopies should be sent. Photographs should be enlarged sufficiently to permit clear reproduction in half-tone. If words or numbers are to appear on a photograph then they should be sufficiently large to permit the necessary reduction in size. Figure captions should be typed on a separate sheet and placed at the end of the manuscript.

REVISTA BRASILEIRA DE CIÊNCIAS MECÂNICAS
JOURNAL OF THE BRAZILIAN SOCIETY OF MECHANICAL SCIENCES

Vol. XI - Nº 3 *1989*

ÍNDICE / CONTENTS